Between metal and insulator : ultrafast dynamics in the topological insulator Bi2Te3and microscopic domains at the Mott transition in V2O3

Mahdi Hajlaoui

Université Paris XI
U.F.R. Scientifique d'Orsay

THÈSE

présentée à l'Université Paris XI
pour obtenir le grade de

Docteur en Sciences de l'Université Paris XI, Orsay
E.D. 107 – Spécialité : Physique

Entre métal et isolant: dynamique ultra-rapide dans l'isolant topologique Bi_2Te_3 et domaines microscopiques à la transition de Mott dans V_2O_3

par

Mahdi HAJLAOUI

Soutenue le 25 septembre 2013 devant le jury composé de :

Petra Rudolf	Rapporteur
Ricardo Lobo	Rapporteur
Michel Héritier	Examinateur
Yannick Klein	Examinateur
Marino Marsi	Directeur de thèse
Evangelos Papalazarou	Co-directeur de thèse

Remerciement

Je souhaite ici saluer et remercier tous ceux qui m'ont aidé à aller au bout de cette thèse, ainsi qu'à la réussite de ces formidables années de recherche.

Cette thèse s'est déroulée au Laboratoire de Physique des Solides, je tiens à remercier la directrice Dominique Chandesris, de m'y avoir accueilli.

Je tiens à remercier sincèrement mon professeur Marino Marsi, qui, en tant que Directeur de thèse, s'est toujours montré à l'écoute et très disponible tout au long de ces trois années, ainsi pour l'inspiration, l'aide et le temps qu'il a bien voulu me consacrer et sans lui cette thèse n'aurait jamais vu le jour.

Mes remerciements s'adressent également à Evangelos Papalazarou, pour sa générosité et son aide pour les mesures pompe sonde. Son présence a donné une véritable impulsion pour l'élaboration de ce travail. J'ai particulièrement apprécie sa gentillesse. Merci Evangelos !

Ce travail de thèse s'est déroulé dans une très bonne ambiance grâce au travail de l'équipe Femto-ARPES, que j'ai partagé avec, Luca Perfetti et Julien Mauchain qui ont facilité mon début de thèse en partageant leurs expériences expérimentales et en répondant à mes questions.

Je voudrais remercier tous les chercheurs avec qui j'ai interagi pendant ma thèse. Je remercie Luca Gregoratti et Matteo Amati , pour nous avoir accueilli de nombreuses fois sur La ligne ESCAmicroscopy à Elettra. Merci Sylvain Ravy, Eric Elkaim et Claire Laulhé pour nous avoir accueilli sur Cristal à Soleil, et avoir sacrifié un week-end pour nous. Merci à Jean-Pascal Rueff, de La ligne Galaxie Soleil, pour nous avoir assisté avec patience au cours de nos tentatives d'expériences.

Je voudrais remercier Gabriel Lantz avec qui j'ai partagé une grande partie de la mesure SPEM à Elettra. Un merci également à tout les personnes du laboratoire de physique des solides. Merci à tous ceux que je n'ai pas cité et avec qui j'ai fait un bout de chemin

Je ne saurais conclure sans dédier une pensée à ma famille, à leur indispensable et indéfectible soutien depuis le début.

Merci, Merci, Merci...

Contents

To my Mother and Father...

Chapter 1

Introduction

La différence entre les matériaux électroniques conduits et isolants est l'un des concepts les plus fondamentaux de la physique des solides, avec de nombreuses applications dans la vie quotidienne. Dans la plupart des cas, la théorie de la bande classique peut expliquer les raisons de cette différence. Par la combinaison de différents matériaux, il a été possible de réaliser des dispositifs de la matiàre condensée qui peuvent aller d'un isolant à un conducteur d'une manière contrôlée. Le fonctionnement de la plupart de ces dispositifs, comme par exemple le transistor, est aujourd'hui tout à fait compréhensible en utilisant la théorie quantique conventionnelle des solides.

Dans le même temps, la plupart des domaines de recherche les plus actifs en physique de la matière condensée portent sur des matériaux qui présentent des états conducteurs ou isolants, différents de métaux ou isolants normaux. Exemples bien connus de ces nouvelles structures électroniques sont le graphène et les supraconducteurs à haute température. Ces matériaux complexes nécessitent des modèles théoriques plus avancées pour décrire leurs structures électroniques, et des méthodes expérimentales nouvelles et sophistiquées pour mesurer quand et comment ils transmettent le courant. Dans certains cas, les deux phases métallique et isolant coexistent dans le même matériau à l'échelle microscopique : un électron peut trouver un environnement soit conducteur ou isolant à une distance de quelques nanomètres.

Le travail présenté dans cette thèse concerne l'étude de deux de ces matériaux

complexes : un prototype 3D d'isolant topologique Bi_2 Te_3 et un archétype du Mott-Hubbard V_2O_3. L'objectif principal est l'étude expérimentale comment les deux phases métallique et isolant peuvent coexister dans ces matériaux à l'échelle nanométrique, en utilisant la spectroscopie de photoélectrons. En particulier, cette technique permet de mesurer la densité d'état à la proximité de l'énergie de Fermi, ce qui permet de détecter immédiatement si ils sont dans un état métallique ou isolant. De plus, cette technique présente une méthode puissante pour visualiser directement les bandes électroniques, fournissant un test expérimental important pour les modèles théoriques.

Les isolants topologiques sont l'un des nouveaux champs de la physique de la matière condensée, avec des concepts novateurs qui ont été d'abord développés par des travaux théoriques, et qui ont été plus tard vérifiés expérimentalement dans les matériaux réels comme Bi_2Te_3. Dans les isolants topologiques, les électrons dans les états de bord sont décrits par des équations de Dirac et sont topologiquement différents du volume. Cette différence conceptuelle explique pourquoi la surface d'isolant topologique comme Bi_2Te_3 est un conducteur particulièrement robuste et efficace, alors que seulement quelques couches atomiques sous la surface du matériau est un isolant normal.

Les matériaux fortement corrélés sont plutôt un problème classique de la physique de l'état solide, où les corrélations électroniques à plusieurs corps jouent un rôle essentiel. Ces matériaux peuvent présenter de nombreuses transitions de phase, souvent avec une phénoménologie très compliqué dont l'interprétation est très difficile, même pour les modèles théoriques les plus avancées. En particulier, V_2O_3 est un matériau prototype pour la transition de Mott, où le système peut aller d'un isolant à un métal sans briser la symétrie du cristal, et seulement en changeant les paramètres externes comme la température ou le dopage. La transition de phase est de premier ordre, et par conséquent, elle présente la coexistence microscopique des domaines isolants et métalliques.

Dans cette thèse, je vais présenter les résultats expérimentaux obtenus en utilisant principalement deux techniques basées sur la spectroscopie de photoélectrons. La premiére est le TR-ARPES (time and angle resolved photoemission spectroscopy),

qui permet de distinguer la dynamique ultra-rapide des états métalliques de la surface de celle des états isolants du volume dans Bi_2Te_3. Et la deuxième est le SPEM (scanning photoelectron microscopy), qui a été utilisé pour étudier la coexistence des domaines métalliques et isolants à la transition de Mott dans le Cr-dopé.

Le manuscrit est structuré comme suit:

Chapitre 2 donnera une introduction à la physique des isolants topologiques. Je vais d'abord commencer à présenter ce sujet dans le cas 2D, dans le but de faciliter la description des isolants topologiques 3D. Plus tard, je vais décrire en détail certains travaux expérimentaux et théoriques sur le systme 3D Bi_2Te_3 , qui est le matériau étudié dans cette thèse.

Chapitre 3 concentrera sur la description de la transition de Mott. La première partie de ce chapitre présente un aperu théorique de la transition de Mott. La deuxième partie se concentre sur la description du composé prototype de Mott-Hubbard qui est le vanadium sesquioxyde (V_2O_3) ainsi que sur les résultats expérimentaux récents obtenus sur ce système en utilisant la spectroscopie de photoélectrons.

Chapitre 4 présentera une description détaillée des différentes méthodes expérimentales basées sur la spectroscopie de photolectrons : *angle resolved photoemission spectroscopy* (ARPES), *time and angle resolved photoemission spectroscopy* (TR- ARPES) et *scanning photoelctron microscopy* (SPEM). En particulier, une explication sera donnée de la façon comment on peut effectuer la spectroscopie de photoélectrons avec une résolution femtoseconde dans le temps, ou une résolution nanométrique dans l'espace.

Les deux chapitres suivants sont consacrés aux résultats originaux obtenus au cours de mon travail de doctorat.

Chapitre 5 présentera l'application du TR-ARPES à l'étude de l'isolant topologique 3D Bi_2Te_3 photoexcité avec des impulsions laser ultra-rapides, montrant comment on peut explorer la dynamique des porteurs, à la fois de la surface et du volume, ainsi que les différents mécanismes de diffusion entre eux. La durée de vie des électrons chauds du cône de Dirac peut être largement améliorée par la préexistante à la sous-surface d'une bande de flexion, conduisant à des états de

surface fortement hors équilibre.

Chapitre 6 présentera une étude de la microscopie de photoémission dans ($V_{1-x}Cr_x)_2O_3$, fournir la preuve de la coexistence des domaines métalliques et isolants à la transition de Mott . L'origine et l'évolution des différents domaines métalliques sont discutées, et une comparaison entre l'état du Cr-dopé et du composé non dopé métallique est montré.

Introduction

The difference between conducting and insulating electronic materials is one of the most basic concepts in solid state physics, with many applications in everyday life. In most cases, normal band theory can explain the reasons for this difference. Combining different materials, it has even been possible to realize condensed matter devices that can go from an insulating to a conducting state in a controlled way. The operation of most of these devices, like for instance the transistor, is nowadays completely understandable using conventional quantum theory of solids. At the same time, many of the current most active research fields in condensed matter physics concern materials that present original conducting or insulating states, different from normal metals or insulators. Very well known examples of such novel electronic structures are for instance graphene and high temperature superconductors. These complex materials require more advanced theoretical models to describe their electronic structure, and require novel and sophisticated experimental methods to measure when and how they transmit current. In some cases, metallic and insulating phases coexist in the same material on a microscopic scale, and an electron can find an either insulating or conducting environment at a distance of few nanometers.

The work presented in this thesis concerns the study of two of these complex materials: a prototype 3D topological insulator, Bi_2Te_3 and an archetype Mott-Hubbard compound, V_2O_3. Its main purpose is the experimental study of how metallic and insulating phases can coexist in these materials on the nanometer scale, using the photoelectron spectroscopy. In particular, this technique can measure the material electron density of states in the proximity of the Fermi energy, allowing to immediately detect if they are in a metallic or insulating state; furthermore, it represents a powerful method to directly visualize the electronic bands, providing an important experimental test for theoretical models.

Topological insulators are one of the newest fields in condensed matter physics,

with innovative concepts that have been first developed by theoretical works and that have been later experimentally verified in real materials like Bi_2Te_3. In topological insulators, electrons in edge states are described by Dirac equations and are topologically different from the bulk. These deep conceptual difference explains why the surface of topological insulators like Bi_2Te_3 is a particularly robust and efficient conductor, while only a few atomic layers underneath the surface the material is a normal insulator.

Strongly correlated materials are instead a classical problem of solid state physics, where many-body electron correlations play an essential role. These materials can present many phase transitions, often with a very complicated phenomenology whose interpretation in very challenging even for the most advanced theoretical models. In particular, V_2O_3 is a prototype material for the Mott transition, where the systems can go from an insulating to a metallic state without breaking the symmetry of the crystal, and only by changing external parameters like temperature or doping. The phase transition is of the first order, and consequently during its evolution it presents the coexistence of microscopic insulating and metallic domains whose nature only now starts to be studied.

In this thesis, I will present experimental results obtained using mainly two techniques based on photoelectron spectroscopy. The first one is TR-ARPES (time and angle resolved photoemission spectroscopy), which was able to distinguish the ultrafast surface carrier dynamics of the metallic surface states from that of the insulating bulk states in the 3D topological insulator Bi_2Te_3. And the second one is SPEM (scanning photoelectron microscopy), which was used to study the coexistence of metallic and insulating domains at the Mott transition in Cr-doped V_2O_3.

The manuscript is structured as follows:

Chapter 2 will give an introduction to the physics of topological insulators. I will first start to discuss this topic in the 2D case, with the purpose of facilitating the description of 3D topological insulators. Later, I will describe in more detail some experimental and theoretical work on the 3D system Bi_2Te_3, which is the material studied in this thesis.

Chapter 3 will focus on the description of the Mott transition. The first part of this chapter presents a theoretical overview of the Mott transition. The second part focuses on the description of the prototype Mott-Hubbard compound vanadium sesquioxide (V_2O_3) as well as on the recent experimental results obtained on this system using photoemission spectroscopy.

Chapter 4 will present a detailed description of the different experimental methods based on photoelectron spectroscopy: angle resolved photoemission spectroscopy (ARPES), time and angle resolved photoemission spectroscopy (TR-ARPES) and scanning photoelectron microscopy (SPEM). In particular an explanation will be given of how one can perform photoelectron spectroscopy with femtoseconde resolution in time, or nanometer resolution in space.

The following two chapters are devoted to the original results obtained during my doctoral work.

Chapter 5 will present the application of TR-ARPES to the study of the 3D topological insulator Bi_2Te_3 photoexcited with ultrafast laser pulses, showing how one can explore the carrier dynamics for both surface and bulk states, as well as the different scattering mechanisms between them. The lifetime of hot electrons in the Dirac cone can be widely enhanced by a preexisting subsurface band bending, leading to strongly out of equilibrium surface states.

Chapter 6 will present a photoemission microscopy study of $(V_{1-x}Cr_x)_2O_3$, providing the evidence of the coexistence of metallic and insulating domains at the Mott transition. The different origin and evolution of the metallic domains are discussed, and a comparison between the metallic state of the Cr-doped and of the undoped compound is shown.

Chapter 2

Introduction to 3D topological insulators: Bi_2Te_3

2.1 Introduction

2.1.1 2D and 3D topological phases

In condensed matter physics, phases of matter can be understood using Landau's approach, where all phases require a spontaneous breaking of some symmetry, like for instance translational symmetry in the crystalline state, rotational symmetry in magnetic phases and gauge symmetry in superconductors. However, in 1980, the first system was discovered that does not require breaking of a symmetry: the Quantum Hall (QH) state [1]. This system presents conducting, robust edge states: they do not disappear in presence of disorder. It was shown, soon after, that there is a topological order beyond the symmetry breaking and that this topological order explains the presence and the robustness of the edge states. This phase requires an intense magnetic field at low temperature, which means that the time reversal symmetry is broken. Afterwards, a new phase of matter with topological character was predicted and discovered in other 2D systems, presenting no time reversal symmetry breaking. In these systems the strong spin orbit coupling plays a crucial role in generating the topological phase, which is at the heart of the quantum spin Hall (QSH) state. These systems are insulating in the bulk, but

they differ from conventional insulators by the presence of robust conducting edge states, and from the QH states by the conservation of time reversal symmetry: they are called topological insulators [2, 3]. The QSH effect was theoretically predicted in 2D and later experimentally verified in the mercury/cadmium telluride quantum wells HgTe/CdTe [4, 5]. Soon after, this phase was also found in a 3D system, which represents another major difference with respect to the QH Effect. It was first proposed to be seen in Bi_xSb_{1-x} [6], then in usual semiconductors such as the family of compounds Bi_2Te_3, Bi_2Se_3 and Sb_2Te_3 [7]. It was seen experimentally by ARPES in Bi_xSb_{1-x} [8], Bi_2Te3 [9] and Bi_2Se_3 [10]. These compounds are characterized by robust metallic surface states described by a single Dirac cone, while they present normal semiconducting properties in the bulk.

2.1.2 Topological and ordinary insulators

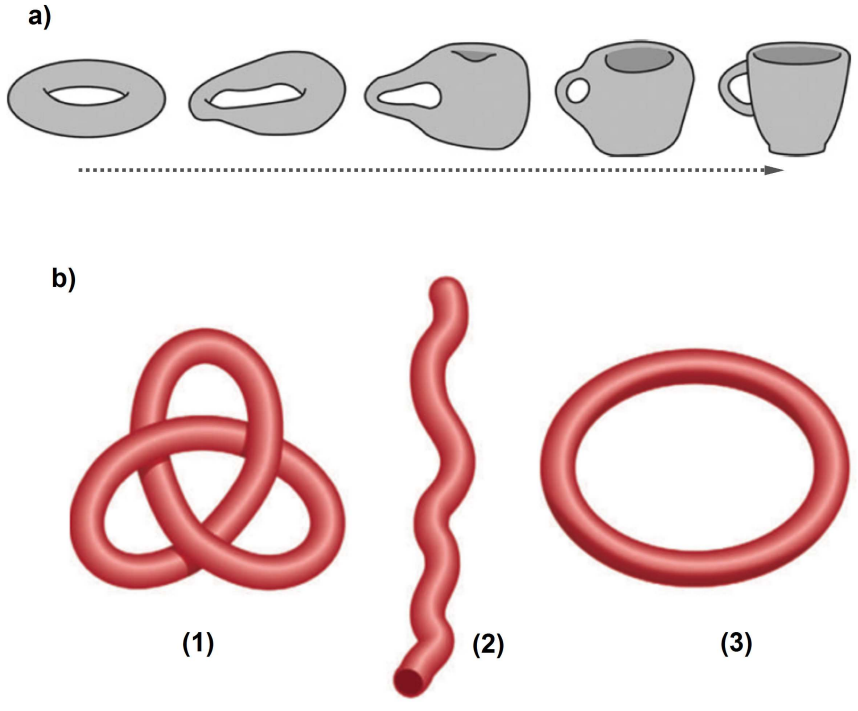

FIGURE 2.1: *a) Smooth deformation from a doughnut to a coffee cup. b) (1): the trefoil knot (2): the open string and and (3): the simple loop. From [11]*

It is possible to describe the topological insulators as insulators always possessing metallic edge (or surface) states when they are at the boundary with an ordinary

insulator or with vacuum [11]. But why is it called topological phase?

Topology is a branch of mathematics that studies the properties of objects that remain invariant under smooth deformation. An example of this invariant property can be found in objects of everyday life: for instance, the doughnut (Figure 2.1-a) can be smoothly deformed to give a coffee cup. Consequently, the doughnut and the coffee cup have the same topological properties. Another example is shown in figure 2.1-b: the open string (2) can be used to produce a trefoil knot (1) or a simple loop (3). But the trefoil knot and the simple loop do not have the same topological properties. It is not possible to deform either one to obtain the other one by stretching or twisting, unless one cuts them. In connection to our understanding of the topological phase, the trefoil knot can be thought of as a topological insulator while the simple loop is on ordinary insulator: at the interface, there must be an edge or surface where the knot is cut. This notion of knotting can be applied to understand the topological phase; in this case there is another kind of "knotting" corresponding to the electronic wavefunctions when they move through momentum space. The evolution of the topological wavefunctions is so complicated that they cannot be continuously changed to obtain those of ordinary materials.

2.2 Quantum Hall Effect: first topological phase

In 1980 Von Klitzing discovered the quantum Hall effect [1], which occurs when electrons confined to a 2D interface between two semiconductors are subject to a strong magnetic field at low temperature. The most remarkable resulting effect are quantized values of the Hall conductance:

$$\sigma = p\frac{e^2}{h} \tag{2.1}$$

Electrons in such a system end up with quantized circular orbits, and the energy levels of these quantized orbits take discrete values known as the Landau Levels (Figure 2.2-b).

$$E_n = (n + \frac{1}{2})\hbar w_c \tag{2.2}$$

where w_c is the cyclotron frequency. This description resembles that of an atom, where quantum mechanics replaces the circular motion of bound electrons by orbitals having quantized energies.

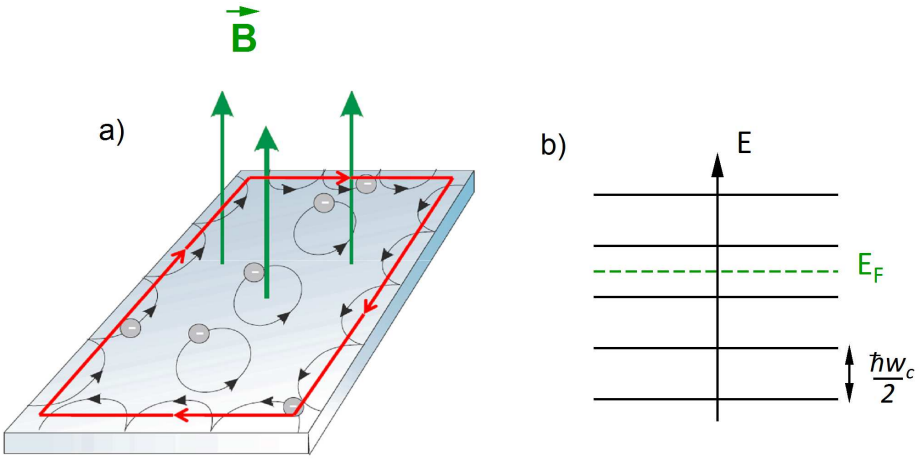

FIGURE 2.2: *a) The magnetic field effect on a two-dimensional electron gas. b) The Landau levels.*

A quasi-classical view of the effect of a magnetic field on a two-dimensional electron gas is shown in Figure 2.2-a. The electrons will follow closed orbits under the influence of the magnetic field, unless they meet an interface with an insulator (or vacuum) on which they reflect; this results in a different kind of motion following the edges of the sample. The confinement effect at the boundary pushes the Landau levels "up" in energy. As a consequence, Landau levels below the Fermi level cross in the sample edges and thus bring the electrons at the Fermi level, thus producing the edge channels responsible for the conduction. What's specific about these channel states?

As shown in the Figure 2.2-a, the edge states are unidirectional channels; an electron can travel only in one direction. An electron cannot be backscattered by the presence of an impurity, because there is no channel enabling the change of its direction (except through the entire sample). Backscattering is then forbidden, showing a dissipationless transport mechanism, which could be extremely useful for devices.

2.3 Spin Quantum Hall effect: 2D topological insulators

2.3.1 Description and edge states

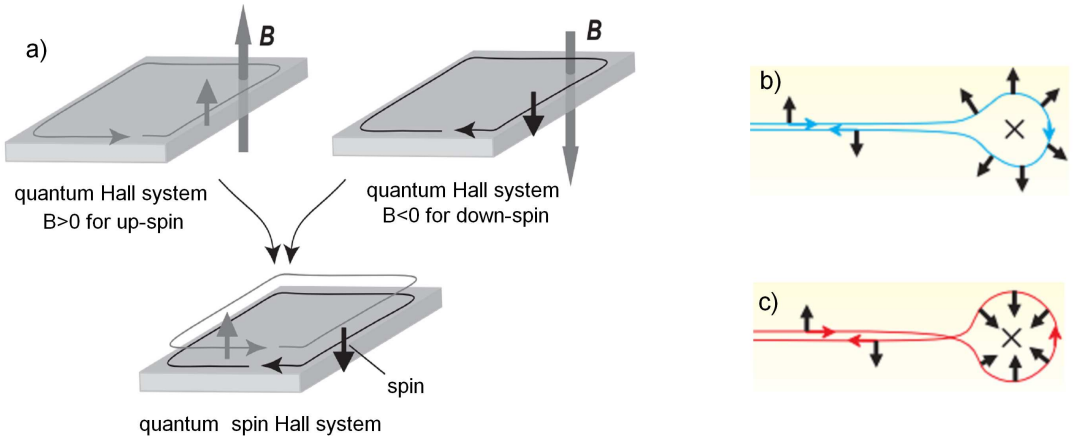

FIGURE 2.3: *a) The superposition of two QH effects to generate the QSH effect, from [12]. b)-c) The electron scattering with an impurity in an edge channel, from [13].*

Let us imagine a two-dimensional electron gas with all spins up (Figure 2.3-a), with a magnetic field which is generated and directed upwards: this will cause a quantum Hall effect, opening channels at all edges facing the same direction. Now let us imagine an electron gas with spin down, with the magnetic field in this case directed downwards, having edge channels rotating in the opposite direction with respect to those with spin up. By superposing these two images we obtain what is called the quantum spin hall effect (QSH). Obviously, it is impossible to apply an external magnetic field acting only on the electrons of a given spin. This effect can still be obtained in the absence of external magnetic field, in compounds of heavy atoms characterized by a strong spin-orbit coupling, such as mercury-cadmium telluride quantum wells HgTe/CdTe (see below). Due to the strong spin-orbit coupling, the electrons are subject to an effective magnetic field depending on their spin, which generates the Quantum Spin Hall Effect. Unlike for the QH effect, in the QSH effect the time reversal symmetry does not break.

Are the channels still protected as in the case of the quantum Hall Effect?

In fact, in this case the propagation channels in opposite directions are spatially

close, and one can imagine that an electron is released from one to the other by an impurity. But this is not possible. We should note that in the quantum spin Hall state, spin and wave vectors are locked, their directions are strongly related to each other. Figure 2.3-b-c describes the electron scattering with an impurity in an edge channel, as an exemple where spin and wave vector are perpendicular. When the electron bypasses an impurity to reverse direction, the wave vector rotates by π and the spin of the electron must also rotate by π. Or one can bypass the impurity by turning in two different directions: one is π (2.3-b) and the other is -π (2.3-c). The difference between these two paths is 2π.

Consider ψ_1 the wave function representing the state in which the electron is found after a rotation of π and ψ_2 after -π. The orbital part of the two wavefunctions is identical. These two states are separated by a rotation of 2π for the spin. But the spin is invariant under a rotation of 4π, the phase difference between ψ_1 and ψ_2 is therefore $\exp(i2\pi/2) = \exp(i\pi) = -1$. Thus, $\psi_1 + \psi_2 = 0$, which means that the two wavefunctions interfere destructively. The edge channels are therefore protected: no backscattering is allowed.

This construction is valid in the case of a non-magnetic impurity. Therefore, no time-reversal symmetry breaking is required to protect edge states (contrary to the case of the QH effect). This dissipationless transmission of the edge states makes QSH systems perfect candidates for spintronic applications.

2.3.2 Z_2 topological insulator

The QSH effects, presented above, have single pair edge states (forward and backward movers). If we assume that we have two pairs of edge states, then the electron can be scattered from one to the other without reversing its spin, hence without destructive interference: in this case there are no protected edge states. To get a robust edge state, the QSH state must have an odd number of pairs. This odd-even number is characterized theoretically by the so-called Z_2 topological number [14, 15], which is used also for 3D invariant topological systems.

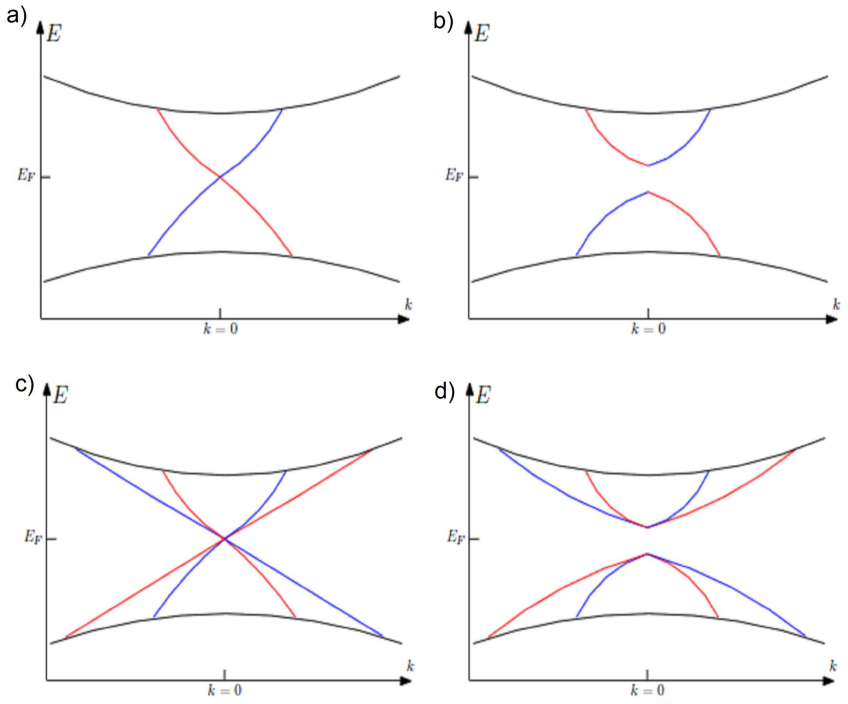

FIGURE 2.4: *a) gapless and b) gapped (forbidden) edge states in the case of a single Kramers' pair. c) gapless and d) gapped (not forbidden) edge states in the case of a two Kramers' pairs. The red and the blue colors show the dispersion of opposite spins. From Ref. [16]*

A more physical intuition of this number can be given via the notion of Kramers degeneracy, in which the edge state pair is known as a Kramers' pair: Kramers theorem tells us that for a system with an Hamiltonian that obeys a time reversal symmetry $[H, T] = 0$, where T is the time-reversal operator, all its eigenstates are at least twofold degenerate: if we have an eigenstate $\mid n \rangle$ with an energy E_n, then there exists a different state at the same energy $T \mid n \rangle \neq \mid n \rangle$. This remarkable theorem is due to the fact that the electron spin is half-integer: if we apply twice the time-reversal operator, $T^2 = -1$, this corresponds to a spin rotation of 2π. Indeed, if $T \mid n \rangle$ and $\mid n \rangle$ are equivalent we should write $T \mid n \rangle = a \mid n \rangle$, (with a complex number), which means that $T^2 \mid n \rangle = |a|^2 \mid n \rangle$ or $|a|^2 \neq -1$, which proves the twofold degeneracy.

Figure 2.4-a presents the case where we have a single pair of edge states, or one Kramers' pair, which means only one state is available for each spin; the crossing point is located at a time reversal-invariant point. Then gap opening (Figure 2.4-b) violates the Kramers theorem, since the state at k = 0 becomes non-degenerate.

Now if we have two possible states for each spin, or two Kramers' pairs (Figure 2.4-c), then each energy is fourfold degenerated and one can construct a gap without defiling the time reversal symmetry (Figure 2.4-d).

Therefore Kramers theorem allows the band structure to have a gapped state in the case where the system has an even number of Kramers' pairs. According to this notion, one defines the Z_2 topological invariant, ν, whose value of either 0 or 1 corresponds respectively to even and odd number of Kramers' pairs.

2.3.3 Example: Mercury Telluride quantum wells

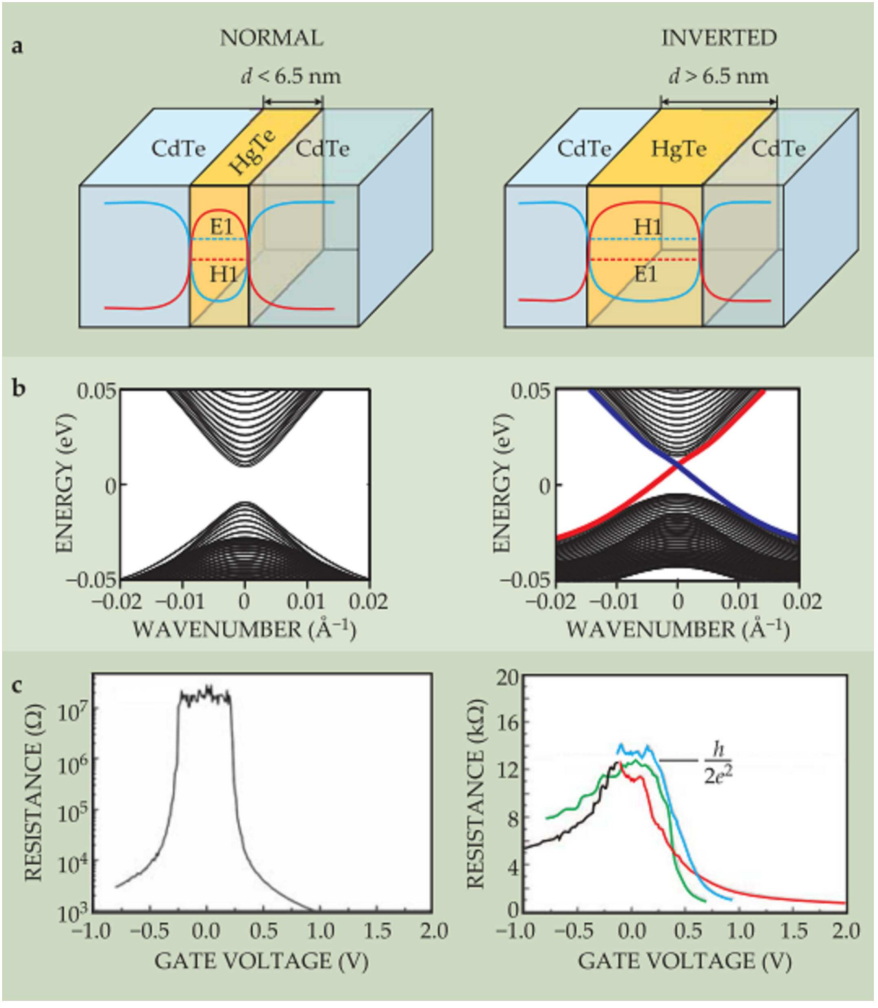

FIGURE 2.5: *a) A mercury telluride quantum well without and with band inversion. b) The band structure of a mercury telluride quantum well without and with band inversion. c) The transport measurement of the edge states for thin and thick values of the quantum well. From [13]*

The topological phase effects in mercury telluride quantum wells was first theoretically predicted in 2006 by Bernevig et al. [4] and later experimentally verified in 2007 by Knig et al. [5]. Mercury telluride quantum wells can be prepared by sandwiching Mercury Telluride (HgTe) between two Cadmium Telluride (CdTe) layers (Figure 2.5-a). The two compounds HgTe and CdTe have the same crystalline structure but present a slight difference in the lattice parameters. However, HgTe presents a strong spin orbit coupling (Hg is a heavy element) which results into band inversion for this system: the conduction band is of p character whereas the valence band has an s character.(CdTe presents the inverted situation, see figure 2.6). By increasing the HgTe thickness, i.e. by increasing its width d, the strength of the spin-orbit coupling increases. At a critical d value (predicted theoretically to have a value of 6.5 nm), the inversion of bands takes place. HgTe is not an insulator in the bulk (see figure 2.6). To make HgTe insulating one should force the opening of gap by contraction, i.e by making it grow on a substrate having a slightly different lattice parameter, which allows modifying the HgTe and thus the band structure. This is the role of CdTe substrate: the growth of HgTe on CdTe can impose the right strain necessary to open a gap in its bulk band structure. At the interface, the bands will be connected and this produces surface states with band crossing.

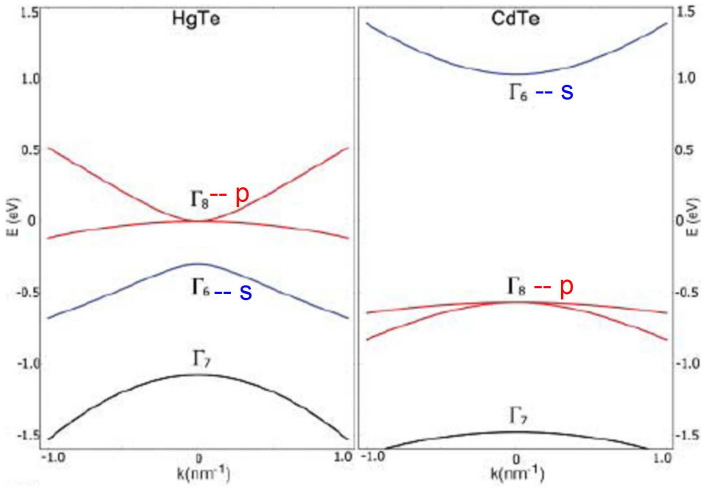

FIGURE 2.6: *The band structure calculations of HgTe and CdTe. from [4]*

These edge states are dispersing from the valence band to the conduction band

with opposite spin direction. The crossing point is located at a time reversal-invariant point, at which gap opening violates the Kramers theorem.
In 2007, the QSH effect was for the first time experimentally observed by Konig et al.[5]. The resistance measured for this quantum well is shown in figure 2.5-c: a nearly infinite resistance is observed in thin quantum wells, for d< 6.3 nm, while a quantized resistance with plateau R= $\frac{h}{2e^2}$ is observed for thick quantum wells d> 6.3 nm. However the resistance plateau is independent of the sample width, from 0.5 μm (red) to 1 μm (blue), showing that it is caused by edge states
Mercury Telluride quantum well is then a 2D topological insulator with metallic edge states protected by time reversal symmetry. These edge states are again (like in QH) realized by the contact between a topological insulator and an ordinary insulator. They are described by a single Dirac cone corresponding to a single Kramers' pair for each edge.

2.4 3D topological insulators

2.4.1 From 2D to 3D topological insulators

A 2D topological insulator is a material supporting a quantum spin Hall Effect. It is an insulator in the bulk, but its edges are conduction states protected by time reversal symmetry. In addition, the dispersion relation of the energy E of these states is linear with respect to the wavevector k; E (k) = $\hbar$kc (c is the speed of electrons), see figure 2.7-a, like the case of the mercury telluride quantum wells. This picture can be generalized to build a 3D system. In these systems spin-orbit coupling is again required for the inversion of bands. The boundary of the sample is no longer an edge but a surface. Edge states in one dimension must be replaced by surface states in two dimensions, and the dispersion relation becomes a cone E (k) = || k ||c, where k is a vector in two dimensions, as shown in Figure 2.7-b. These electrons behave like Dirac fermions and present all the interesting physical proprieties of these systems, protected again by time reversal symmetry. Each momentum along the surface has only a single spin state at the Fermi level, and

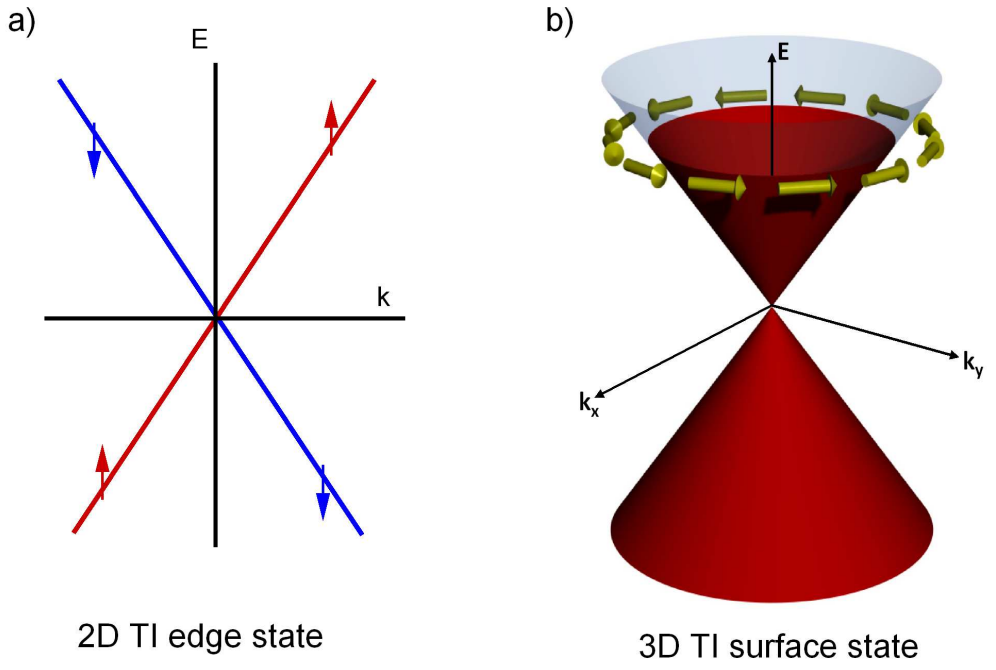

FIGURE 2.7: *a) Description of the edge states in 2D topological insulators. b) Description of the surface states in 3D topological insulators.*

the spin direction rotates as the momentum moves around the Fermi surface.

In the summer of 2006 three theoretical groups independently discovered that the topological characterization of the quantum spin Hall state has a natural generalization in three dimensions [6, 15, 17]. This phase was predicted in several real materials, including $Bi_{1-x}Sb_x$ [6], as well as strained HgTe. Using ARPES (angle resolved photoemission spectroscopy), in 2008, Hsieh et al. reported the experimental discovery of the first 3D topological insulator in $Bi_{1-x}Sb_x$ [8]. In 2009, Zhang et al predicted that Bi_2Te_3, Bi_2Se_3 and Sb_2Te_3 are 3D topological insulators whereas the related material Sb_2Se_3 is not [7]. Soon after Bi_2Te_3 and Bi_2Se_3 were identified experimentally as 3D topological isulators by Chen et al [9] and Xia et al [10] via ARPES.

2.4.2 Comparison with graphene

Graphene, which consists of a single layer of carbon atoms, see figure 2.8-a, is a 2D material and is one of the most studied topics in nowadays physics [18]. In

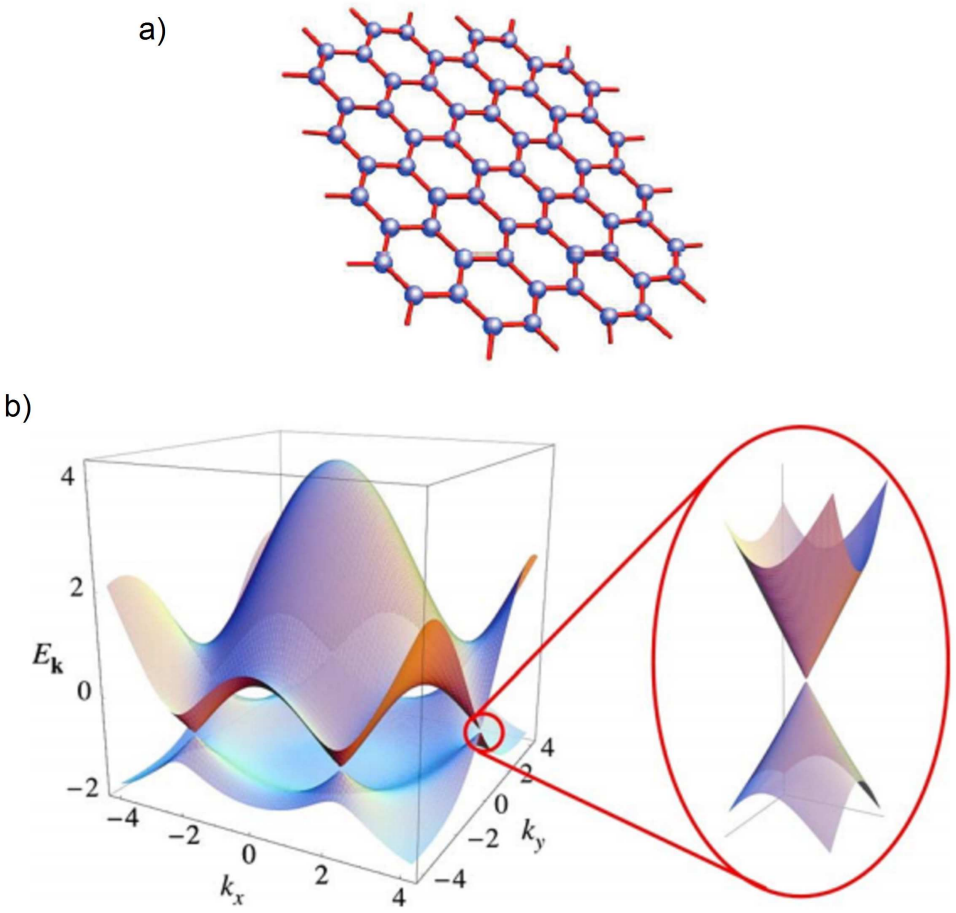

FIGURE 2.8: *a) Single layer of carbon atoms. b) Electronic structure calculations of graphene, from [18].*

k-space, the dispersion of its bands is described by two cones in each Brillouin zone that meet at discrete Dirac points at the Fermi level, figure 2.8-b. What's the difference between graphene and the surface states of a 3D topological insulator? The main difference between topological insulators and graphene is that the topological insulator possesses a single Dirac cone in the Brillouin zone, whereas graphene has two. The Kramers theorem, as we explained above, shows that for a material having an even number of electrons that obey time reversal symmetry, the degeneracy of states can be lifted. For this reason Dirac cone in topological insulators is protected (due to its odd number of Kramers' pairs) while in graphene it easily destroyed (due to its even number of Kramers' pairs): it is easy to generate a gap in graphene by application of external electric field or by distortion of the two carbon atoms in one unit cell.

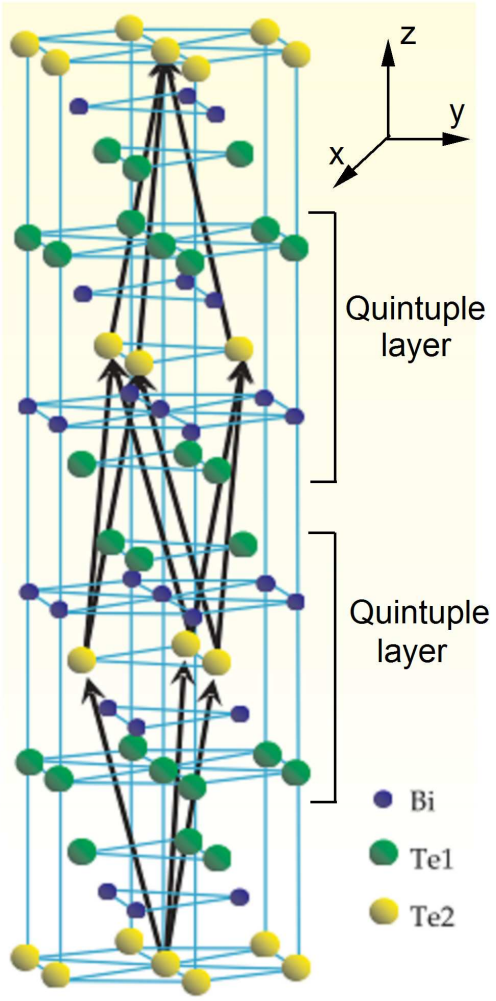

FIGURE 2.9: *The crystal structure of Bi_2Te_3. From [13]*

2.4.3 The 3D topological insulator Bi_2Te_3

In chapter 5 I will present experimental studies of ultrafast surface carrier dynamics in several bismuth chalcogenide topological insulators (Bi_2Te_3, $Bi_{2.2}Te_3$). In this paragraph I will present some previous experimental and theoretical works on Bi_2Te_3.

2.4.3.1 Crystallographic structure

Figure 2.9 shows the crystal structure of Bi_2Te_3. It presents a rhombohedral crystal structure with the space group $R\bar{3}c$. The crystal is formed by quasi 2D layers arranged along the z-direction or the [111] direction, known as quintuple

layers (Te-Bi-Te-Bi-Te). The coupling is strong between two atomic layers within one quintuple layer but it is much weaker (van der Waals type), between two quintuple layers.

2.4.3.2 Electronic band structure

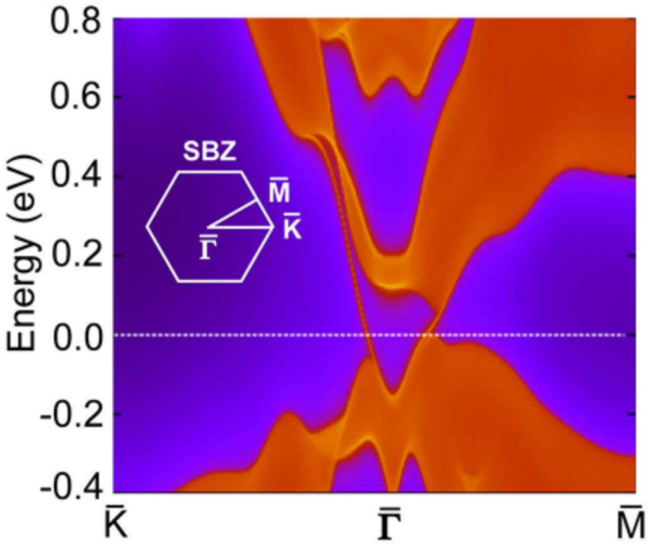

FIGURE 2.10: *The band structure calculation of Bi_2Te_3 by Zhang et al. [19]*

Figure 2.10 presents the calculated electronic band structure in Bi_2Te_3 on the (111) surface of the rhombohedral crystal as obtained by Zhang et al in 2009 [7]. This calculation predicted that the undoped Bi_2Te_3 is an insulator in the bulk with a direct gap of 0.3 eV and indirect gap of 0.165 eV. The surface states for this system are described by a single surface Dirac cone at the Γ point (k = 0) in the surface Brilloiun zone (SBZ). In figure 2.10 they are represented by a red line dispersing from the valence to the conduction band, which merges in the conduction band above the Dirac point at around 0.1 eV in the ΓM direction and around 0.5 eV in the ΓK direction. However, the surface states around the Γ point overlap in energy with the bulk valence band, contrary to the other compounds Bi_2Se_3 and Se_2Te_3, where the Dirac point is within the gap.

2.4.3.3 Photoemission spectroscopy

The charge transport experiments, which were successful in identifying HgTe as a 2D topological insulator, are problematic in 3D materials because it is difficult to separate the surface contribution to the conductivity from that of the bulk. As it will be explained in chapter 4, ARPES (angle resolved photoemission spectroscopy) is a very powerful technique to experimentally determine the electronic structure by measuring electrons photoejected from the solid. Due to its surface sensitivity, this technique can well probe surface states and discriminate them from the bulk state. In particular, high-resolution ARPES performed with modulated photon energy allows to discriminate surface states from bulk 3D band structures, because surface states do not disperse along a direction perpendicular to the surface, whereas bulk states do. For this reason ARPES is an ideal tool to probe surface states.

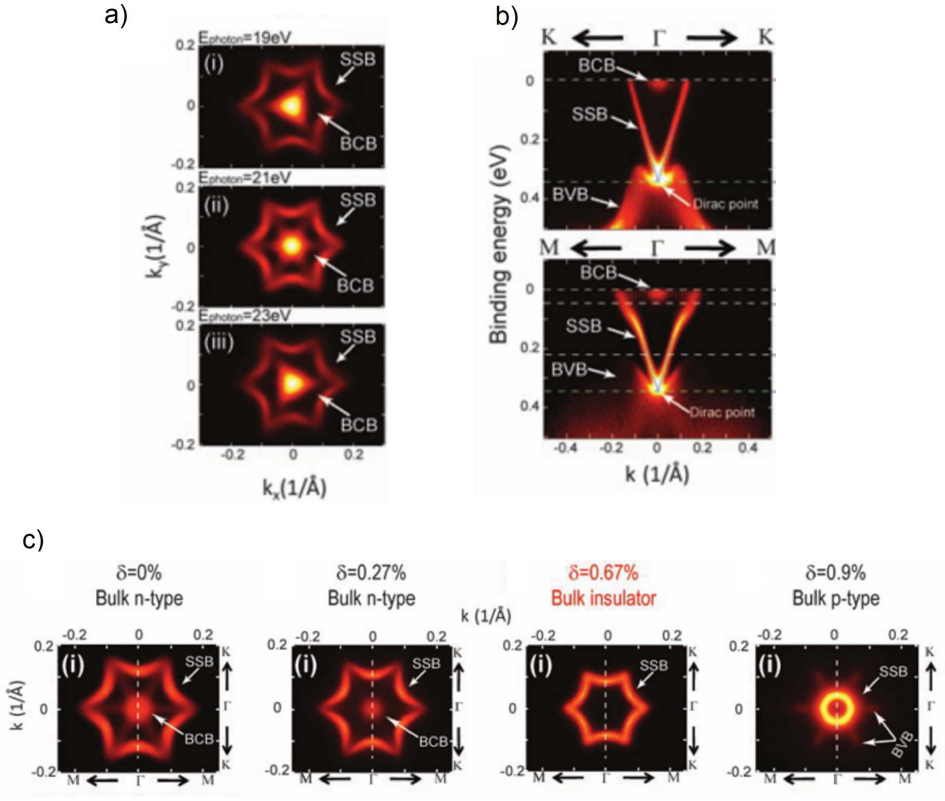

FIGURE 2.11: *a) Evolution of the Fermi surface in Bi_2Te_3 as a function of the photon energy (19, 21 and 23 eV). b) ARPES measurements in Bi_2Te_3 along ΓM and ΓK direction. c) Evolution of the Fermi surface for different hole concentrations δ. [9].*

The ARPES measurement performed by Chen et al. in 2009 [9] at 21 eV for the undoped Bi_2Te_3 is shown in figure 2.11. Figure 2.11-a shows the Fermi surface at different photon energies (19, 21 and 23 eV): by varying the photon energy, the bulk states (BCB) disperse from a left-pointing triangle to a right-pointing triangle, as a result of different values of the momentum k_z. The hexagram Fermi surface (SSB) remains instead unchanged due to its purely 2D structure, and confirms that it is a surface state for this system. The surface states are characterized by a single Dirac cone at the Γ point, consistently with the band structure calculation performed by Zhang et al. This measurement showed that the undoped Bi_2Te_3 is n-type bulk, see figure 2.11-b.

We can also notice that there is a deviation of the surface states dispersion from the expected linear behavior. This effect is measured in ARPES by changing the Fermi level position within the gap, using different hole doping concentration δ ($Bi_{2-\delta}Sn_\delta Te_3$): the Fermi surface evolves from an hexagon to a pure circle, see figure 2.11-c. This effect is known as hexagonal warping of the surface states, and it was confirmed also by STM measurements [20]. At δ=0.67, pure surface states without conduction band were measured: the Fermi level could be tuned to intersect only the surface states, indicating fully gapped bulk states as is expected for a 3D topological insulator.

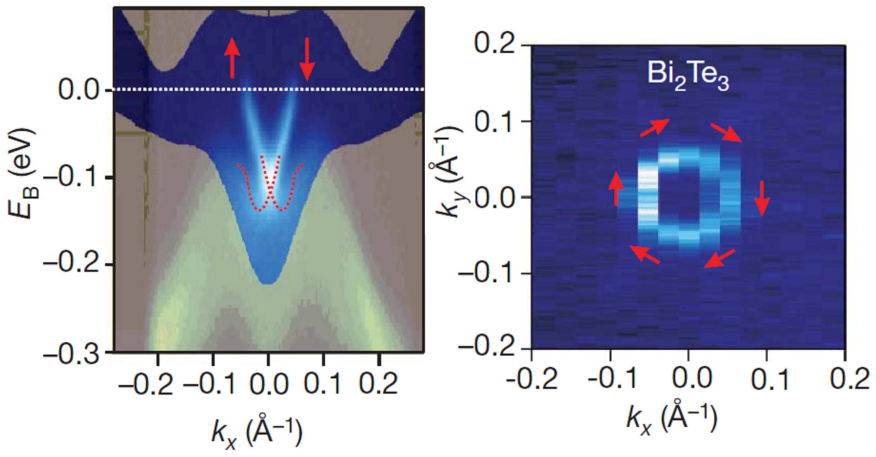

FIGURE 2.12: *a) ARPES experiment of Bi_2Te_3. b) The winding of the spin projection around the Fermi surface. From [8]*

Besides the dispersion relation of the surface (and bulk) states via ARPES, photoemission experiments can also probe the spin of the extracted electron (spin

resolved photoemission spectroscopy). The experimental plots presented in Figure 2.12-a show the unicity of the surface states, and the winding of the electron spin around the Fermi surface (figure 2.12-b) [8].

2.4.3.4 Scanning tunnelling microscopy

In addition to ARPES, another experimental technique well adapted to probe surface states is scanning tunneling microscopy (STM) [21]. The STM is the most powerful tool to directly study the electron density on the surface of materials with atomic resolution: by applying a bias voltage between a metallic tip brought within atomic distance from the sample and its surface, one can tunnel electrons from the sample to the tip and vice versa. By scanning over the sample surface, one can collect the tunneling current as a function of tip position; at a set tunneling current, one can determine the surface morphology. In addition, information on the electronic structure at a given location in the sample can be given by the measuring of the differential tunneling conductance dI/dV, which is directly proportional to the Local Density of States (LDOS): it consists in adding some oscillatory voltage (dV) on top of the bias voltage and measuring the response (dI). This type of measurement is called scanning tunneling spectroscopy (STS). With STM one can compare the LDOS in different points on the surface sample: for example, LDOS at an impurity site can be compared to the LDOS far from impurities.

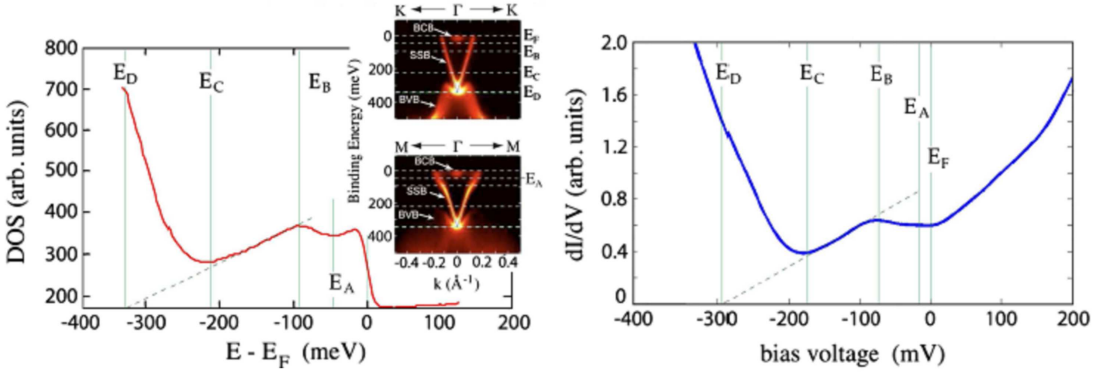

FIGURE 2.13: *Comparison of the integrated density of states obtained from ARPES measurements (left) and STM measurements (right). From [20]*

By measuring the LDOS from impurities and steps on the surface, the backscattering in Bi_2Te_3 was detected by STM [19, 20]: the interference patterns near defects

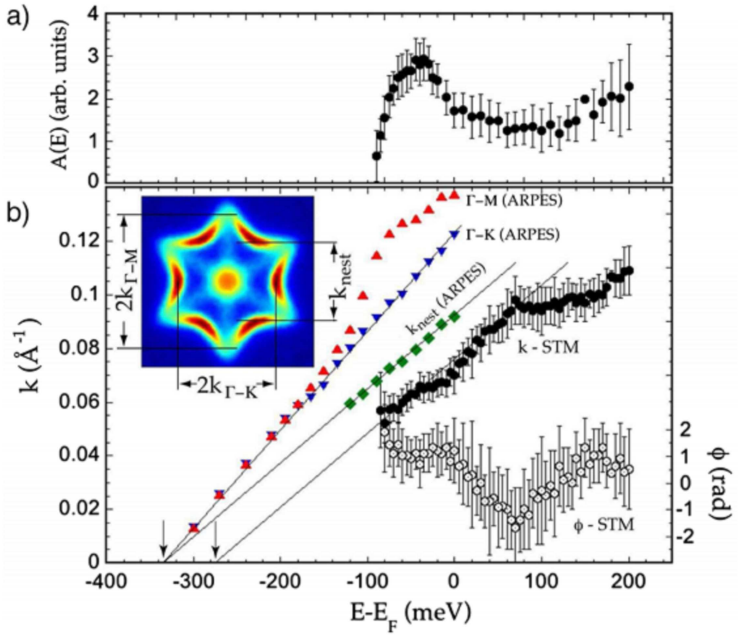

FIGURE 2.14: *The STM measurement: the parameters oscillation of the DOS (averaging of the LDOS), as a function of the bias voltage, from [20]*

or steps on the surface show that electrons are never completely reflected when scattered.

A comparison between ARPES and STM experiments was done in Bi_2Te_3[20]. The integrated density of states derived from ARPES experiments [9], see figure 2.13-a, is in good agreement with the STM measurements, see figure 2.13-b. Also, another point in which STM is consistent with ARPES measurements is the presence of the hexagonal warping of the surface states, as discussed above. This propriety is confirmed by the presence of oscillations in the STM measurements done on a surface with atomic steps [20]. In fact, by analyzing the average LDOS as a function of the distance between steps, an oscillations is absent in the case where we have a pure Dirac cone [22]. In the case of the Bi_2Te_3, in contrast, these oscillations are observed at 100 meV, see figure 2.14, where the Fermi surface turns from concave to convex, proving the existence of warping in the Dirac cone.

Chapter 3

Mott-Hubbard transition in V_2O_3

3.1 Introduction to Mott metal-insulator transitions

3.1.1 Metal-insulator transition

The metal-insulator transition in solids is experimentally identified by a huge resistivity change. It is widely observed in many systems due to many different effects. In some cases, it is due to a purely electronic many body effect, the Anderson localization, where the formation of the insulating state is a result of strong disorder, which corresponds to a total absence of scattering [23]. It other cases it can be described by the interaction of the electrons with an effective periodic potential, produced by the positive ions and the other electrons, described in the framework of band structure theory. This latter description is valid for many materials with large bands, where electron-electron interactions can be neglected. However, there are various examples of materials presenting transitions that cannot be understood within this framework. In 1934, de Boer and Verwey [24] reported that many properties of some transition metal oxides were in disagreement with band structure theory: these materials are insulators whereas they are expected to be conductors because of their partially filled d-band. The mechanism leading to the insulating phase was later understood by Mott [25, 26]. Indeed, these materials present small values of the bandwidth for the bands close to the Fermi energy

(narrow d-bands); this implies that the ratio of the Coulomb repulsion energy between the electrons and the available kinetic energy becomes larger. In such cases, the effects of correlations between the motions of individual electrons become important. Delocalization of electrons over the whole solid would lead to an energetically unfavorable condition. This implies that electrons should remain localized to their parent atomic sites. If this happens to all electrons close to the Fermi level, the solid becomes an insulator and such insulators are therefore called **Mott insulators**.

A change in electron correlations, without spontaneous symmetry breaking, can be sufficient change to the balance between itinerant and localized electrons on the preexisting atomic sites. When the localized character and the itinerant character coexist a metal-insulator transition is predicted: this transition is called the **Mott metal-insulator transition**. It is a first order transition induced by electron correlations, where in the insulating phase the electrons are localized on the existing ionic lattice. In this chapter, I will first present a theoretical description of this phenomenon, within the framework of the Hubbard model and of Dynamical Mean Field Theory (DMFT). I will then focus on the description of a prototype Mott-insulator system, the vanadium sesquioxide (V_2O_3). A detailed analysis of the novel experiments performed on V_2O_3 will be given in chapter 6.

3.1.2 Mott-Hubbard transition

The modelization of the Mott transition is very challenging to be handled theoretically. It requires treating individually and in a non-perturbative way the electronic correlations, which amounts to solving a many-body problem. One of the simplest models describing this transition is the Hubbard model [27–29] where a single atomic orbital is taken into account:

$$H = \sum_{i,j;\sigma} t_{i,j} c^{\dagger}_{i,\sigma} c_{j,\sigma} + U \sum_{i} n_{i,\uparrow} n_{i,\downarrow} \tag{3.1}$$

$n_{i,\sigma}$ represents the number occupation of the site i, with the spin σ.
Localizing the electrons on an atomic site costs a $z^*t_{i,j}$ kinetic energy per electron, where $t_{i,j}$ describes the hopping between orbitals on neighboring atomic sites i and j, and z is the number of the neighboring atomic sites. But moving an electron from a site i to its neighbor j, thus creating an empty site i with a doubly occupied site j, costs a correlation energy called U. However, considering just the interaction on-site is an approximation that is justified only if the Coulomb potential is sufficiently screened, i.e. in the metallic phase, and ignores the long-range interaction in the insulating phase.
The Hubbard hamiltonian has been used in numerous studies to describe in the easiest way correlation effects in metals, and more precisely the competition between kinetic energy and correlation energy. The treatment of this Hamiltonian is simple in two limits:

- The *non interaction limit* $U/z^*t_{i,j} \rightarrow 0$: a limit describing the metallic phase where no interaction between electrons is present and the systems is well described by band structure theory.

- The *atomic limit* $z^*t_{i,j}/U \rightarrow 0$: electrons are localized in on-site atomic orbitals describing an insulating phase, where each atom has two energy levels; the first corresponds to a simple occupation (E= 0) and the second to a double occupation (E= U).

When $z^*t_{i,j}/U$ increases, the atomic levels widen until they form overlapping strips. There is then a transition to a metallic state. If the idea at the basis of this physical phenomenon is clear, its precise description remains difficult because the transition occurs for intermediate values ($U \sim z^*t_{i,j}$). Although very simple compared to physical reality, it is difficult to solve this Hamiltonian, especially in the intermediate regime where competition between itinerant and localization due to correlations is more subtle. Only the one-dimensional case was solved exactly by Lieb and Wu in 1968 [30]. The results in one dimension are very specific and cannot be extended to higher dimensions. It should also be noted that the insulator-metal transition takes place only in the case of a half-filled band (one

electron per single atomic orbital), which is not the case in d-like electrons systems, where a partial degeneracy of the orbitals caused by the crystal-field is present, like in the vanadium sesquioxide V_2O_3.

One understands the problem resolving of the Hubbard Hamiltonian to describe the metal-insulating transition in the intermediate case, when the localized character and the itinerant character coexist. In such cases, the electrons hesitate between being itinerant and being localized. Among the various attempts of handling this problem, it is worth citing at least two theoretical models: the first one is the Gutzwiller method, where a variational approach was included to account for electronic correlations [31, 32]. The second one is Dynamical Mean-Field Theory (DMFT) [33–35], describing the electronic correlation from the low to intermediate energy scale. It has been developed over the last fifteen years and has led to some significant advances in our understanding of the Mott-Hubbard transition.

3.1.3 Mott transition in the DMFT approximation

Dynamic mean-field theory reduces a great number of degrees of freedom to a single-site effective problem; that is the dynamics at a given site in the real lattice can be thought of as the interaction of the local degrees of freedom at this site with an external bath created by all other degrees of freedom on other sites, figure 3.1.

The Green's function : The key quantity on which DMFT focuses is the local Green's function at a given lattice site:

$$G^{\sigma}_{i,i}(\tau) \quad = \quad -\langle \Psi_0 | T c_{i,\sigma}(\tau) c^{\dagger}_{i,\sigma}(\tau) | \Psi_0 \rangle \tag{3.2}$$

$|\Psi_0\rangle$ describes the ground state.

To understand the physical interpretation of the Green's function we consider a system with N body problem and we insert one electron at t=0: $c_k{}^{\dagger}|\Psi_0\rangle$. The state of the system at time t is:

$$e^{-iHt}\ c_k{}^{\dagger}|\Psi_0\rangle = |\Psi(t)\rangle$$

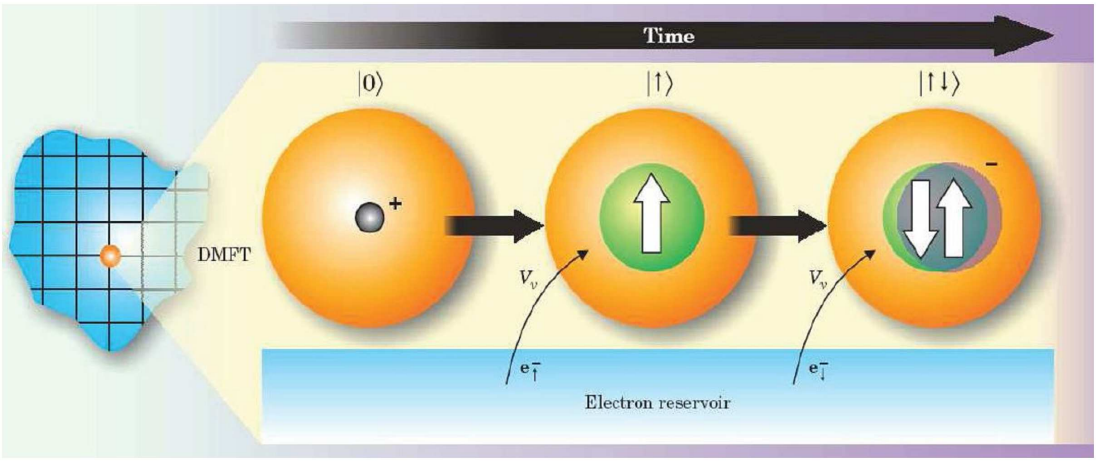

FIGURE 3.1: *A schematic configuration of the DMFT approximation: the local dynamics of the on-site atomic in the real crystal is thought as the dynamics of an impurity atom interacting with an external effective bath of electrons. The impurity atom can flip between different configuration $|0\rangle$; $|\uparrow\rangle$; $|\downarrow\rangle$ and $|\uparrow\downarrow\rangle$,* [35]

One takes now the same N-system and we insert one electron at the same time t:

$$c_k{}^\dagger \, e^{-iHt}|\Psi_0\rangle = |\Psi_e(t)\rangle.$$

The Green's function is a direct measurement of the overlap between $\Psi_e(t)$ and $\Psi(t)$:

$$\langle\Psi_e(t)|\Psi(t)\rangle = \langle\Psi_0 \, e^{iHt} \, c_k|e^{-iHt} \, c_k{}^\dagger\Psi_0\rangle = -i \; G(k,t)$$

-*For a system without interaction:* $\Psi(t)$ evolves in time without mixing with the other excited states, indicating a coherence state after the injection of one electron. The overlap $\langle\Psi_e(t)|\Psi(t)\rangle$ is just a time invariant phase.

-*For a system with interaction:* $\Psi(t)$ is the decomposition of the set of the other excited states, which have evolved differently, indicating the loss of coherence of this state after the injection of one electron. Thus the overlap $\langle\Psi_e(t)|\Psi(t)\rangle$ is no longer a simple phase but decreases with time. This loss of coherence decay can be described by the lifetime of a coherent entity, propagating like a particle, called "the quasiparticle".

The DMFT approximation : The representation of a single atom coupled to an effective bath, figure 3.1, can be described by the Anderson impurity model

[36] (the impurity solver). We can define a local self-energy from the interacting Green's function as:

$$\sum_{(imp)}(\mathrm{iw}_n) = {G^{-1}}_0(\mathrm{iw}_n) - {\mathrm{G}^{-1}}_{(imp)}(\mathrm{iw}_n)$$

${G^{-1}}_0(\mathrm{iw}_n)$ is an initial guess of the effective bath (an electron gas without interactions).

The approximation of the DMFT theory is that the real lattice self-energy coincides with the impurity self-energy. In real space, this means that we neglect all non-local components of $\sum_{(i,j)}$ and we approximate the on-site one by $\sum_{(imp)}$:

$$\sum_{(ii)} \sim \sum_{(imp)} \; ; \sum_{(i,j)} \approx 0$$

The $\sum_{(imp)}$ is used in order to obtain the local Green's function of the original lattice model, that's used to determine a new ${G^{-1}}_{0,new}(\mathrm{iw}_n)$ of the effective bath which is injected again into the impurity solver. The procedure is iterated until convergence is reached (self-consistency method). All the physical proprieties describing the Mott transition will be given by the converged Green's function and the self energy as I will explain in the next paragraph.

3.1.3.1 DMFT description

The distinctive aspect of DMFT is that it treats both the coherent excitations at low energy corresponding to the quasiparticle peak and the incoherent excitations at higher energy corresponding to the Hubbard band. As a result, it is able to describe the Mott transition by the transfer of the spectral weight between the quasiparticle and the Hubbard bands as a function of temperature, coupling strength, or other external parameters (doping, pressure...).

-***The low-energy scale (the quasiparticle peak)***: The notion of quasi-particle is derived from the Landau theory of Fermi liquids (correlated metal). The basic idea is that even if bare interactions between particles are very strong, it may be that the low energy excitations of the system can be well described by the

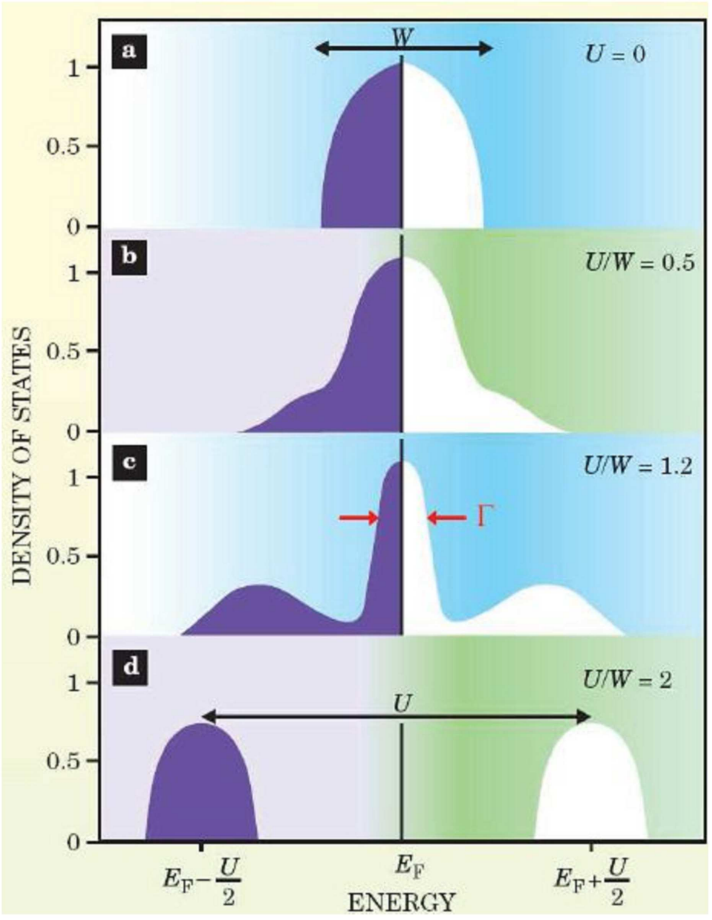

FIGURE 3.2: *Evolution of the calculated spectral density D.O.S at null temperature as a function of different electronic correlations U versus the band width W: a) Without interaction the systems is metallic, the DOS is the same of a metal band. b) At small correlations, a quasiparticle describing the correlation at low energy is present. c) At strong correlations three peaks are observed: the quasiparticle, and the two Hubbard bands (LHB and UHB). d) At very strong correlation the Fermi surface is destroyed: the quasiparticle peak has disappeared and the system is insulating, from* [35]

combination of elementary excitation modes. At low energy scale, a small number of these modes is involved, so that the interactions between these modes can be treated by methods of weak coupling due to their low density. Each particle is "dressed" by the interactions to give a new entity called **quasiparticle**. This low-energy coherence scale is given by Z^*D (with D the half-bandwidth), where Z is the quasiparticle weight given by the real part of the self energy. The lifetime of the quasiparticle ($\sim 1/\Gamma$), see the c case in the figure 3.2, is given by the imaginary part of the self energy. Close to the Mott transition, where a strongly correlated metal is present, $Z << 1$ and the quasiparticle coherence scale is strongly reduced.

-***The high-energy scale (The Hubbard bands)*** : In addition to low-energy coherence scale, the one particle spectrum of a strongly correlated metal contains high-energy excitations with spectral weight *1-Z*. These are associated to the atomic-like transitions corresponding to addition or removal of one electron from an atomic site.

The density of states (DOS), given by the spectral function A (**k**,w) = -1/π ImG(**k**,w), is predicted to have a three-peak structure: a quasiparticle band close to the Fermi energy surrounded by lower and upper Hubbard bands, see c case in figure 3.2. Towards the transition, a transfer of the spectral weight from the quasiparticle to the Hubbard bands is present; from the 2-c case to the 2-d case in figure 3.2.

3.1.3.2 Application to real materials: LDA+DMFT

A limited number of materials are poised right on the verge of the electronic instabilities. This is the case, for example of $(V_{1-x}Cr_x)_2O_3$ [37], the organic conductors, and also $NiSe_{2-x}Se_x$. These materials are particularly interesting for the fundamental investigation of the Mott transition, since they offer the possibility of going from one phase to the other by varying some external parameter (e.g chemical composition, temperature, pressure...). In its more essential version, DMFT does not account in detail for all the subtle electronic properties observed in the vicinity of the transition, nor for the diversity that appears in the physics of these systems. Its application to real materials requires the electronic structure of the system under consideration. In this context, a more realistic theory is represented by the calculation of DMFT band structure obtained by one-electron *ab initio* approaches such as Density Functional Theory (DFT Density-Functional Theory) within the local density approximation (LDA local-Density approximation). This approach allows calculating the band structure by the local electronic density which minimizes the functional energy. It's a self-consistent method using the Khon-Sham potential [38]. The LDA was an approximation to determine the exchange correlation parameter in the Khon-Sham potential by assuming a homogeneous gas

with the same density. The combination of LDA band structure calculations with the DMFT approximation is called LDA + DMFT [39, 40].

3.2 Prototype Mott-Hubbard system: $(V_{1-x}Cr_x)_2O_3$

Since its discovery by McWhan et Remeika [41] in 1970, vanadium sesquioxide has been the subject of, extensive experimental and theoretical studies for now more than four decades. It is considered as the prototype of a compound that undergoes a Mott-Hubbard metal-insulator transition.

3.2.1 Basic description

3.2.1.1 Phase diagram and resistivity

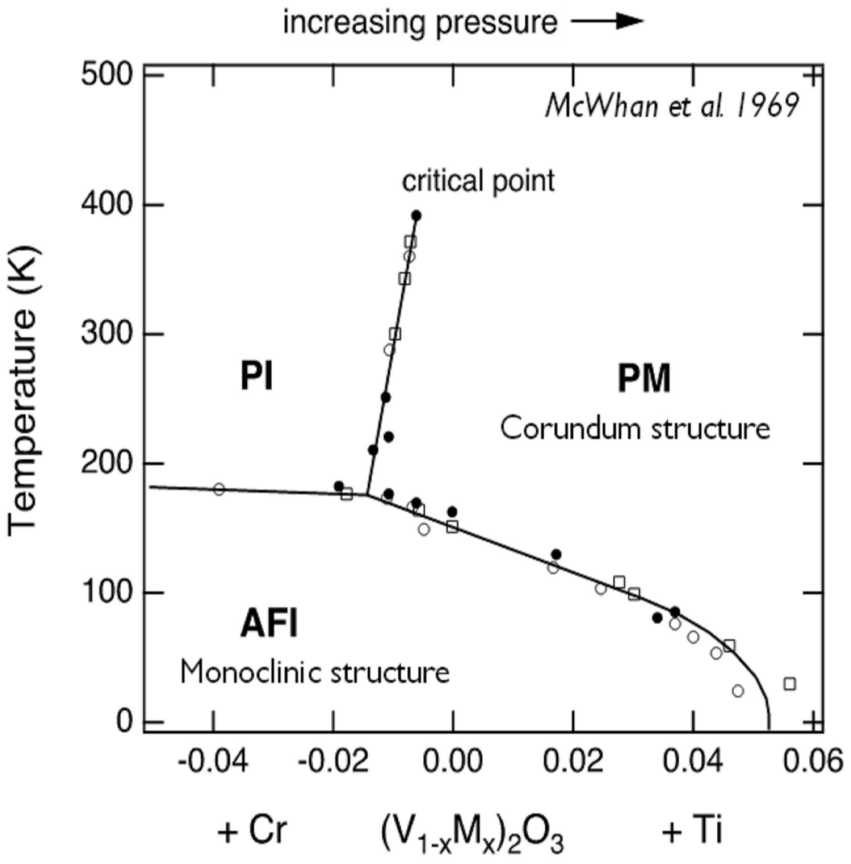

FIGURE 3.3: *Phase diagram of $V_{1-x}Cr_x)_2O_3$: temperature versus pressure or M-doping concentration (M= Cr; Ti), data points from* [42]

In figure 3.3, we show the phase diagram of V_2O_3, as a function of temperature versus doping. The V_2O_3 is metallic at room temperature with the corundum crystal structure. By cooling down below 150 K, an antiferromagnetic order appears with a monoclinic structural distortion, and the system becomes insulating. Alternatively, the system can be tuned by chemical substitution $(V_{1-x}M_x)_2O_3$: doping with chromium (M=Cr) is equivalent to a negative pressure, which effectively decreases the c/a lattice constant ratio, while doping with titanium (M=Ti) is equivalent to positive pressure. Above the Neel temperature (180 K), the crystal structure does not change from its corundum configuration as a function of pressure or doping. As a function of the temperature and for small Cr-doping, $(V_{1-x}Cr_x)_2O_3$ undergoes a first order paramagnetic metal (**PM**) to paramagnetic insulator (**PI**) transition. The latter is considered as a prototype of the Mott-Hubbard transition, because one can go from an insulating to a metallic phase without any change in crystal structure and in magnetic order.

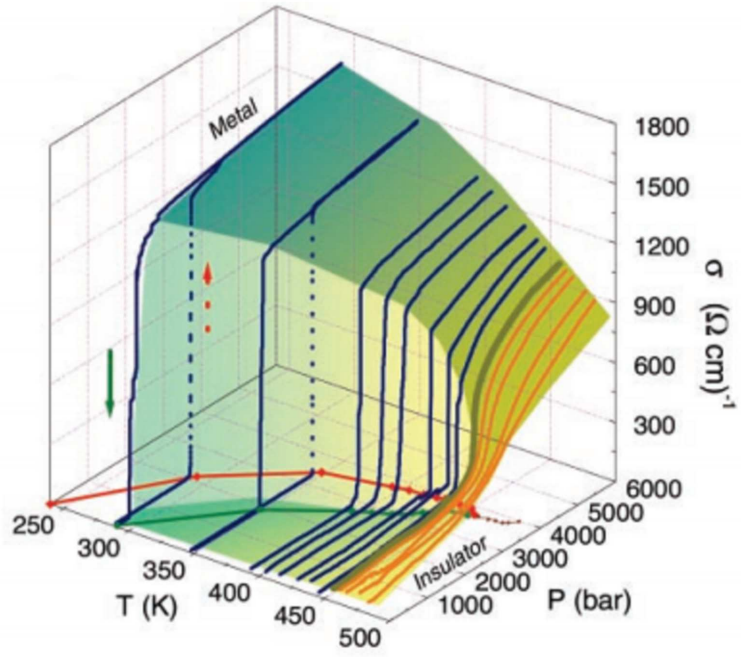

FIGURE 3.4: *The resistivity measurement in $(V_{1-x}Cr_x)_2O_3$, (x=0.011), data points from* [43]

Figure 3.4 presents the resistivity measurement in the Cr-doped compound (x=0.011), as a function of the pressure and at different temperatures [43]. This transition is characterized by a large hysteresis, corresponding to the first order character on

this system. The two lines of this first order transition (green and red lines) end in critical point at (Tc= 457.5 K and Pc= 3738 bar) and correspond to a smoothing into a crossover region, as shown also in the phase diagram, where there are no discontinuous variations of the resistivity.

This thesis considers the study, as a function of the temperature, of the phase transition in $(V_{1-x}Cr_x)_2O_3$; x = 0.011, compared to undoped V_2O_3.

3.2.1.2 Crystallographic structure

The PM or PI phase has the corundum crystal structure, formed by a hexagonal close packing of oxygen atoms ABAB, with 2/3 of its octahedral sites occupied by vanadium atoms. The space group is $R\bar{3}c$. The unit cell has a rhombohedral system (the primitive unit cell) or the hexagonal system, see figure 3.5-a. The octahedra (VO6) have a trigonal distortion [44], and the connection among them is done by sharing edges in the same layer (AB) and by pooling of faces and vertices between successive layers, see figure 3.5-b.

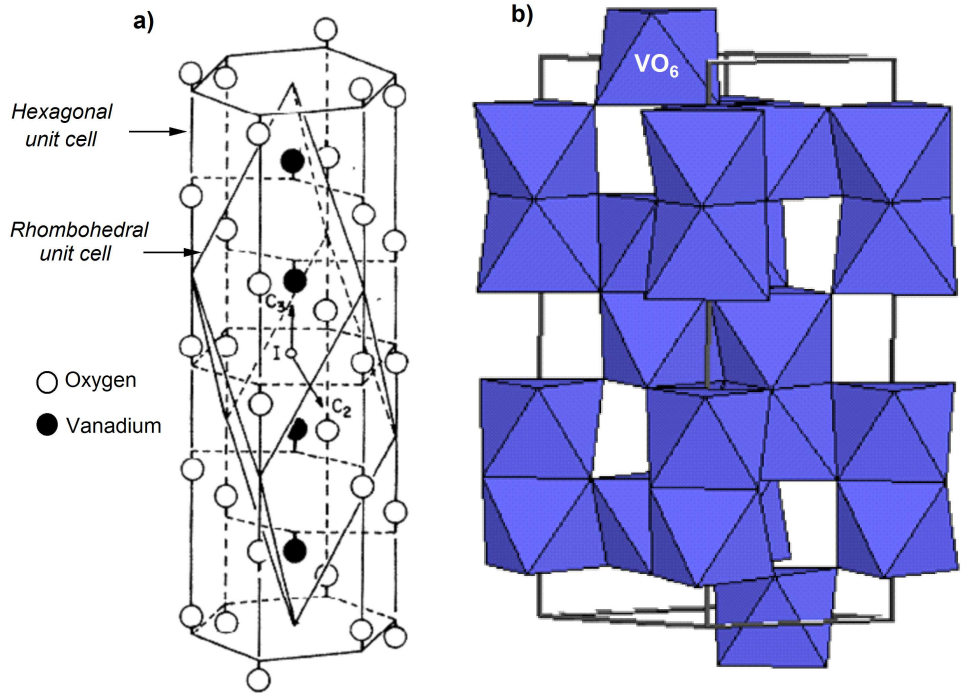

FIGURE 3.5: *a) Representation of the rhombohedral and the hexagonal unit cell in the corundum crystal structure of V_2O_3, from* [41] *. b) Rearrangement of the octahedrons (VO6) in the hexagonal system, from* [45]

In figure 3.6, I show the evolution, as a function of the temperature, of the hexagonal parameters in the Cr-doped compound (x=0.011). This measurement was done using powder diffraction at the SOLEIL synchrotron (beamline CRISTAL). In the temperature range 240 K down to 190 K a coexistence of the two phase (PI-PM) is observed, in a very similar manner compared to the work of Lupi et al. performed by varying the hydrostatic pressure [46] (we will discuss in detail this phenomena in chapter 6. Changing the temperature from 270 K down to 190 K we undergo the transition between two isostructural PI-PM phases. This transition is accompanied by a discontinuity of the crystalline parameters from (a= 4.9959 Å; c= 13.928 Å) to (a= 4.9456 Å; c= 14.005 Å), reflecting a volume contraction of the unit cell of about 1.46 %. This effect is a common feature of the Mott transition, since the d-electrons that participate in the cohesion of the solid in the metallic phase lead to a smaller lattice spacing than in the insulating phase, where they are localized.

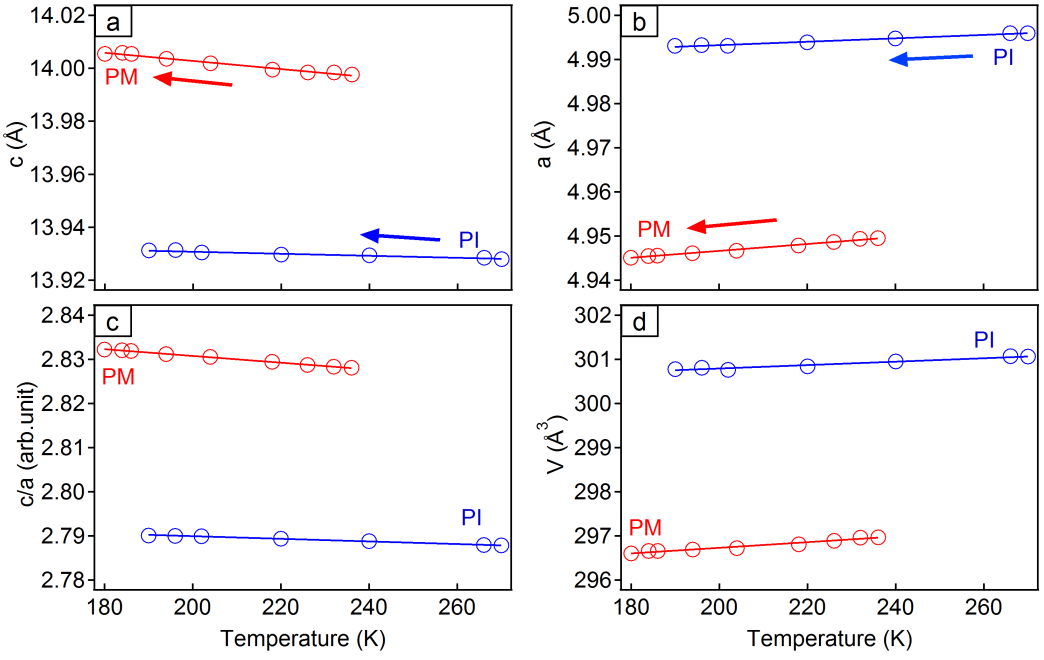

FIGURE 3.6: *Evolution of the crystal parameters in the hexagonal system of the compound $(V_{0.9899}Cr_{0.011})_2O_3$; a), b), c) and d) corresponds to the evolution of the parameters a, c, the ratio c/a and the Volume of the unit cell, respectively. The red color corresponds to the PM phase and the blue color corresponds to the PI phase.*

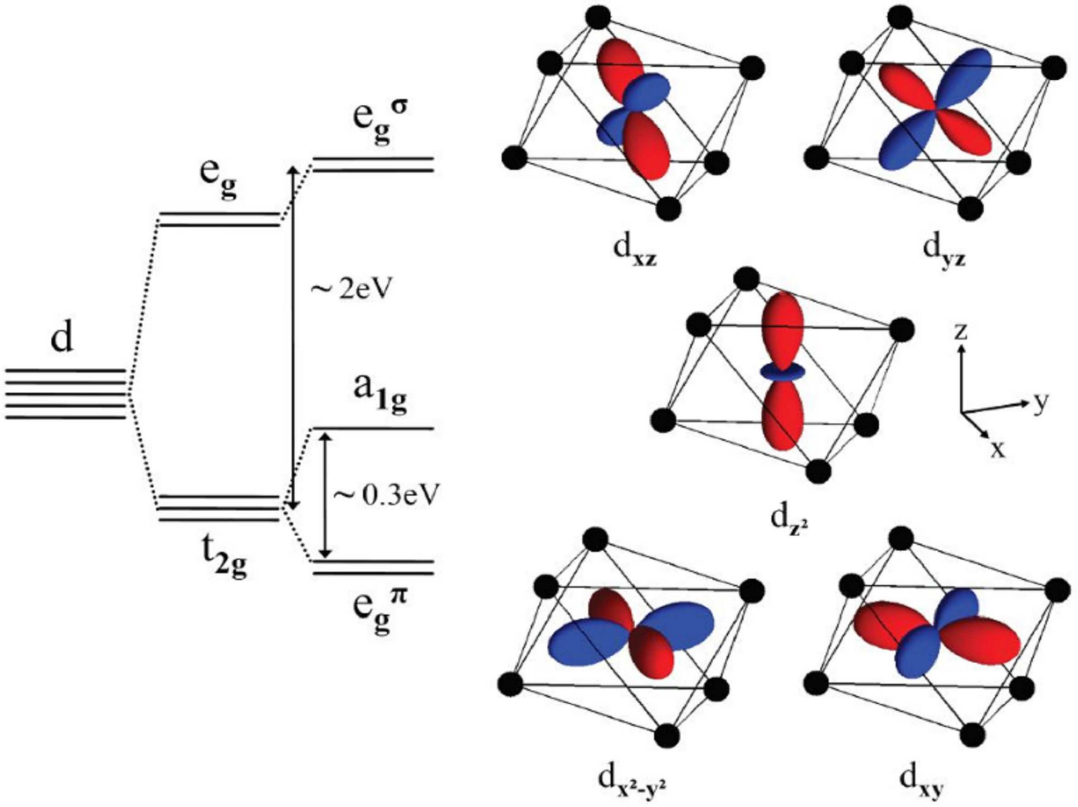

FIGURE 3.7: *The effect of the crystal-field splitting on the d bands.*

3.2.1.3 Electronic structure

In the compound V_2O_3 the vanadium is in its V^{3+} oxidation state, leading to a nominal $3d^2$ configuration. Due to its octahedral oxygen surrounding, the vanadium 3d splits into higher lying $e^\sigma{}_g$ orbitals and lower lying t_{2g} orbitals. The trigonal distortion of the octahedron (VO_6), leads to a degeneracy lifting of the t_{2g} band into a non-degenerate a_{1g} and a doubly degenerate $e^\pi{}_g$ band, as shown in figure 3.7. The orbital a_{1g} is oriented along the c-axis, while the orbitals $e^\pi{}_g$ are oriented predominantly in the hexagonal plane.

3.2.1.4 Spin configuration

What are the positions in energy as well as the occupations of the respective $e^\pi{}_g$ and a_{1g} orbitals in the corundum phase? Castellani et al [47–49], propose a description where pairs of vanadium atoms along the c-axis can form a covalent bond. This results into a strongly bonding/antibonding splitting of the orbital a_{1g}; figure

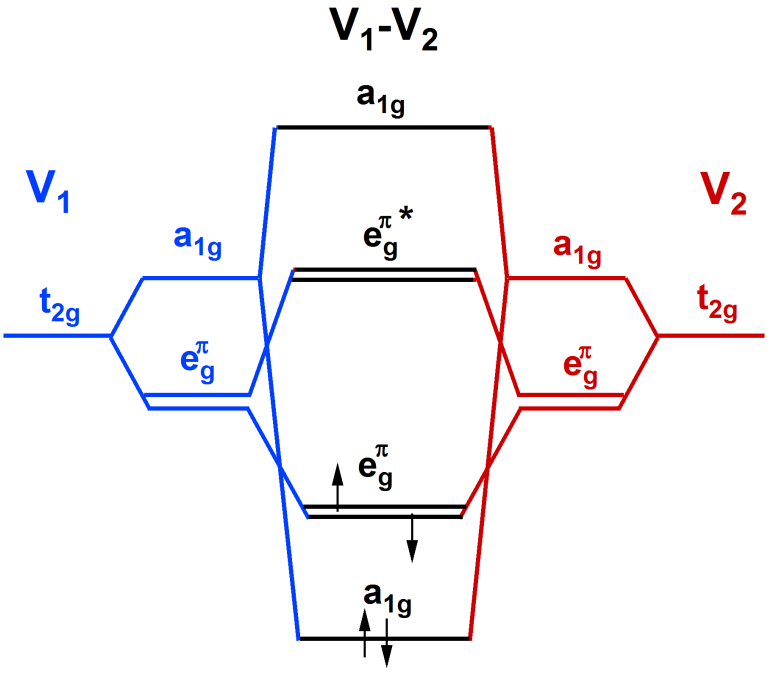

FIGURE 3.8: *The energetic diagram of the atomic states t_{2g} after the occurrence of vanadium pairs V_1-V_2 along the c axis, from* [47].

3.8. As a consequence, the two electrons from the vanadium pairs fill the bonding a_{1g} and the remaining two electrons partially populate the $e^{\pi}{}_g$, giving one electron (S=1/2 spin) per each atom. This suggests that the half-filled one-band Hubbard model is the simplest possible electronic model describing V_2O_3. However, the situation changed when polarization-dependent x-ray absorption measurements by Park et al [50] indicated that the spin is actually S=1 in all V_2O_3 phases. This triggered refinements of the theoretical models. In particular, the LDA+U calculations by Ezhov et al [51] were the first ones to describe correctly the insulating nature of the low temperature, antiferromagnetic monoclinic phase, that proved also to be consistent rather with a S=1 picture of the ground state ; $e^{\pi}{}_g{}^{\uparrow\uparrow}$ and an empty a_{1g}.

3.2.2 Photoemission spectroscopy (PES)

As above discussed, the density of states (DOS) of a Mott-Hubbard system near the Fermi energy can be described with three main features: the quasiparticle peak (QP), the lower Hubbard band (LHB) and the upper Hubbard band (UHB). These

features can be explored experimentally by different spectroscopy techniques. In X-ray absorption spectroscopy (XAS), near the absorption edge, an electron absorbs the incoming photons and it excites above the Fermi level (electron-type excitation). This provides the measurement of the unoccupied states for the QP and the UHB. In photoemission spectroscopy like ARPES (angle resolved photoemission spectroscopy), XPS (soft x-ray photoemission spectroscopy) and HAXPES (hard X-ray phtoemission spectroscopy), one extracts the electrons from states below the Fermi level (hole-type excitation), which allows to measure the occupied states - both the QP and the LHB. In this thesis all the presented experimental results on V_2O_3 are based on photoemission spectroscopy. In this technique the spectral function is directly related to the photoemission intensity as follows:

$$I(k, w) = I_0 A(k, w) f(w) \tag{3.3}$$

where *A(k,w)* is the spectral function corresponding to the extraction of one electron from the system, and *f(w)* is the Fermi Dirac distribution.

By probing the states near the Fermi level (the 3d vanadium states in the case of V_2O_3), it is possible to probe the QP and the LHB band. However, due to the variation of the mean free path of the electron inside the solid depending on its kinetic energy, photoemission spectroscopy (PES) can be a surface sensitive technique at the low energy (20 - 100 eV), used in general for ARPES experiment, which corresponds to a low value of the mean free path. But it can be more bulk-sensitive at high energy using for example XPS (300 - 1000 eV) or HAXPES ($>$ 1KeV), which corresponds to a high value of the mean free path. In addition, to increase the bulk sensitivity one should collect the photoelectrons in normal emission.

Surface sensitivity is actually a drawback to detect the genuine bulk electronic structure of 3D systems. These effects are particularly important in 3D strongly correlated systems in which the electronic properties depend on a very subtle relationship between different energy scales, such as the kinetic energy and the

Coulomb repulsion in the vicinity of the Mott-Hubbard transition. The bandwidth is proportional to the coordination number of the atoms; this is lower at the surface, which increases the correlations effect. The surface can thus exhibit a behavior which is different from the bulk: it can be metallic while the bulk is insulating [52].

In the case of the correlated system V_2O_3, there are many experimental results that demonstrate the effect of the surface on electronic correlations. This is typically obtained by analyzing the QP peak when the photon energy or the emission angle are varied in a photoemission experiment.

3.2.2.1 Soft X-ray and Hard X-ray PES

Figure 3.9-a shows the photoemission measurement done by Mo et al [53, 54] for different Soft X-ray photon energies and at normal emission: only the increased bulk sensitivity by using high photon energy made it possible to detect the QP in the PM phase. At 700 eV, a pronounced QP is detected and presents the first observation of the QP peak in V_2O_3 which is consistent with previous LDA+DMFT calculation [55, 56]. Recently Fujiyara et al. using HAXPES at 8 KeV photon energy were able to measure a more pronounced QP peak than that of Mo et al. (figure 3.9-b) thus showing that correlations are rather depth depended [57].

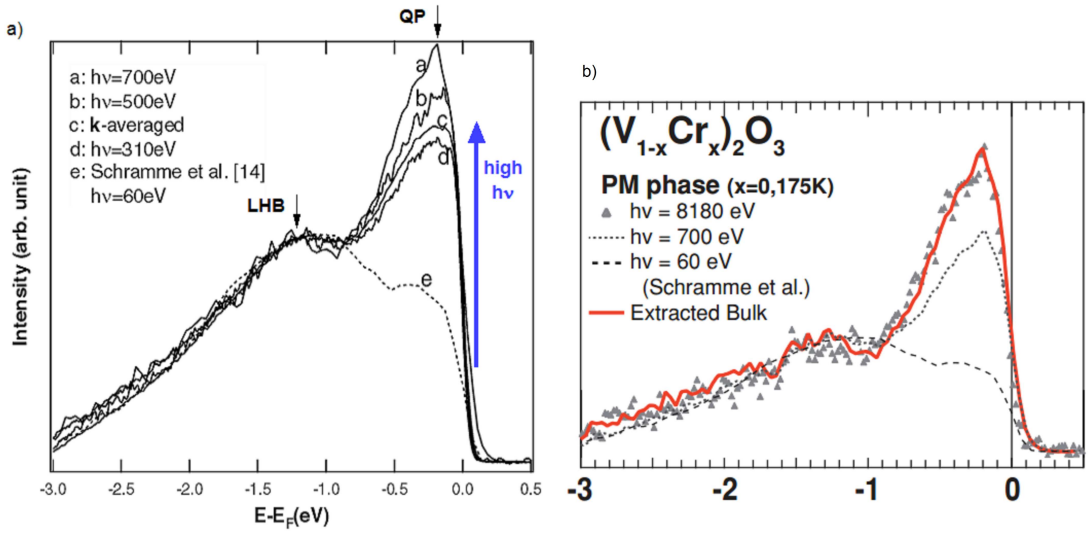

FIGURE 3.9: *a) Soft-XPS measurement in V_2O_3 from [53]. b) HAXPES measurements in V_2O_3 from [57].*

3.2.2.2 ARPES measurements

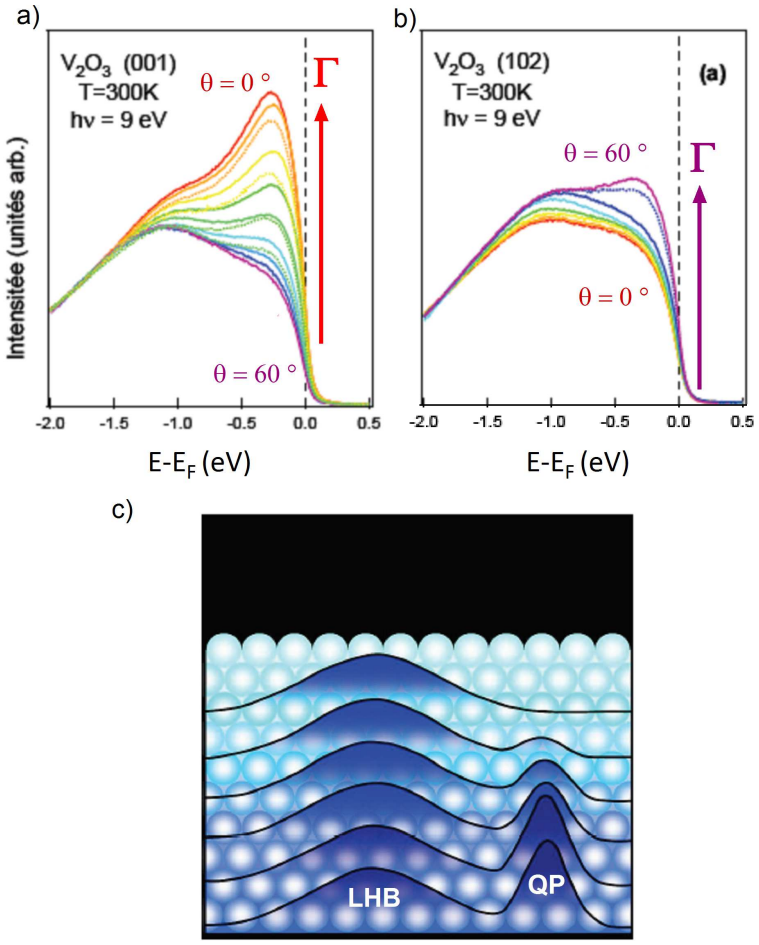

FIGURE 3.10: *a) ARPES measurement in [001] crystal orientation of $V_{22}O_3$; different colors represent the dispersion from the boundary (violet) to the center* Γ *(red) of the Brillouin Zone. b) presents the inverted case for the [102] crystal orientation, from [58]. c) "Insulating behavior is only skin deep" from [59]*

In contrast to high photon energy, low photon energy can provide information of electron's k-dependence, whereas techniques such as XPS or HAXPES can provide mostly k-integrated spectra. At very low photon energy (9 eV), which accounts for a higher value of electron's mean free path, Rodolakis et al [58] using ARPES, were able to k-resolve the QP within the Brillouin zone (BZ). Using a first crystal orientation (001), they found that the QP is more intense only around the center of the BZ (Γ) and with normal emission (figure 3.10-a), consistent with recent LDA + DMFT calculation with k-space resolution [56]. But using another crystal orientation (102) they found that the QP is less intense with grazing emission and

also around Γ (figure 3.10-b), while the incoherent part (the LHB) remains almost constant and k-independent. This proves that the coherent part of the spectral function reacts to the presence of the surface differently from the incoherent part (figure 3.10-c). This notion is consistent with a recent theoretical model proposed by Borghi et al [60], suggesting the presence of a so called *dead layer*. This parameter defines the distance over which the coherent states are disturbed by the presence of the surface beyond the surface itself and it depends on the bulk proprieties of the correlated systems.

Despite this surface attenuation, photoemission spectroscopy provides a direct measurement of the QP and the LHB, which allows to directly detect, at fixed photon energy and emission angle and by varying the temperature or pressure, the PM-PI transition as the transfer of the spectral weight from the QP to the LHB (see chapter 6). This type of spectroscopy further permits to compare the electronic correlation strength in the PM phase by analyzing the QP near the Fermi level.

Reducing this problem of surface sensitivity by using scanning photoelectron microscopy (SPEM) at relatively high photon energy, in chapter 6 we investigate the coexistence of PM and PI domains on the surface, something that is practically impossible by means of standard photoemission spectroscopy (ARPES, XPS...)

Chapter 4

Experimental methods: time and space resolution in photoelectron spectroscopy

4.1 Introduction

The photoelectric effect was initially discovered by Hertz in 1887 [61], and later explained by Einstein [62]. Let us consider photons with energy hν incident on a solid: if the frequency ν is high enough an electron can absorb this energy and escape from the solid with a kinetic energy: E_{kin}= hν - ϕ. ϕ is the work function of the material, and represents the minimun energy required to extract an electron from the solid surface, typically on the order of 5 eV. Such an electron is called a photoelectron. Based on this effect, several spectroscopy techniques have been developed to provide information on the chemical, electronic, dynamic and microscopic properties of solids: by measuring the photoelectron's kinetic energy, X-Ray Photoelectron spectroscopy (XPS) [63] is used to study the chemical properties. If one measures also the photoelectron's emission angles, Angle Resovled Photoelectron Spectroscopy (ARPES) makes it possible to study in detail the structure of valence electronic states, in particular the dispersion of the bands in reciprocal space E(k) [64, 65]. When ARPES is performed using two photon laser pulses in pump-probe configuration, Time-Resolved ARPES (TR-ARPES) represents a

unique technique to study the ultrafast electronic dynamics of solids with k-space resolution [66–69]. Finally, by using light focusing techniques, it is possible to achieve a submicron spatial resolution with techniques like Scanning Photoelectron Microscopy (SPEM), which is particularly useful to study the microscopic details of non homogeneous samples [70, 71].

In this thesis, I will present experimental results obtained using mainly two techniques. The first one is the TR-ARPES, which was used to study the ultrafast surface carrier dynamics between the metallic surface states and the insulating bulk in topological insulators like Bi_2Te_3; the second one is SPEM, which was used to study the coexistence of metallic and insulating domains at the Mott-Hubbard transition in V_2O_3. In this chapter, I will give a description of the ARPES technique to later introduce the TR-ARPES, which will be explained in more details, providing also an extended view on pump-probe spectroscopies in general. Finally, I will describe the instrumental aspects of SPEM, with particular attention to the methods used to focus photons in the X-ray domain.

4.2 Angle-resolved photoelectron spectroscopy

4.2.1 Basic principles

The geometry of a typical ARPES experiment is drawn in figure 4.1: a photoelectron e is emitted by an incident photon with energy $h\nu$; an electron energy analyzer collects the photoelectrons and measures both their kinetic energy E_{kin} and their momentum $\mathbf{K}$ by detecting the two emission angles, polar (θ) and azimutal (φ). From these values one can obtain information respectively on the binding energy E_B and the momentum $\mathbf{k}$ of the electrons inside the solid:

The kinetic energy: the energy balance of the photoemission process from the solid to the analyzer is represented in figure 4.2-a, where the Fermi level E_F is taken as a null reference: on the left, the energy level diagram of the electrons inside the solid; on the right, the drawing of the associated photoemission spectrum measured by the analyzer. ϕ is the work function between the Fermi level and the

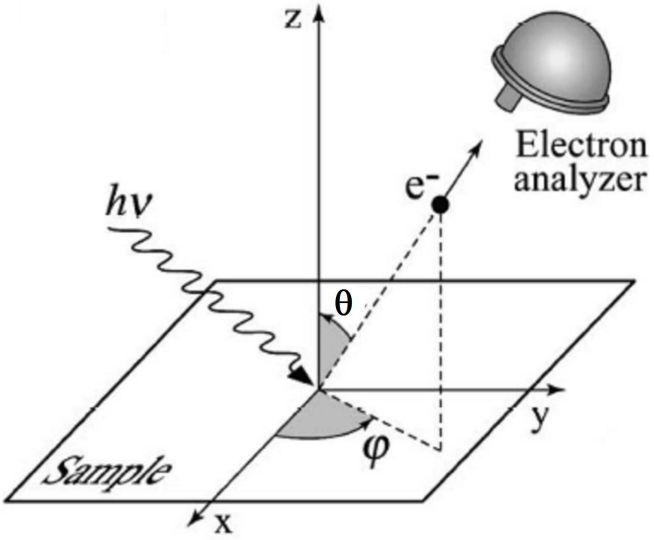

FIGURE 4.1: *Experiment geometry of the ARPES technique, from [64].*

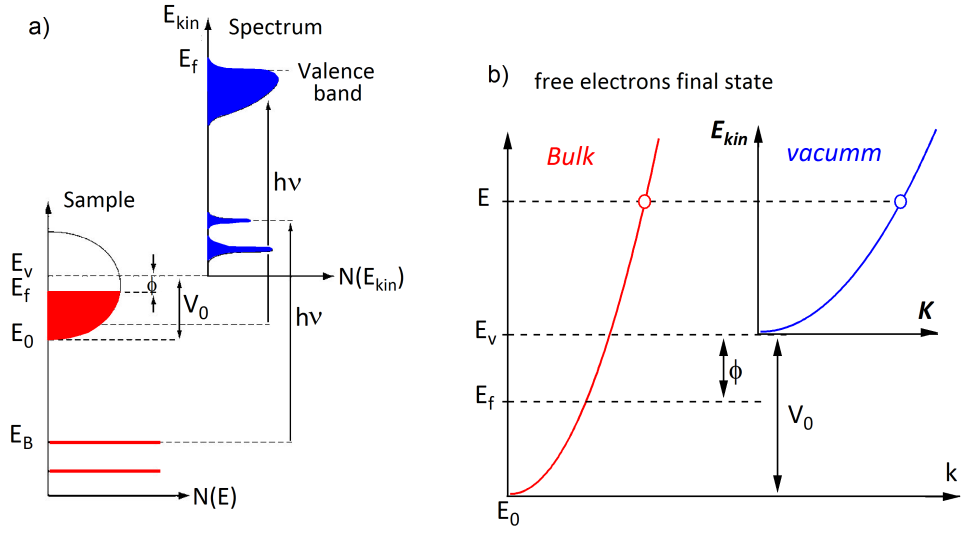

FIGURE 4.2: *a) the energy balance of the photoemission process, from [64]. b) nearly free-electron description for the final bulk states*

vacuum level E_V, and E_B represents the binding energy. By measuring E_{kin} with the analyzer, one can determine E_B by means of the simple energy conservation relation:

$$E_{kin} = h\nu - E_B - \phi \tag{4.1}$$

The momentum k: at low photon energies, typically $h\nu < 100$ eV, photon momenta can be neglected if one considers the typical size of the Brillouin zone

(typically of the order of 10^8 cm^{-1}). Thus one can take into account only electron momenta when employing conservation laws. The wave vector of the photoelectron in vacuum **K**= P/2m can be completely determined: its module is given by **K**= $\sqrt{2mE_{kin}}/\hbar$ and its components parallel ($\mathbf{K}_{//} = \mathbf{K}_z + \mathbf{K}_x$) and perpendicular (**K**⊥= $\mathbf{K}_y$) to a sample surface are obtained from the two emission angles θ and φ as:

$$K_x = \frac{2\pi}{\hbar}\sqrt{2mE_{kin}}\cos(\varphi)\sin(\theta) \tag{4.2}$$

$$K_y = \frac{2\pi}{\hbar}\sqrt{2mE_{kin}}\sin(\varphi)\sin(\theta) \tag{4.3}$$

$$K_z = \frac{2\pi}{\hbar}\sqrt{2mE_{kin}}\cos(\theta) \tag{4.4}$$

The translational symmetry on the surface is not conserved in the bulk due the sudden change of potential along the z axis. The wave vectors conserved in the photoemission process are only the vectors parallel to the surface. i.e $\mathbf{K}_{//}$=$\mathbf{k}_{//}$ and so:

$$k_{//} = \frac{2\pi}{\hbar}\sqrt{2mE_{kin}}\sin(\theta) \tag{4.5}$$

Leading to determine the momentum parallel resolution as:

$$\Delta k_{//} = \frac{2\pi}{\hbar}\sqrt{2mE_{kin}}\cos(\theta)\Delta\theta \tag{4.6}$$

However, the perpendicular component **k**⊥ can be determined if an a priory assumption is made for the dispersion of the electron final states E_f (**k**) participating in the photoemission process and for the inner potential inside the solid. In particular we can either use the results of band structure calculations, or adopt a nearly free-electron description for the final bulk states i.e. a parabolic dispersion as shown in figure 4.2-b. Therefore we can write that:

$$E_f(k) = \frac{\hbar k^2}{2m} - |E_0| = E_{kin}\sin^2(\theta) + \frac{\hbar k_\perp^2}{2m} - |E_0|. \tag{4.7}$$

with E_0 is the energy of the bottom of the valence band.

Since E_f (**k**)= E_{kin} + ϕ, the perpendicular component of the electron inside the solid **k**$\perp$ can be written as

$$k_\perp = \frac{1}{\hbar}\sqrt{2m(E_{kin} + V_0)\cos^2(\theta)} \tag{4.8}$$

with V_0= $|E_0|$ + ϕ is defined as the inner potential.

Fortunately there are special classes of materials for which the uncertainty in **k**$\perp$ is less relevant. It is true in particular for low-dimensional systems where the band dispersion along the z-axis is negligible, and it is exclusively determined by $\mathbf{k}_{//}$ [65]. This is the case for example of our topological insulator Bi_2Te_3, thought of as a bi-dimensional system.

ARPES is indeed a powerful technique to measure the band dispersion E(k) in 2D systems, by extracting E_B and $k_{//}$ from the previous formulas. ARPES is actually the main experimental technique in solid state physics to measure E(k).

4.2.2 Hemispherical analyzer

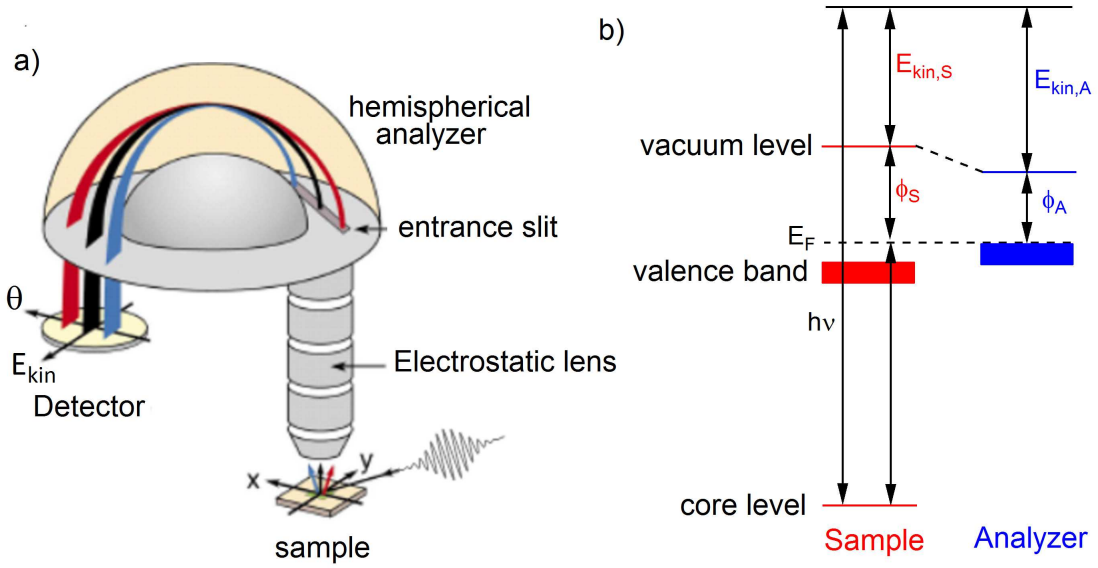

FIGURE 4.3: *a) General schematic view of a hemispherical electron analyzer. b) Energy relation between the sample and the analyzer*

One of the essential components of an ARPES experiment is the hemispherical electron energy analyzer, which provides the measurement of the kinetic energy

and the emission angle of the ejected electron. In figure 4.3- a general schematic view of a hemispherical energy analyzer is provided. An electro-optical lens is placed in front of the analyzer entrance slit. This will focus parallel electron beams into different parts of the entrance slit situated in the focal plane of the lens. When electrons enter the analyzer through the entrance slit, they will be detected only if they have the appropriate kinetic energy, i.e. if they can pass through the hemispheres without collisions with the inner walls. More in detail, let us consider an electron travelling inside an analyzer made by two concentric hemispheres of radii R1 and R2. These are kept at a potential difference ΔV, so that only the electrons that reach the entrance aperture with the appropriate kinetic energy E_p will pass through the hemispheres. E_p is called the pass energy of the analyser and given by:

$$E_p = \frac{e\Delta V}{\frac{R_1}{R_2} - \frac{R_2}{R_1}} \tag{4.9}$$

To make a scan of various energies,a retarding voltage is applied at the entrance lens in order to slow down electrons to the pass energy. The energy resolution of the hemispherical analyzer is given by:

$$\Delta E = E_p(\frac{w}{R_0} + \frac{\alpha^2}{4}) \tag{4.10}$$

where R_0=$(R_1 + R_2)/2$, w is the is the width of the entrance slit, and α is the acceptance angle. After passing through the electric field between the two hemispheres, the electrons will be separated according to their emission angle and their kinetic energy at the same time forming a two dimensional image on the detector. What is actually measured is the kinetic energy of the electron inside the analyzer $E_{kin,A}$, where the analyzer work function is present ϕ_A. Figure 4.3-b, shows the energy level diagram for photoemitted electrons including the effect of the analyzer. Thus in order to extract the binding energy E_B one has to take into account the analyzer's work function (an offset-value that can be experimentally measured). By having the sample in electrical contact with the analyzer, the Fermi levels E_F of both the sample and the analyzer are lined up. By taking a reference spectrum from the Fermi level region, hν - $E_{kin,A}$ at the Fermi level gives the work function of the analyzer ϕ_A and thus the value of E_B is determined.

4.2.3 Photoemission intensity

The Three-Step Model [72] is one of the earliest models used to describe the photoemission process. The underlying physical idea is that the photoemission yield is the result of the product of three independent contributions which do not interfere one with each other:

-Optical excitation of the electron from an initial state $|\Psi_i\rangle$ to a final excited state $|\Psi_f\rangle$ in the bulk.

-Propagation of the excited electron to the surface

-Escape of the photoelectron into the vacuum after transmission through the surface potential.

Optical excitation :

To describe the optical excitation one must compute the transition probability $W_{i,f}$ from the N-electron ground state $|\Psi_i\rangle$ to the final state $|\Psi_f\rangle$ with (N-1)-electrons plus the electron excited inside the solid. This can be approximated by using Fermi's Golden Rule, as a result of perturbation theory to the first order:

$$W_{i,f} = \frac{2\pi}{\hbar}|\langle\Psi_f|H_{int}|\Psi_i\rangle|^2\delta(E_f - E_i - h\nu) \tag{4.11}$$

where E_i and E_f are respectively the energy of the initial and the final excited state.

$$H_{int} = -\frac{e}{mc}\vec{A}.\vec{P} \tag{4.12}$$

is the Hamiltonian describing the photon-electron interaction

By the assumption of an independent-particle picture applied to the initial system, the wave function can be written as the product of one and (N-1)-electron's wave function. Using a second approximation applied to the final state, where the photoemission process is assumed to be sudden with no interaction between the system left behind and the photoelectron, and no relaxation during the photoemission process itself, the wave function of the final states can be given by the product of two wave functions describing respectively the photoelectron and the (N-1)-electrons of the system left behind.

If we sum over all possible transitions $W_{i,f}$ we obtain the total photoemission intensity:

$$I(E_{kin}, \mathbf{k}) = \frac{2\pi}{\hbar} \sum_{i,f} |M^k_{i,f}|^2 \sum_m |c_{m,i}|^2 \delta(E_{kin} + E_m - E_i - h\nu) \quad (4.13)$$

where $M^k{}_{i,f}$ is the one-electron dipole matrix element, E_m is one of the possible final excited states, and $c_{m,i}$ describes the overlap between the initial (N-1) states and one of the possible **m** excited final states with (N-1) electrons. This intensity must take into account the cross section, which depends on the photon energy and polarization, as well as on the experimental geometry.

Propagation of the electron towards the surface :

The propagation of the excited electron towards the surface is described in terms of an electron mean free path λ, which describes the probability of the excited electron to arrive at the surface of the sample without undergoing any inelastic scattering and so without suffering any change in its kinetic energy or momentum. The inelastic scattering, due to electron-electron and electron-phonon interactions, causes the electrons to have a kinetic energy which is lower than that expected from their initial value E_i, and this gives an inelastic background which is present in photoemission experiments and generally decreases with E_{kin}. The inelastic scattering is the major factor limiting the electron mean free path at a depth z inside the sample, as a consequence the photoemission yield, I (z), decreases exponentially with depth according to the equation:

$$I(z) \propto I_0 e^{-z/\lambda \cos\theta} \quad (4.14)$$

The curve for an electron mean free path [73], figure 4.4, has a universal trend because many analysis of experimental data for the inelastic mean free paths in different materials proved that their values follow more or less the same behavior, with a minimum at about (5-20 Å) in the kinetic energies region of (20-100 eV). This rather small electron escape depth implies that the majority of the photoemission intensity is representing only the topmost surface layers, and this is the

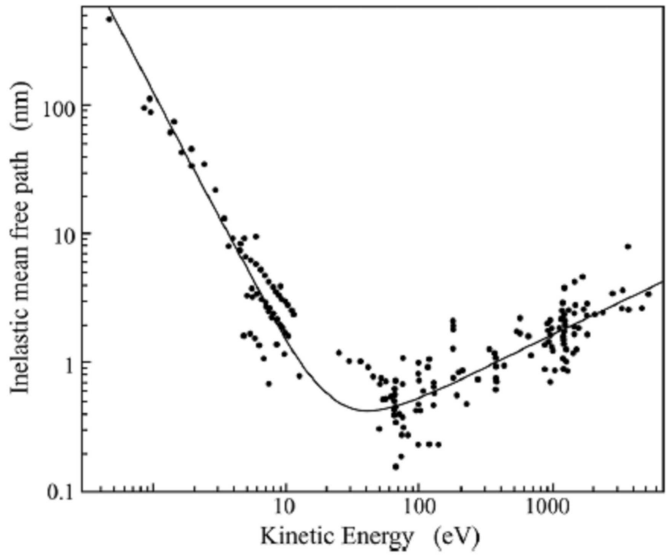

FIGURE 4.4: *The "universal" mean free path for electrons inside solids depending on thier kinetic energy, from [73]*

reason why photoemission is considered as a *surface sensitive* technique. Under these considerations, it is of great necessity to keep the surfaces under study extremely clean and without defects at the atomic scale; the quality of the surface determines the quality of the spectra. The experiment must be realized on freshly cleaved surfaces and in situ ultrahigh vacuum condition ($< 10^{-9}$ mbar), to maintain the surfaces still clean; it's possible in some case to create a layer of adsorbates in few minutes after cleaving the sample. On the other hand, for 3D systems, it is possible to decrease the surface sensitivity by choosing incident photons either at low energy < 10 eV or at high energy > 1 KeV: at low energy the angular resolution is better, but we probe a small energy range below the Fermi level. While at high energy, we loose angular resolution, but we preserve a good penetration in the bulk (k$\perp$ becomes higher).

Escape of the photoelectron from the surface into vacuum :

The escaping electrons are those for which the component of the kinetic energy normal to the surface is sufficient to overcome the surface potential barrier; the other electrons are totally reflected back into the bulk. Inside the bulk as shown in figure 4.2-b, the electrons travel in potential of depth $V_0 = E_0 + \phi$. To escape

into the vacuum the electrons must satisfied the condition:

$$\frac{\hbar k_{\perp}^2}{2m} > V_0. \tag{4.15}$$

4.3 Time-resolved ARPES

4.3.1 Basic principles

Using pump probe spectroscopy with laser pulse durations up to few femtoseconds (1 fs = 10^{-15} s), opened the possibility of measuring ultrafast dynamics of various samples on this time scale. Its combination with the ARPES measurement allows probing the electronic structure dynamics with k-space resolution. This combination leads to so called time resolved ARPES (TR-ARPES) illustrated in figure 4.5.

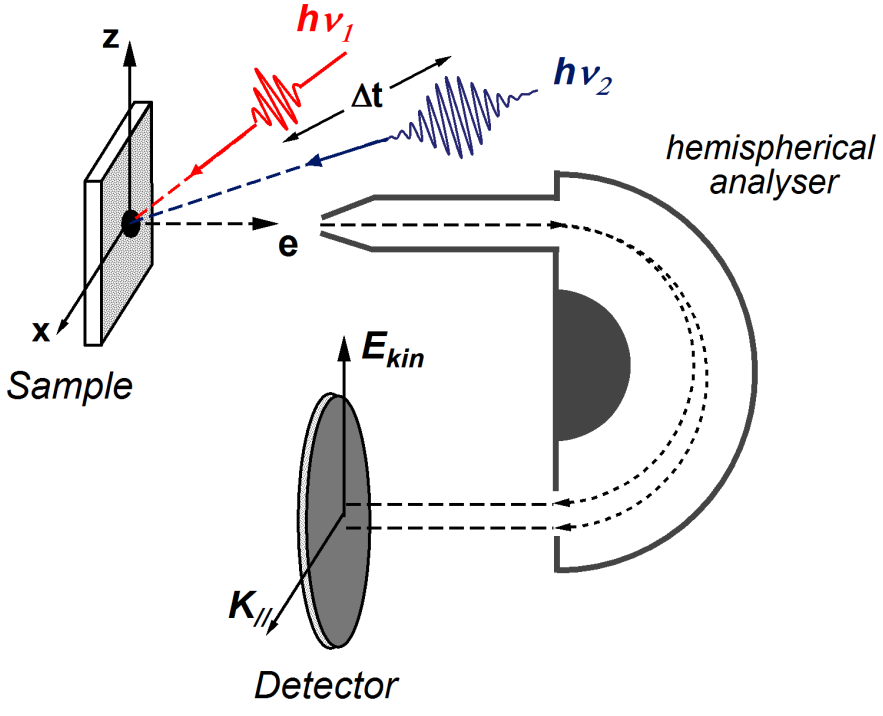

FIGURE 4.5: *Experimental geometry of the pump-probe ARPES configuration: $h\nu_1$ is the pump excitation and $h\nu_2$ is the probe photon*

As previousely described in conventional ARPES studies, electrons may escape the solid surface by irradiating them with monochromatic light sources such as

discharge lamp (He-Lamp) or synchrotron radiation. Now if instead of (quasi-) continuum sources, two femtosecond laser pulses are used in a pump-probe configuration, one can have a direct way to visualize the relaxation of the photoexcited electronic band structure. The different components of TR-ARPES can be seen in figure 4.5: the first one is a femtosecond pump pulse ($h\nu_1$) which creates an out of equilibrium excited state in the sample, and the second one is the femtosecond probe pulse ($h\nu_2$) used to eject the electrons from the surface into the analyzer, where, like in ARPES experiment, the electron kinetic energy and its momentum are both measured. By the interband and the intraband excitation processes, the pump pulse can create different excited states on the system, from the occupied to the unoccupied states, while the probe pulse is used to detect these different excited states, i.e. taking an excited ARPES image describing the occupied and the unoccupied excited states. By gradually delaying the arrival time of the probe pulse with respect to the pump pulse, represented by the Δt in figure 4.5, the relaxation process can be followed in time: from short time scales, about tenth of fs, to longer time scales of more than a few hundreds of ps. Different types of relaxations processes (electron-electron, electron-phonon scattering...) have different characteristic decay times, and allow the system to return to its initial equilibrium state.

TR-ARPES provides then the evolution as a function of pump-probe time delay Δt of different excited ARPES images, describing the system from its initial excitation and through its relaxation. It is a unique experimental technique in terms of providing a measure of the out of equilibrum states with a k-space resolution. There are nowadays several TR-ARPES experimental setups in the world, differing by some technical aspects like the laser source of the electron analyzer: some examples are the setups of Martin Wolf et al. (Berlin, Germany) [69], of Alessandra Lanzara et al (Berkeley, USA) [66], of Murnane and Kapteyn (Boulder, USA) [67], of Durakiewicz and Rodriguez (Los Alamos, USA) [68], of Nuh Gedik (Boston, USA), of Fulvio Parmigiani (Trieste, Italy), and of Z.X. Shen (Stanford, USA) etc. The TR-ARPES setup used for the experiments presented in this thesis is FemtoARPES, and is located in Paris (France), and is a collaboration among the groups of the LSI (Luca Perfetti), of SOLEIL (A. Taleb) and of

LPS (M. Marsi). In the following I will provide a more detailed description of this setup, as well as a general introduction to pump-probe spectroscopies.

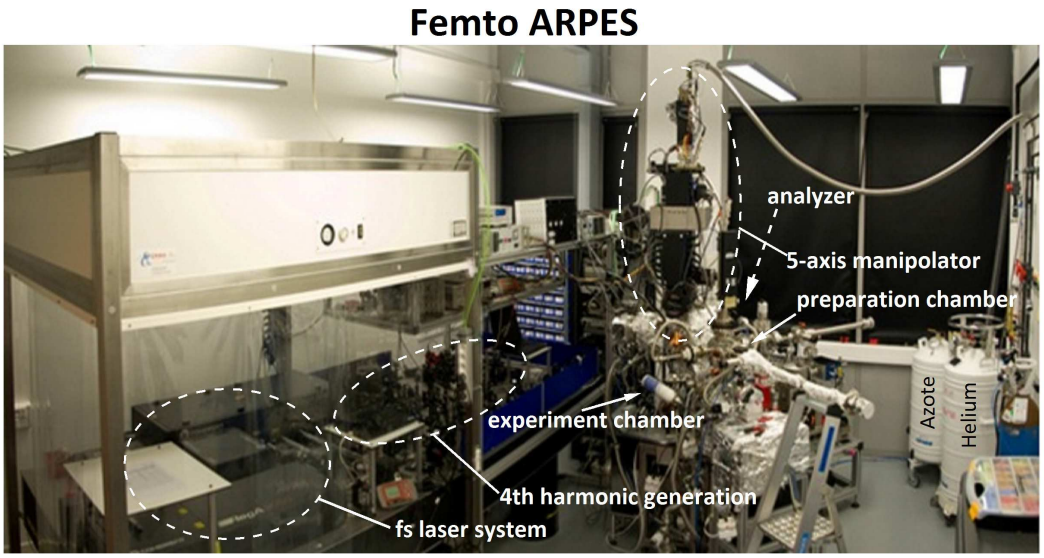

FIGURE 4.6: *FemtoARPES experiment room*

4.3.2 The FemtoARPES setup

4.3.2.1 ARPES configuration

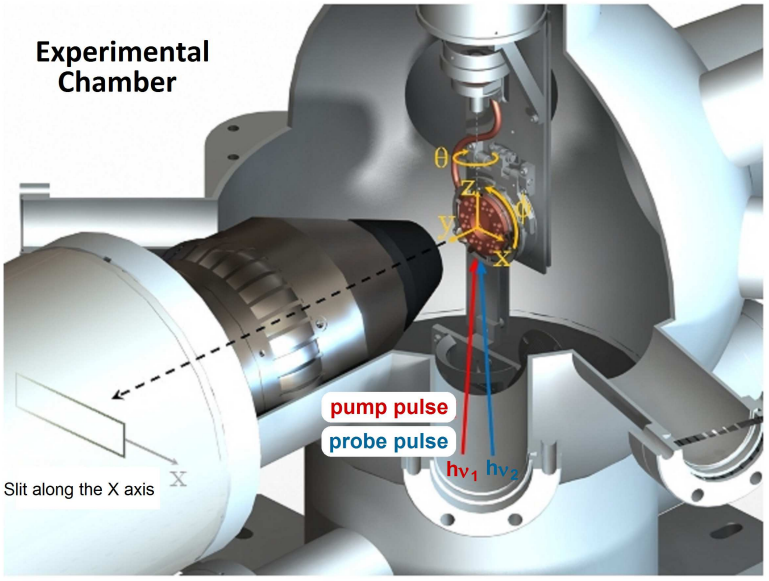

FIGURE 4.7: *ARPES configuration of the FemtoARPES experiment*

The experimental geometry of the ARPES configuration is shown in figure 4.7: The emission angles and the sample's position are guided by a 5-axis manipulator motor (X-Y-Z-θ-ϕ), possessing the capabilities to heat up (600 K) and cool down (40 K) the samples. The experiments are realised under ultrahigh vacuum conditions (10^{-10} mbar). The sample is irradiated by two pulsed laser beams in pump-probe configuration and placed in front of a hemispherical electron analyzer (SPECS Phoibos 180), with angular resolution $< 0.15°$ and energy resolution < 10 meV. The electrostatic lenses allow to change the angular acceptance (from $\pm$ 3° to $\pm$ 14°) and the wanted kinetic energy range.

4.3.2.2 Pump probe spectroscopy

The Femtosecond laser system [74–76] is shown in figure 4.8-a: we start from the oscillator Ti:Sapphire (Micra) pumped by diode laser (Verdi 523 nm), which gives a wavelength range between 780 nm and 820 nm with a bandwidth of 45 nm at a repetition rate 80 MHz. This wavelength interval corresponds to photon energies between 1.5 eV and 1.59 eV. A phase modulator (SILHOUETTE) is used to measure the temporal profile of the laser pulses. In order to enhance the energy per laser pulse, the output pulses from the oscillator are first stretched to a length of more than 100 ps to prevent damage to the optical elements. A regenerative amplifier (RegA) is then used for amplification. After subsequent compression, lasers pulse of 35 fs with 6 μJ at a repetition rate of 250 kHz are available. Half of this output pulse is split off as a pump pulse to excite the sample. However, the ejection of an electron from the surface must require a laser pulse with photon energy greater to the work function.

For this reason the other half of the output pulse will be used to generate higher photon energies using non-linear optical processes in crystal β-barium borate (β-BBO) [77], see figure 4.8-b: the first harmonic ω_0 can be doubled ($2\omega_0$), tripled ($3\omega_0$) and then quadrupled (fourth harmonic $4\omega_0$). A detail about the generation of this fourth harmonic is well described in the reference [75], where the fourth harmonic, used as probe pulse, is with 6.23 eV photon energy and 50 fs larger pulse, which gives an overall time resolution of 80 fs in the pump probe process.

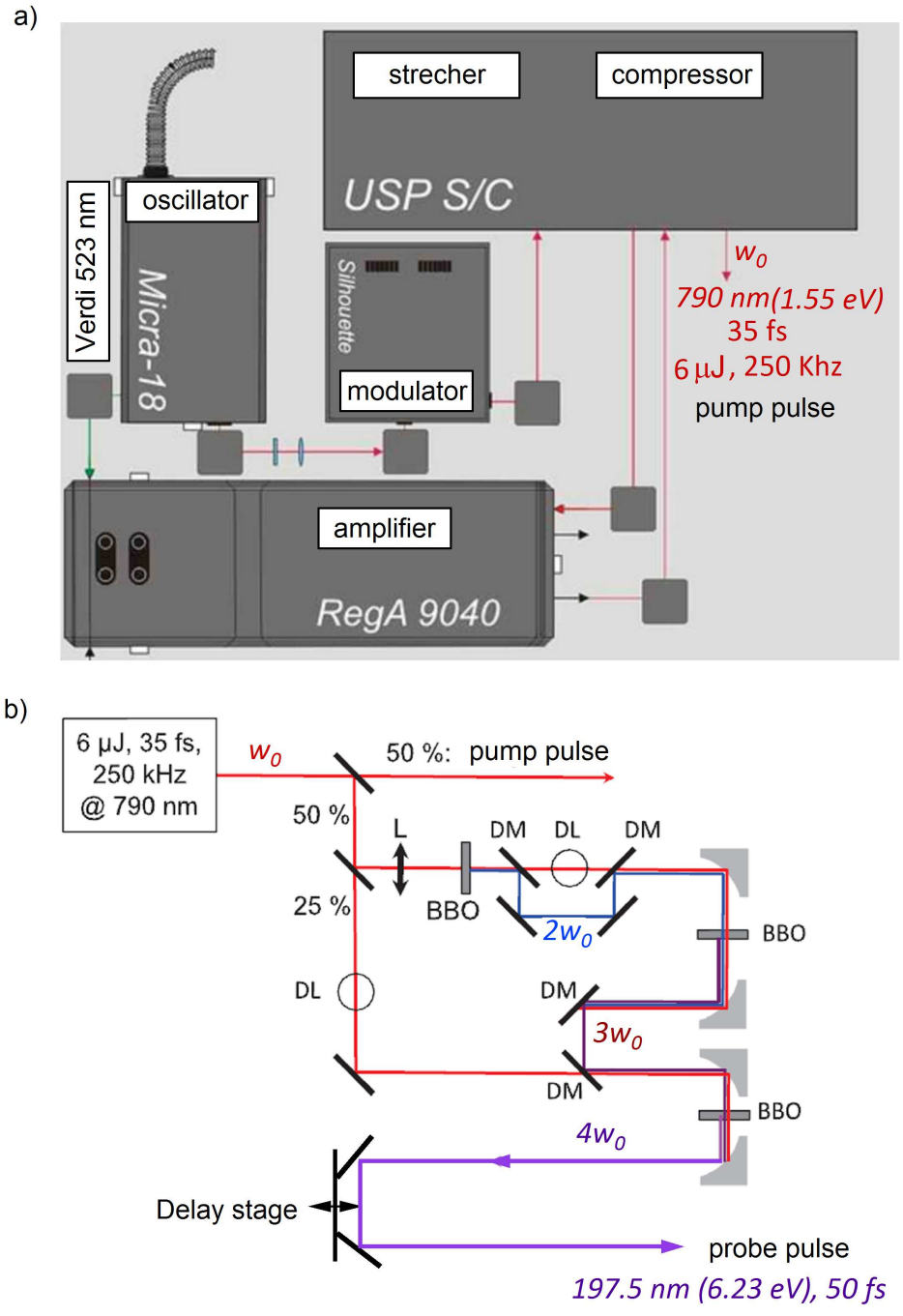

FIGURE 4.8: *The pumpe-probe spectroscopy of the FemtoARPES experiment: a) the Femtosecond laser system, b) the generation of the fourth harmonic using crystal (β-BBO) with the mechanical delay line to shift the delay time between the pump and the probe pulse.*

The last signal from the fourth harmonic used in order to detect as the mechanical delay line. By $\Delta t = \Delta x/c$ (with c the speed of light), the position change of the mechanical delay line is translated into a change of the time delay between pump and probe pulse. The maximal position change of mechanical delay stages is

usually limited to few centimeters. Therefore, the maximal time delay is of the order of tens to hundreds of picoseconds. To probe a 10 ns long process, the delay line has to be scanned over a 1.5 m distance. The realization of time windows on the order of nanoseconds is unpractical with this technique.

4.3.3 Interaction of Pulsed Light with Matter

In order to know the possible electronic processes after the pump excitation on the sample, I will outline in this paragraph the different electronic effects that can be seen in the laser-solid interaction, especially in the case of metals and semiconductors.

4.3.3.1 The excitation processes

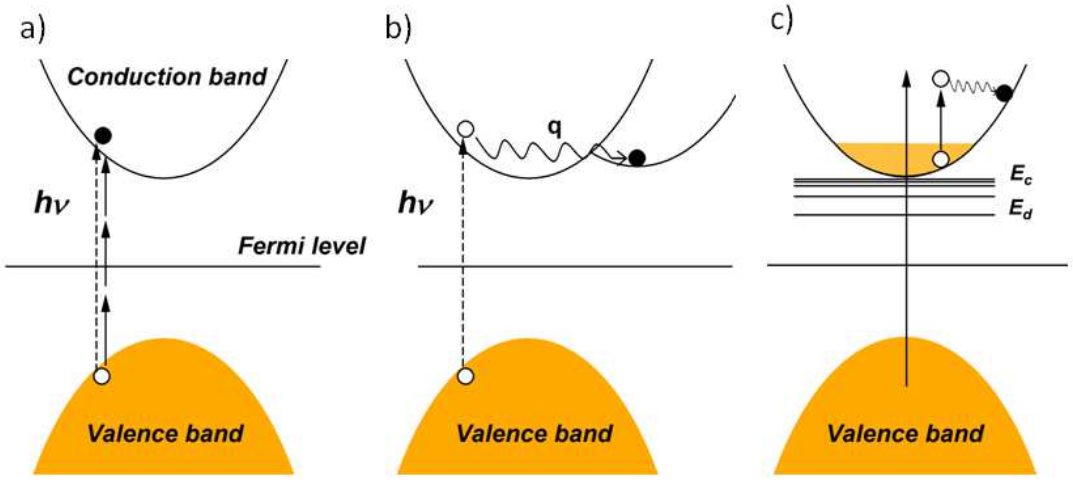

FIGURE 4.9: *a) a direct transition after the pump excitation, b) an indirect-transition: a phonon is involved, c) intraband transition in n-type semiconductor.*

In a semiconductor, a photon with energy comparable to the energy gap can excite an electron from an occupied state in the valence band to an unoccupied state in the conduction band. At high flux also multiphotonic processes can excite the electrons from the conduction band. This is called an **interband excitation** and is represented schematically by the picture in Figure 4.9-a. In this process the

photon is absorbed, an excited electronic state is formed and an empty state hole is left behind. It can be either a direct transition (conserving crystal momentum **k**) or an indirect transition (a phonon is involved, figure 4.9-b: the **k** vectors for the valence and conduction bands differ by the phonon wave vector **q**). Conservation of crystal momentum yields $\mathbf{k}_v = \mathbf{k}_c + \mathbf{q}$. In discussing the direct transitions, optical photons possess very little momentum with respect to the electron. Thus, a typical direct optical interband process excites an electron from a valence to a conduction band without a significant change in the wave vector.

This transition depends on the coupling between the valence and conduction bands and this is measured by the magnitude of the momentum matrix elements coupling the valence and conduction bands states. This dependence results from Fermi's Golden Rule and from the perturbation interaction H_{int} of the electromagnetic field with electrons in the solid, equation 4.11.

However, in semiconductors selected impurities are frequently introduced to make them n-type or p-type. The introduction of impurities into a crystal lattice not only shifts the Fermi level, but also results in a perturbation of the periodic potential, giving rise to bound impurity levels which often occur in the band gap of the semiconductor. Impurities and defects in semiconductors can be classified according to whether they result in a minor or major perturbation to the periodic potential, which corresponds to giving electron carriers (donors) or hole carriers (acceptors). Figure 4.9-c presents the case of a donor states in a n-type semiconductor. In a pump excitation, a transition between different states in the same conduction band occur, known of as the **intraband excitation**.

4.3.3.2 The relaxation processes

After the pump excitation, the excited electrons will interact with other particles leading to relaxation of the energies absorbed to go back to equilibrum. The timescale of the different relaxation processes can change with respect to the interaction types, figure 4.10. In the following I will describe some scattering processes that can be seen in metals and semiconductors:

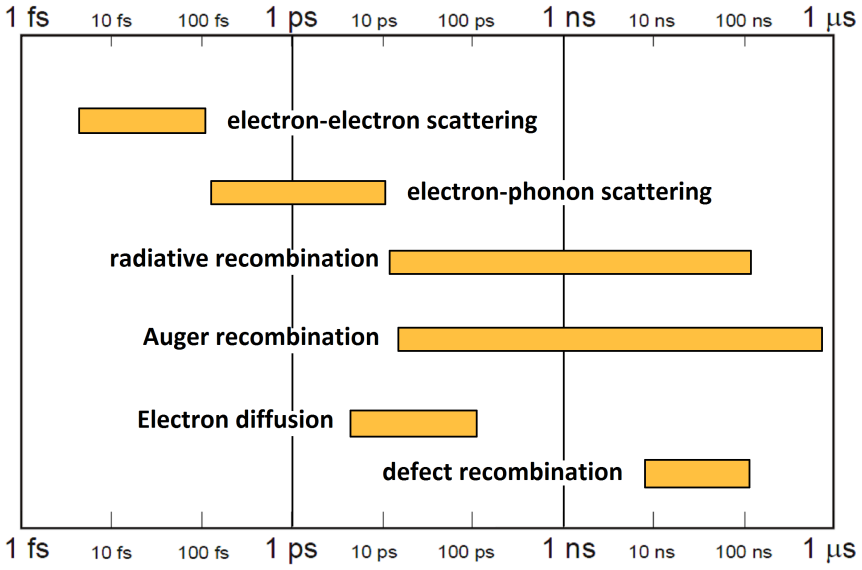

FIGURE 4.10: *Chart of the time response of metals-semiconductors to light excitation [78]*

The electron-electron scattering :

In the case of metals, the electron-electron scattering is treated using the theory of Fermi liquid. Without going into the details of this theory, the possibility for an electron located above the Fermi level to excite another electron, depends of the available phase space of itself and of the excited electron in the final state, which is limited by the Pauli's exclusion principle. At T temperature, an initial electron with energy ϵ_i near the Fermi level ϵ_f has a diffusion rate $1/\tau$ which depends on its energy and on the temperature T as:

$$1/\tau \propto w_p(\epsilon_i\text{-}\epsilon_f)^2 + c(k_B T)^2$$

where w_p is the frequency plasma of electrons gas, and c is independent of ϵ_i and T.

If $(\epsilon_i\text{-}\epsilon_f)$ is about 1 eV, then τ is of the order of 10 fs. After photoexcitation, the electrons thermalize to a Fermi-Dirac distribution through e-e scattering. At this stage ($<$ ps) the electron gas temperature is different from the phonon (lattice) temperature. The following phase ($>$ ps) is characterized by electron-phonon scattering.

The electron-phonon scattering :

Lattice vibrations involve deviations of the ions from their positions of equilibrium and therefore a modification of their interaction with the electrons. A perturbative treatment of this interaction leads to the notion of electron-phonon interaction.

The lattice vibrations are described in terms of 3N branches for the phonon dispersion relations, where N is the number of atoms per primitive unit cell. Three of these branches are the acoustic branches, and the remaining 3N-3 are the optical branches. The characteristic shape of these two branches is shown in figure 4.11: the lower branches are the acoustic branches corresponding to the oscillation of different unit cells, and their dispersion relations are of the form w = cq (for small q), which is characteristic of a sound wave. The upper branches are named optical branches, and correspond to the oscillation of atoms inside a single unit cell. In contrast to the acoustic phonons, the optical phonon's frequency is non-zero at q=0.

The interaction of the electrons with the lattice vibrations can be regarded as a collision between an electron and a phonon, in which the phonon is absorbed (or emitted) 4.11: annihilation (or creation) of an electron in the state k and a phonon with wave vector q, and the creation (or annihilation) of an electron in the state k + q.

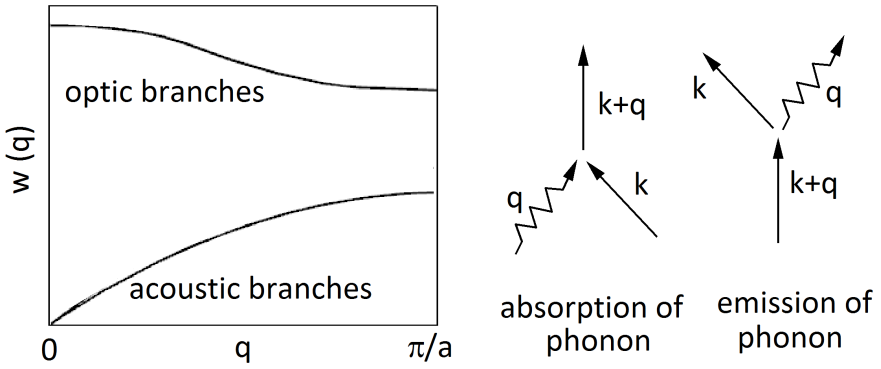

FIGURE 4.11: *At the right the types of phonon branches in the solids, at the left the absorption and the emission of a phonon after the interaction with an electron.*

In this way phonon scattering processes decrease the electron gas temperature and increase the lattice temperature: this interaction can be happen on the time scale of about one to ten picoseconds.

Radiative and non radiative recombination:

The excited electron is in interaction with the hole left behind in the valence band. This interaction can lead to a radiative recombination process: the electron recombines with the hole, emitting a photon in a process perfectly symmetric with respect to the absorption described above.

Another possible (non radiative) process is the Auger recombination, where the excess energy causes the emission of another electron.

Both these recombination processes are slow, typically of the order of nanoseconds, and become important only when other faster relaxation processes are finished.

4.4 Scanning Photoelectron Microscopy

4.4.1 Introduction

Different spectroscopy techniques (XPS, XAS...) make it possible to extract chemical and electronic information from solid samples, but they are not readily applicable to inhomogeneous samples. The spatial information from surfaces can be provided by other techniques, like the SEM (scanning electron microscopy) and STM (scanning tunnel microscopy). These techniques have been developed to provide, with their spatial resolution, also a spectral information: by measuring the differential tunneling conductance, the STM was developed to measure the local density of states (scanning tunneling spectroscopy, STS); the signal is originated from the outermost atomic layer. The combination of (SEM) with Auger electron spectroscopy (AES) leads to the scanning Auger microscopy (SAM), which also provides spectral information by the emission of the Auger electrons; the chemical information provided by the Auger emission is relatively limited compared to the XPS or XAS technique; besides, the electron beam is generally harmful to the surface layer. Other sources like synchrotron radiation X-rays are gentler with solid surfaces, especially in ultra high vacuum condition ($< 10^{-9}$ mbar): using these sources, Photoemission spectroscopy (PES) has been developed to provide, in addition to its spectral information, also a spatial resolution in the micrometer range

or better. This is the case of SPEM (Scanning photoelectron microscopy), where the incoming photon beam can be focused using different optical solutions, making it possible to obtain photoelectron spectra with submicron spatial resolution. Effective focusing can be obtained using spherical mirrors like in the Schwarzschild objectives [79] or the Kirkpatrick-Baez objectives [80], or by diffractive optical elements like the Fresnel zone-plates [70, 71]. The photoemission microscopy results presented in this thesis were obtained using a SPEM with Fresnel zone plates. The microscope is located at the ELETTRA Synchrotron (Italy), on the beamline ESCA-microscopy.

4.4.2 Synchrotron radiation

The term synchrotron radiation indicates electromagnetic radiation that is produced when charged particles (usually electrons, but also positrons, protons, etc) are forced by magnetic fields to move in a closed circular path at a speed close to the speed of light. The most important properties of synchrotron radiation are:

- High brilliance of the photon flux.

- Full control of the polarization of the radiation.

- High energy resolution.

- Wide range of photon energy.

These characteristics make synchrotron radiation highly preferable with respect to conventional laboratory sources. Electrons circulating in storage ring cause the emission of a continuous spectrum of light with different wavelengths and power. Scientists can then select the wavelengths they require for their experiments, ranging from infrared to X-rays. The synchrotron is composed of many technical components like the injection system, vacuum tubes, magnets, insertion devices, and beamlines (see figure 4.12):

-Injection system: Electrons are introduced in the injector system from the electron source, and an energy accelerator (mainly a linear accelerator and a booster

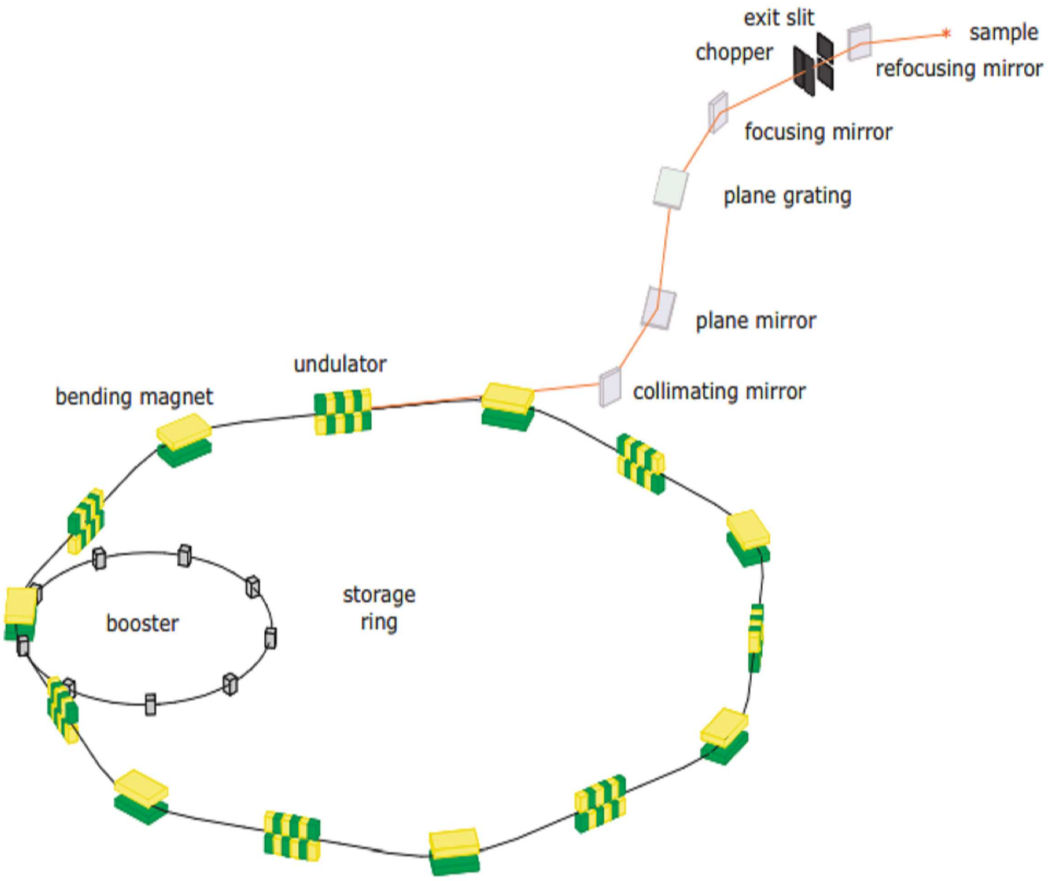

FIGURE 4.12: *Shmeatic view of a Synchrotron radiation source.*

synchrotron) accelerates, usually up to a few GeV, the electrons from the initial energy to the operating energy of the storage ring.

-Vacuum tubes: To avoid particle losses due to scattering on residual gas atoms, the electron beam must be enclosed in a vacuum tube where the air pressure is reduced to 10^{-9} mbar or lower. Electrons are expected to circulate inside the storage ring for several hours and produce synchrotron radiation with a minimum rate of loss. This low pressure is reached by placing several vacuum pumps along the circular path.

-Bending magnets: used to deflect the electron beam to follow a closed circular path in the accelerator. The geometry of the storage ring is defined by the position of the bending magnets. Bending magnets are also used as source of synchrotron radiation and the radiation they produce is always polarized in the plane of the

orbit and its emission spectrum ranges from the infrared to X-rays as a continuum, see figure 4.12-a.

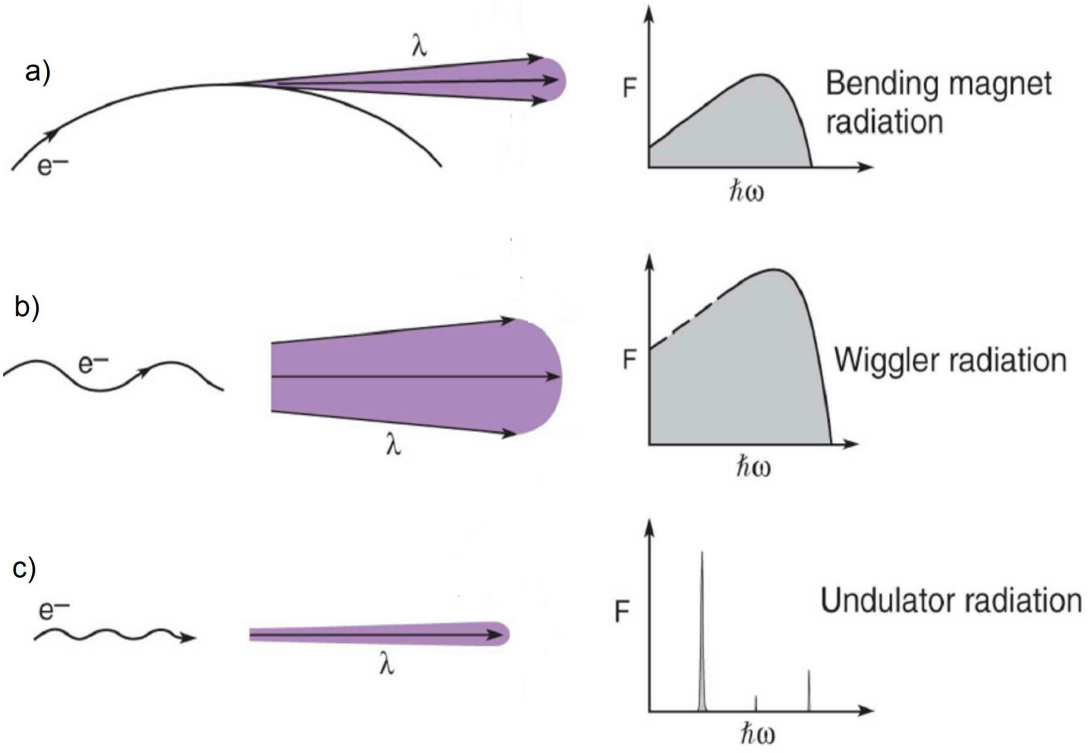

FIGURE 4.13: *a) electromagnetic radiation emitted from charged particles under acceleration providing by the Bending magnets. b) Wiggler, c) Undulator) used to increase the photon intensity and the brilliance of the photon beam.*

-Insertion device: to further improve the photon intensity and brilliance, insertion devices are located in the straight line sections between two consecutive bending magnets in the storage ring. These insertion devices, called undulators, are periodic magnetic structures where the beam is oscillating. If this oscillation is small, figure 4.13-c, interference between the electromagnetic waves results in a discrete spectrum with high intensities at photon energies for which the interference condition is fulfilled. With higher magnetic fields and longer periods the interference condition is lost and the undulator turns into a Wiggler figure 4.13-b. In this case, the resulting energy spectrum is continuous and determined by the sum of all the magnet periods rather than by the interference condition. It should be noted that there is no sharp distinction between undulators and wigglers. An

undulator can often be operated in a wiggler mode to deliver a continuous spectrum.

-Beamline: the beamlines used to convey the light to the experimental stations are installed tangentially to the storage ring and consist of a complex series of optical elements with very high precision. These elements are placed in vacuum condition to prevent the surface contamination. With the beamline, it is possible to select and direct the energy beam onto the sample placed typically at ten meters or more from the storage ring.

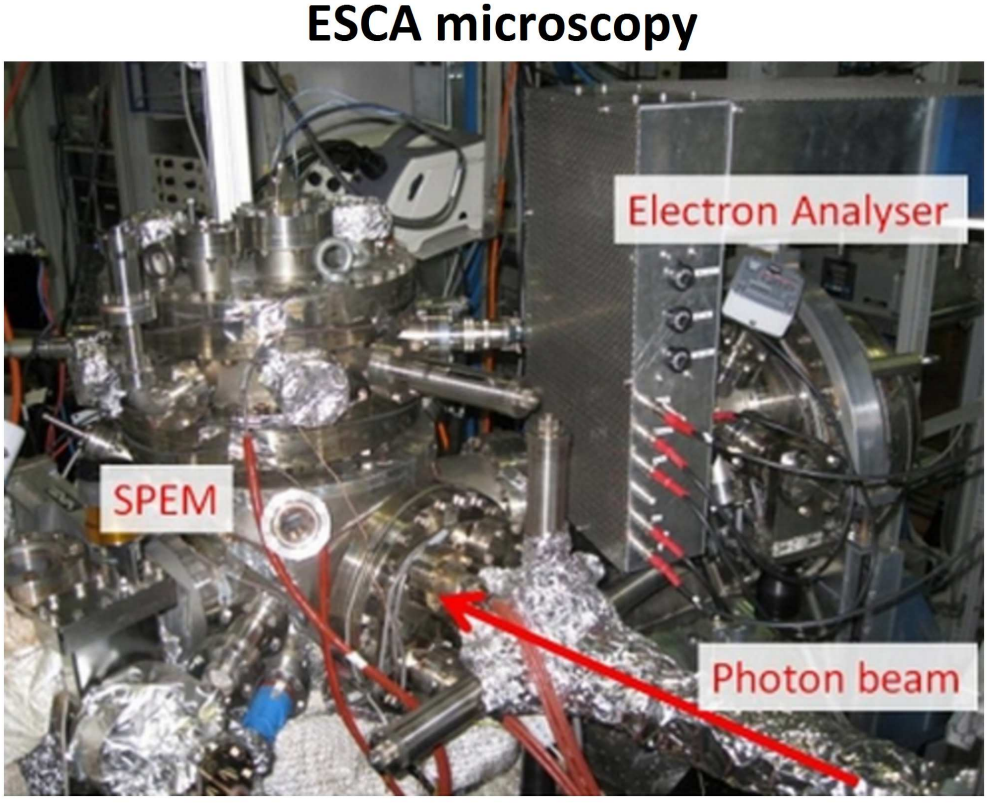

FIGURE 4.14: *The ESCA microscopy beamline at Elettra.*

4.4.3 SPEM on ESCA-microscopy

The geometry of the SPEM installed on the ESCA-microscopy beamline is drawn in the figure 4.15. Three important components are used in this technique: the first one is the Zone Plate optic system (ZP) to focus the photon light, the second one is the scanning system for the scanning images, and the third one is the

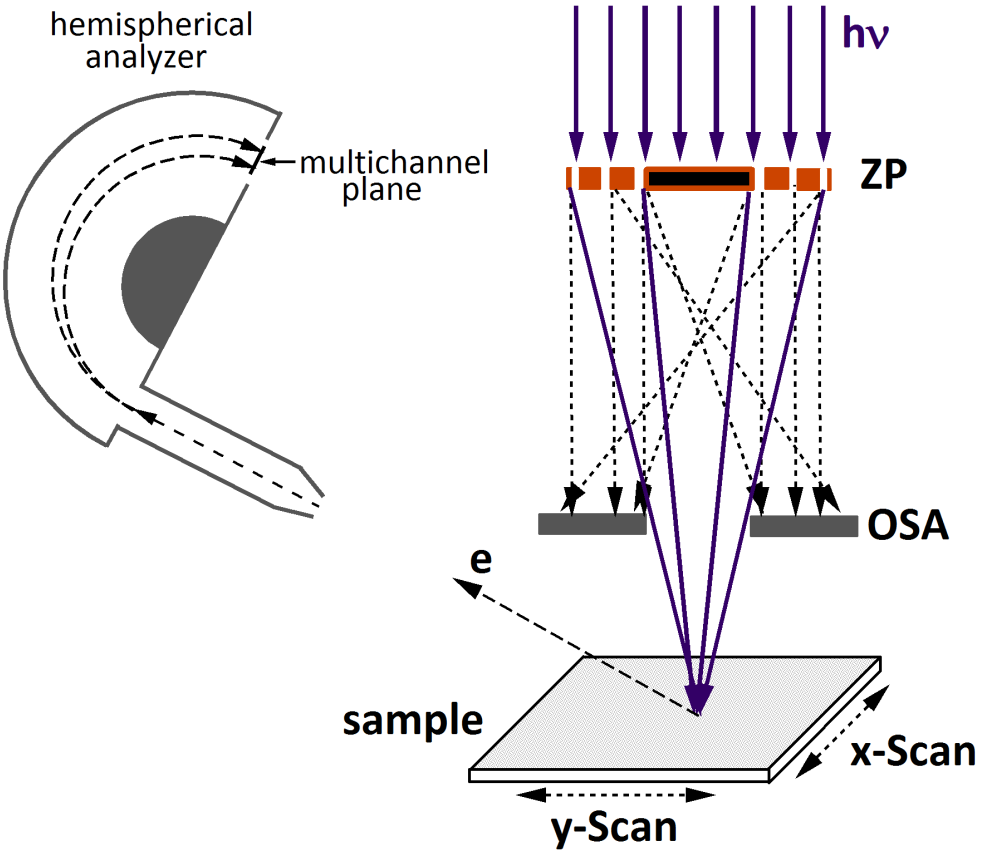

FIGURE 4.15: *The geometry of the SPEM technique in the beamline ESca-microscopy: after the light focusing on the sample by the Fresnel zone plates, the electrons are ejected from the surface into the analyzer.*

hemispherical electron analyzer with multichannel plate to measure the ejected ectrons.

4.4.3.1 Frensel zone plates

The Fresnel zone plate (ZP) consists of a circular (or elliptical) grating with line spacing and line widths varying in the radial direction, see figure 4.16. Light hitting the zone plate will diffract around the opaque zones. Using an order selecting aperture (OSA), mounted in the same z axis of the (ZP), the wanted diffracted order light is selected and focused into a spot due to constructive interference at the focal point. The diffraction limited spot size, in the first order of diffraction is approximately equal to the outermost zone width d (1.22*d); about 150 nm for the experiments presented in this thesis. Zone plates can be used over a rather

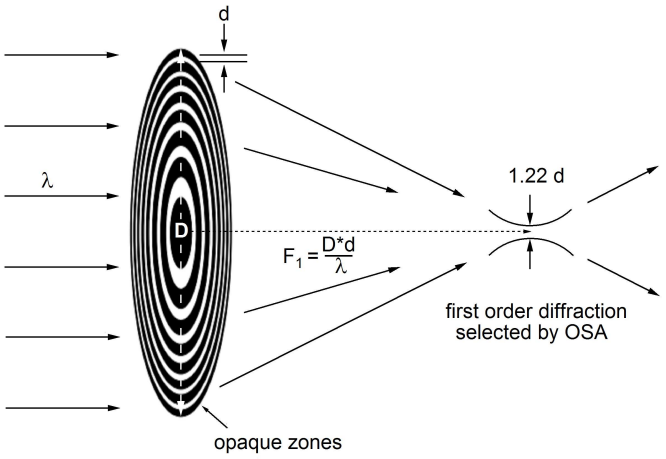

FIGURE 4.16: *Diffraction of the light beam using Frensel zone plates*

wide range of photon energies, but the focal distance varies with the energy, it's given by:

$$\mathbf{F}_n = \frac{D*d}{n\lambda}$$

where n is the diffraction order, D is the zone plate diameter, d is the outmost zone width and λ is the wavelength of the incident light. Hence, when the photon energy is changed, either the sample or the zone plates have to be translated to keep the sample in the focal plane. One of the disadvantages of the ZP-based SPEM system is the short focal length. When the photon energy is getting lower, the OSA needs to be placed closer to the sample, which can shade the emitted photoelectrons.

4.4.3.2 Scanning system

The sample manipulator is attached to a motorized fine stage which is in turn attached to a motorized coarse stage, see figure 4.17. By the movement of the sample using these two motorized stages, a scanning image can be taken from the sample surface. This image is the intensity distribution of photoemission yield, taken at different subsequent spots along the surface sample. The movement of the fine stage is along the sample surface with two directions (xy-type), with steps which can be as small as 1 nm. While the movement of the coarse stage is with

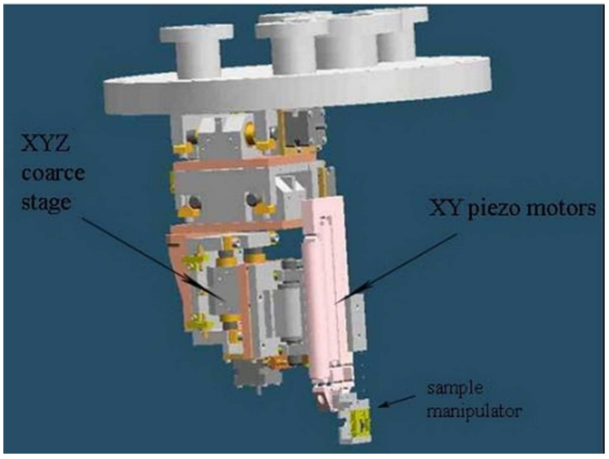

FIGURE 4.17: *The fine and the coarse motor stages attached to the sample manipulator*

large steps (micron size) . It has additional z-direction along the X-ray beam which is used to put the sample surface in the focal point.

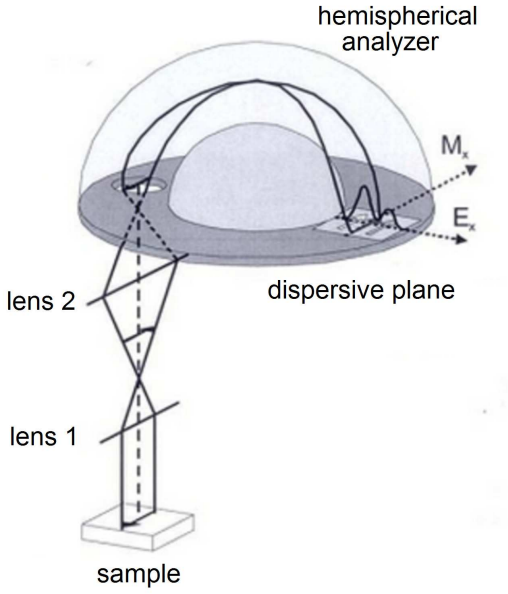

FIGURE 4.18: *Schematic view of the hemispherical electron analyzer using multichannel plate*

4.4.3.3 Multichannel plate

Like in a normal photoemission experiment, electrons are ejected from the sample and collected by the analyzer. Using different electronic lenses, the photoelectrons within a specific kinetic energy range are selected and projected to the channelplate

at the analyzer exit slit. The channelplate is constituted by a 48 channel electron cascade multiplier set along the dispersive plane of the analyzer, see figure 4.18. Consequently, each scanning image consists of 48 channels in which the energy window and the separation between channels depends on the pass energy of the analyzer: for example at pass energy 10 eV, the energy window is 2 eV. In this way, one can take images from selected regions on the sample collecting photoelectrons in the energy window covered by the multichannel plate. Conversely, one can also take conventional photoemission spectra from individual selected microspots on the sample.

Chapter 5

Ultrafast surface carrier dynamics in 3D topological insulators

5.1 Introduction

As already discussed in chapter 2, 3D topological insulators (3D TI's) are new states of quantum matter that are attracting a lot of interest due to the unique properties of their surface states. These surface states show massless Dirac fermions with linear energy-momentum dispersion. 3D TI's present different unique properties, such as topological and time reversal symmetry protection for the surface states, which are characterized by a helical spin structure. Their response to optical excitation shows many interesting phenomena such as surface spin current [81] and a large Kerr rotation [82]. In general, pump-probe spectroscopy can provide important information on the empty electronic states and on the relaxation of hot carriers.

However, when studying the optical properties of 3D TI's, one should consider the details of their surface states in k-space, in particular with respect to their bulk electronic structure [7, 9]. For example, a study of the optical response by ultrafast optical reflectivity [83, 84] or by optical spectroscopy [85] is not able to separate bulk and surface signals. So it is important to deepen these studies by distinguishing the response of the surface states from that of bulk states, with the purpose of understanding their coupling mechanisms and of selectively visualizing

the ultrafast response of the surface Dirac cone.

TR-ARPES (time and angle resolved photoemission spectroscopy) is an ideal experimental technique to explore the response of 3D TI's to ultrafast optical excitations [86]. Thanks to the surface sensitivity of ARPES and to its pump-probe configuration, with this technique one can follow at different time delays the dynamics of the photoexcited Dirac cone separately from that of bulk bands.

In this chapter I will present the application of TR-ARPES to the study of photoexcited surface and bulk states in the prototype 3D TI Bi_2Te_3. All crystals of Bi_2Te_3 used in this thesis are coming from the University Purdue, by a collaboration with I. Miotkowski and Y.P.Chen and the University Georgia Tech, by a collaboration with Z.Jiang. A first experiment, performed on n-type Bi_2Te_3 [87], shows how one can understand the carrier dynamics for both the surface and bulk states, as well as the different scattering mechanisms between these two states. A second study on p-type $Bi_{2.2}Te_3$ [88] presents another mechanism due to its specific propriety of the subsurface band bending, leading to a further bottleneck of the surface carrier dynamics.

5.2 Ultrafast surface carrier dynamics in n-type Bi_2Te_3

In this paragraph I will present a TR-ARPES study of the ultrafast surface carrier dynamics of both surface and bulk conduction bands in the n-type TI Bi_2Te_3. This was one of the first TR-ARPES experiments on 3D TI's: other measurements performed in parallel on the sibling compound Bi_2Se_3 confirmed our results, showing a persisting dynamics for the photoexcited Dirac cone [89], with the bulk states playing the role of electron reservoir, and pointing out that the recombination dynamics is assisted by surface-bulk phonon coupling [90, 91].

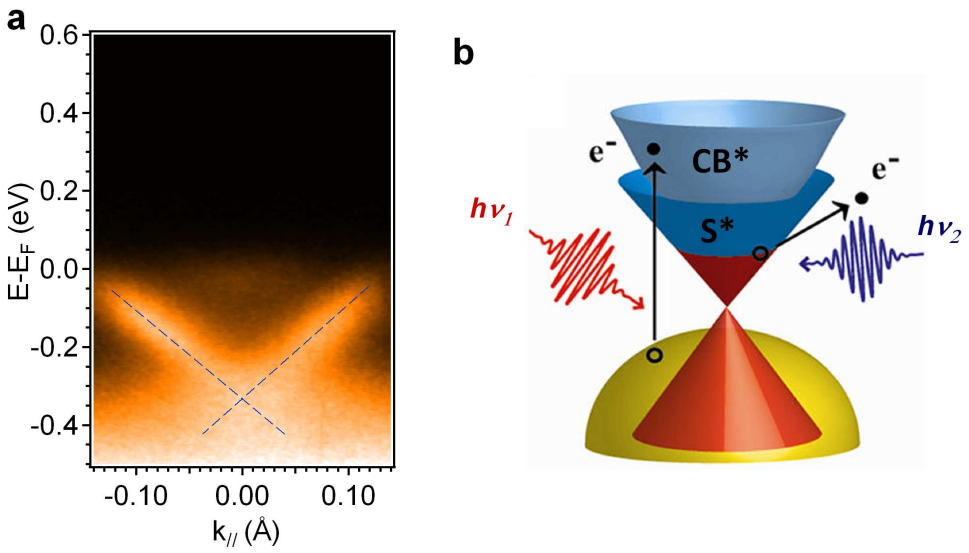

FIGURE 5.1: *a) ARPES image acquired along the ΓK direction in s-polarization with the laser source $h\nu_2$ = 6.32 eV . b) Pictorial view of the experiment; the infrared laser pump $h\nu_1$ = 1.58 eV excites electrons from the occupied state into the empty conduction band. The subsequent carrier flow produces a transient variation in the charge population of the surface Dirac cone, both for empty and filled electronic states and is probed by the ultraviolet probe $h\nu_2$ = 6.32 eV.*

5.2.1 Relaxation dynamics of the Dirac cone

A detailed description of the FemtoARPES experimental setup has been given in chapter 4, showing that the pump excitation hν_1 (35 fs, 1.58 eV) and the probe pulse hν_2 (50 fs, 6.32 eV) give an overall time resolution of 80 fs. The use of a 6.32 eV probe pulse gives access to a limited portion of k-space, but sufficient in this case to observe the entire Dirac cone. Using such a low energy photon source, the probing depth can be estimated to about 2-3 nm [58], which makes it possible to simultaneously detect the surface and the bulk electronic states.

Single crystals of Bi_2Te_3 were carefully oriented and cleaved along the [111] crystallographic direction and under ultrahigh vacuum conditions in the FemtoARPES experimental setup. Figure 5.1-a presents a conventional ARPES image along the ΓK direction. The results are consistent with previous ARPES studies at higher photon energy on Bi_2Te_3 [9] (figure 2.11); the surface Dirac cone is clearly visible (indicated by two dashed lines), along with an electron pocket for the conduction band consistent with the n-type character of Bi_2Te_3. In this chapter I will present

results obtained along the ΓK direction, where no hybridization is present between the surface Dirac cone and the bulk conduction band in the proximity of E_F (contrary to the ΓM direction, see figure 2.10). This allows to clearly distinguish, over an extended k-energy window, the transient populations of the unoccupied excited surface and bulk states, indicated as S* and CB*, respectively, in figure 5.1-b. I studied also other directions in k-space, and no relevant difference was found in the observed carrier dynamics, indicating that the hexagonal warping of the surface states in Bi_2Te_3 does not play a critical role in the ultrafast dynamics of this system.

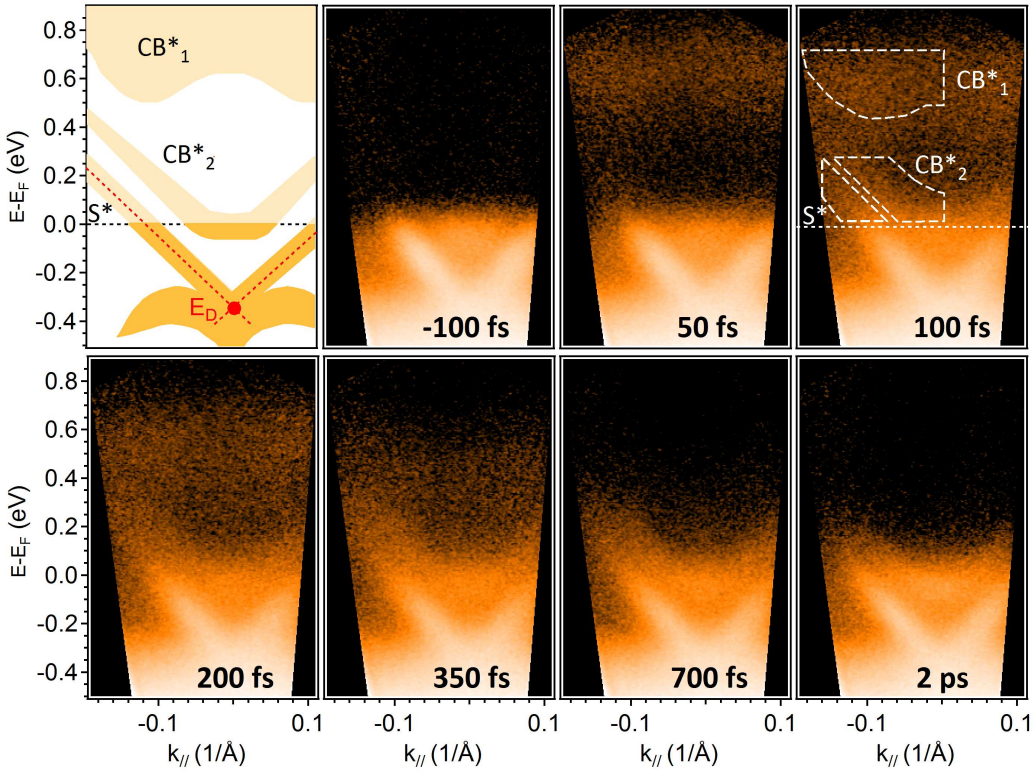

FIGURE 5.2: *Time-resolved ARPES sequence obtained after photoexcitation from the pump pulses. The color intensity is presented in logarithmic scale to make the signal from the transient electronic states more evident. In the upper left corner, a schematic view of the bands involved in the process: the projections of the bulk bands CB*$_1$ and CB*$_2$, and the surface Dirac cone S*. In the image (Δt = 100 fs), the integration regions CB*$_1$, CB*$_2$ and S* are defined.*

In Figure 5.2, I present the evolution of the TR-ARPES signal at room temperature and at different pump-probe time delays Δt. Following the pump excitation (0.15 mJ/cm^2), a transient excited electron population is observed in the high energy bulk band CB*$_1$, around 0.6 eV above E_F and at Δt = 50 fs. This transient

population relaxes quickly (in about 350 fs), activating a cascade of relaxation processes and acting as a source of electrons for the bulk conduction band CB^*_2, and for the surface band S* near E_F. In the upper left corner of figure 5.2 a schematic band structure of Bi_2Te_3 is presented, consistent with recent theoretical calculations [7] (figure 2.10), which can be used as a guide to the eye to interpret the data.

In order to get more quantitative information on the relaxation dynamics of surface and bulk states, I followed the evolution of the electron population in k-space, by integrating the signal within the dashed areas shown in figure 5.2 at a time delay of $\Delta t = 100$ fs. These integrated areas give the temporal evolution of the unoccupied bulk band CB^*_1, of the conduction band CB^*_2 and of unoccupied surface states S*. The separation between the conduction band CB^*_2 and the surface band S* is clear from the experimental data (for instance at $\Delta t = 700$ fs), so that our choice of the integration regions makes it possible to unambiguously follow the time evolution of each individual band.

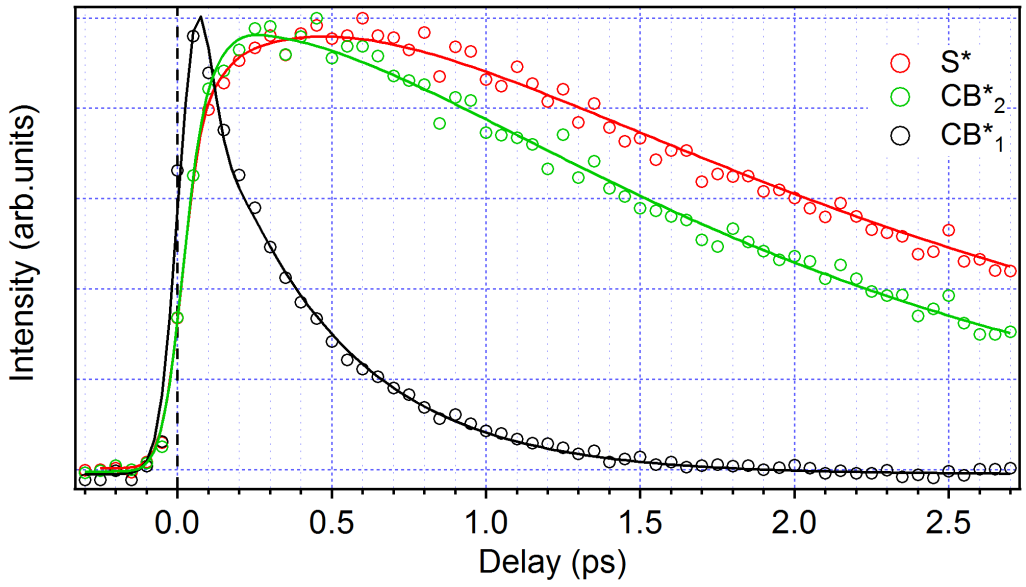

FIGURE 5.3: *The temporal evolution of the electronic population in the different k-energy windows CB^*_1, CB^*_2 and S*.*

Figure 5.3 shows the time evolution of the transient populations in these k-energy windows. The ultrafast carrier dynamics between the surface and the bulk can be described using a standard rate equation model for semiconductors to fit the

population curves S*(t) and to identify the main charge flow processes to and from the surface bands [92, 93]. Nevertheless, in the case of Bi_2Te_3 one is not confronted with weakly dispersing surface resonances normally found in standard semiconductors; on the contrary, the surface bands are metallic, strongly dispersing and cross the bulk energy gap. This makes it necessary to adopt an alternative approach to study their relaxation.

On the basis of the assumption that CB_1^* acts as a source of excess electrons that adds up to direct excitation for CB_2^* and S^*, the main carrier interband scattering processes can be described by the following equations:

$$\frac{dCB_1^*}{dt} = G_1(t) - \frac{CB_1^*}{\tau_1} \tag{5.1}$$

$$\frac{dCB_2^*}{dt} = G_2(t) + \frac{CB_1^*}{\tau_{12}} - \frac{CB_2^*}{\tau_2} \tag{5.2}$$

$$\frac{dS^*}{dt} = G_{S^*}(t) + \frac{CB_1^*}{\tau_{1S}} - \frac{S^*}{\tau_S} \tag{5.3}$$

The flow of charge to S^* (t) is described by direct excitation from the laser pulse G_{S^*} (t), by a flow of electrons from the CB_1^* (t) projection of the bulk conduction band with characteristic time τ_{1S}, and by the recombination processes for excess electrons described by τ_S. CB_2^* (t) can be also described by direct excitation, by interband scattering from CB_1^* (t) with characteristic time τ_{12}, and by a decay time τ_2: its proximity with S^* would suggest that an interband scattering term should be considered, but as a first approximation we preferred to neglect it and simply compare the values obtained for τ_2 and τ_S. We used the solutions of these coupled differential equations as fitting functions for our population curves CB_1^* (t), CB_2^* (t) and S^* (t), obtaining as a result the curves shown as solid lines in figure 5.3, and corresponding respectively to the following values of the fitting parameters:

fwhm of 76 fs for G_1, G_2, and G_{S^*}; $\tau_1 = 0.35$ ps, $\tau_{12} = 0.53$ ps, $\tau_2 = 1.8$ ps, $\tau_{1S} = 0.55$ ps, $\tau_S = 2.1$ ps.

The decay time of $CB1^*$ is about 350 fs and is clearly related to the time needed for both CB_2^* and S^* to reach the maximum population change. The very similar values of τ_{12} and τ_{1S} can be associated to similar scattering times with the surface and the conduction bands. Furthermore, τ_S and τ_2 are very similar, indicating that S^* and CB_2^* present a parallel evolution; even though we did not explicitely insert a scattering term between them in the rate equation, this similarity indicates that an effective carrier exchange takes place between the two bands.

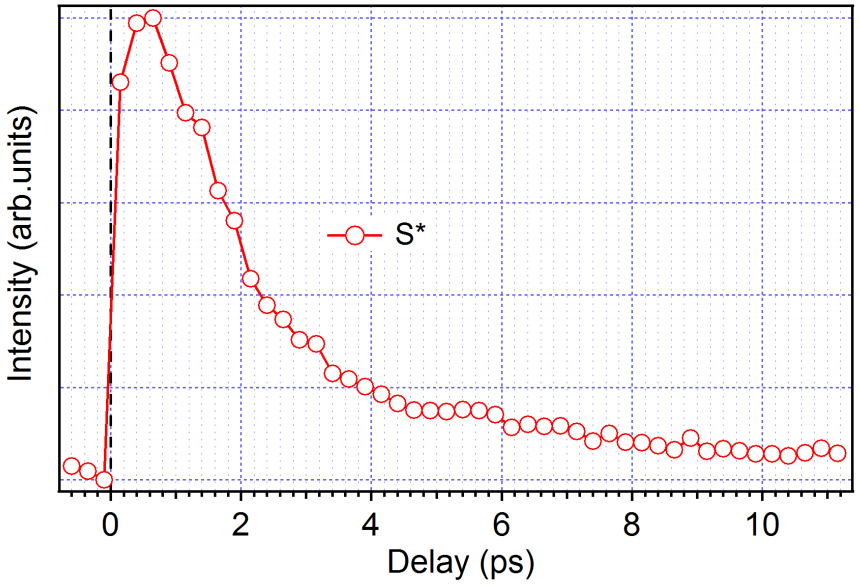

FIGURE 5.4: *The temporal evolution of the transient population in the k-energy window S* at longer time delays.*

The longer scans (figure 5.4) show that after about 10 ps S^* is back to its values before excitation. This decay is unusually long for a metallic system. It is found also on p-type Bi_2Se_3 [89], where the authors also found a transient surface state population persisting for more than 10 ps due to the reservoir role played by the bottom of the conduction band. The fact that different materials with different doping levels show this effect suggests that a slow relaxation of surface hot electrons should be an intrinsic property of TI's.

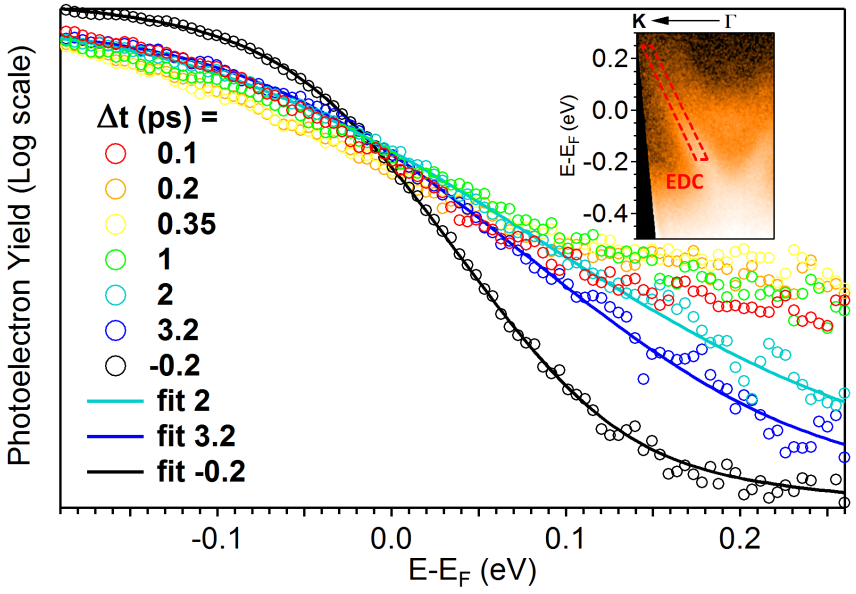

FIGURE 5.5: *EDC's along the surface state at different pump-probe delays. For the spectra at -0.2, 2, and 3 ps, I also present the corresponding fits with a Fermi-Dirac distribution. The photoemission yield is presented in logarithmic scale. In the inset, the corresponding momentum integration area is shown.*

5.2.2 Thermalization of excited Dirac electrons

A more precise information can be obtained on the electronic structure of the photoexcited surface states by looking at the details of the energy distribution curves (EDC's). Figure 5.5 presents the EDC's extracted from the surface bands (the momentum integration regions are visible in the inset) at some representative time delays; these curves can give a direct description of the Dirac cone during its thermalization process. One can see that for the longer delays, namely 2, 3, and -0.2 ps after the pump-pulse, the EDC's can be well fitted with a Fermi-Dirac distribution (the spectra at 2 and 3 ps give an electronic temperature of 792 and 619 K, respectively). For shorter time delays, that is, 0.1, 0.2, and 0.4 ps, the EDC's cannot be fitted with a Fermi-Dirac distribution. This is different from the case of Bi_2Se_3 [91] and is due to a strong presence of electrons at high energy, indicating that the system is not thermalized yet; at these delays, the population of S* is still increasing due to the flow of charge from the bulk bands.

5.2.3 Conclusion

In conclusion, using TR-ARPES, I provided a direct visualization of the excess carriers population of both the surface Dirac cone and the bulk conduction band in n-type TI's Bi_2Te_3. Transient excited bulk states at high energy act as a reservoir that keeps providing a relevant charge flow for the surface Dirac cone and the conduction band for more than 0.5 ps: as a consequence, the thermalization of both surface and bulk conduction band excess electrons is delayed. A similarity in the relaxation between the surface Dirac cone and the conduction band is due to charge diffusion and scattering between the two states. Photoexcited surface states are back to equilibrium after more than 10 ps, an unusually long time for a normal metallic system. The results presented here appear of general interest also for other 3D TI's in particular for possible technological applications of these materials.

5.3 Ultrafast and asymmetry carrier dynamics in p-type $Bi_{2.2}Te_3$

As I showed in the last section the surface recombination in topological insulators can be well assisted by the presence of the conduction band. In this section I will show how the interplay of surface and bulk transient carrier dynamics can be disentangled by studying a p-type compound. Furthermore, I will show that for the p-type $Bi_{2.2}Te_3$, showing a preexisting band bending, one can control the balance between excess electrons at the surface and holes in the bulk states, which leads to a further bottleneck for the carrier recombination in the Dirac cone.

5.3.1 Band bending after pump excitation

5.3.1.1 Electronic surface states and band bending

At the crystal surface of a semiconductor, the periodic pattern of chemical bonds is interrupted at the surface-vacuum interface, causing the formation of dangling

bonds. These dangling bonds can rearrange themselves to give a surface reconstruction, i.e. a change of the surface crystal structure, which differs in general from the bulk. The energies of surface electronic states are frequently located inside the band gap, forming a two-dimensional electron band of surface states. These states can have contributions from either the conduction or the valence bands, and in some cases can be a mixture of both types of bands.

In the case of an intrinsic semiconductor (undoped semiconductor, figure 5.6-a), due to charge neutrality, the number of filled surface states is equal to the number of electrons that were removed from the bulk valence band, resulting in a neutral or uncharged surface. The remaining surface states are empty. The energy up to which the surface states are filled is dictated by charge neutrality and is referred to as the charge neutrality chemical potential μ_0.

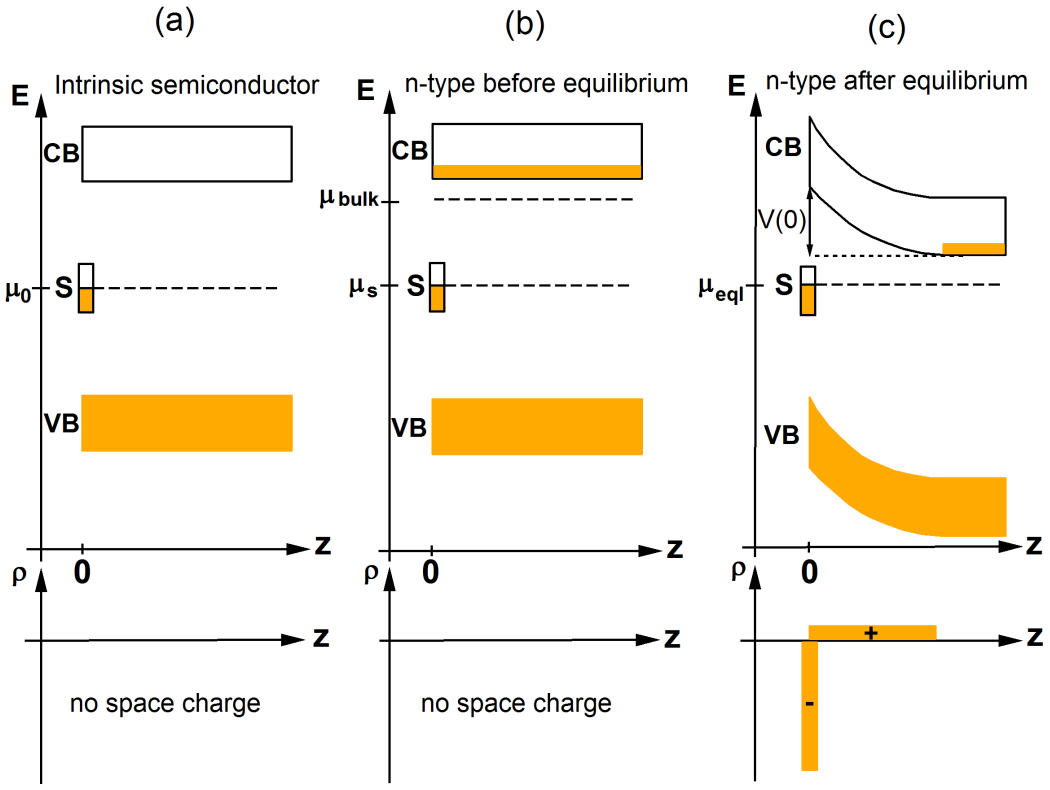

FIGURE 5.6: *a) band structure at the surface of an intrinsic semiconductor, b) n-doped semiconductor before equilibration, c) after equilibration. The yellow color indicates occupied states. To match the chemical potentials at the surface and in the bulk, charge builds up on the surface placing the donor charges into the bulk and consequently bending the bands.*

For the surface of a doped semiconductor (n-type for example, figure 5.6-b), to

match the chemical potentials at the surface and in the bulk, electrons occupying the conduction band (holes in valence band for p-type) can lower (rise in p-type) their energy by filling empty surface band states (figure 5.6-c). This gives a net negative surface charge (positive in p-type) which is balanced to maintain charge neutrality by a region inside the crystal of equal total positive charge (negative in p-type), referred to as depletion region. The positive charge in the depletion region is due to holes left behind by electrons from the conduction band, and results into a potential V(z) in this region and consequently gives an upward band bending (the opposite case is found for p-type compounds)[92, 94, 95].

To give a more quantitative description of this effect, let us call z_{dep} the extent of the depletion region into the bulk starting from the surface at $z = 0$, and N_d the dopant density. All donors are ionized in the depletion region, giving a space charge density of $\rho = eN_d$. Using the Poisson equation one can determine the z-dependence of the potential $V(z)$ within the depletion region $0 < z < z_{dep}$ as:

$$V(z) = -\frac{e\rho}{\epsilon\epsilon_0}(z - z_{dep})^2 \tag{5.4}$$

with $V = 0$ for $z > z_{dep}$. According to this equation, bands have bent by a total amount of $\Delta V = V(0) = \frac{e\rho}{2\epsilon\epsilon_0} z^2_{dep}$. If one compares the Fermi level position with respect to the valence or the conduction band position at $z = 0$ (at the surface) with the one at $z > z_{dep}$ (in the bulk), one can determine the pinning of the Fermi level, and estimate the value of z_{dep} as:

$$z_{dep} = \sqrt{\frac{2\epsilon\epsilon_0\Delta V}{e\rho}} \tag{5.5}$$

5.3.1.2 Separation of charges after pump excitation

After pump excitation, the absorption of photons with energy hν higher than the bandgap creates electron-hole pairs. Due to the near-surface potential V(z) in the bent region, the electron-hole pairs will separate as the produced free charge carriers move in different directions. In the case of upward bent bands, for n-type semiconductors, free electrons drift to the bulk and free holes move towards

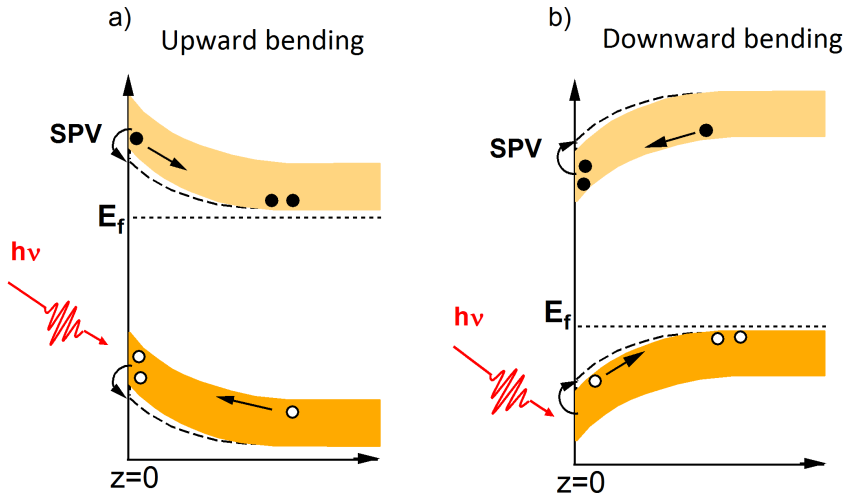

FIGURE 5.7: *a) upward band bending b) downward band bending bending, after pump excitation, causing a partial band flattening*

the surface causing a partial band flattening (figure 5.7-a). The opposite case occurs for p-type semiconductors with downward bent bands; upon irradiation free electrons transfer to the surface and free holes move towards the bulk, causing the degree of downward band bending to decrease (figure 5.7-b). This effect is known as the surface photovoltage (SPV) [92]. In the case of high photon flux, the SPV can be saturated and the energy bands may be completely flattened.

5.3.2 Two TI's with and without band bending

In the following I will present a TR-ARPES study of two photoexcited TI's compounds: a highly doped n-type compound (Bi_2Te_3) with flat bands at the surface, and a p-type compound ($Bi_{2.2}Te_3$) obtained with a Bi-rich stoichiometry and presenting a downward band-bending at the surface. The band lineup was precisely determined by considering the bulk carrier concentration extracted from transport measurements, evaluating the band position with respect to E_F in the bulk, and then comparing it with the band position at the surface as observed with ARPES. According to transport measurements, Bi_2Te_3 exhibits an electron density in the bulk n = 10^{21} cm^{-3} with a mobility $\mu = 0.012$ m ^{2}.V^{-1}.s^{-1} while $Bi_{2.2}Te_3$ exhibits a hole density in the bulk $n_h = 9\ 10^{18}$ cm^{-3} with a mobility $\mu_h = 9300$ cm ^{2}.V^{-1}.s^{-1}. Figure 5.8 presents conventional ARPES images using 6.32 eV photons along the

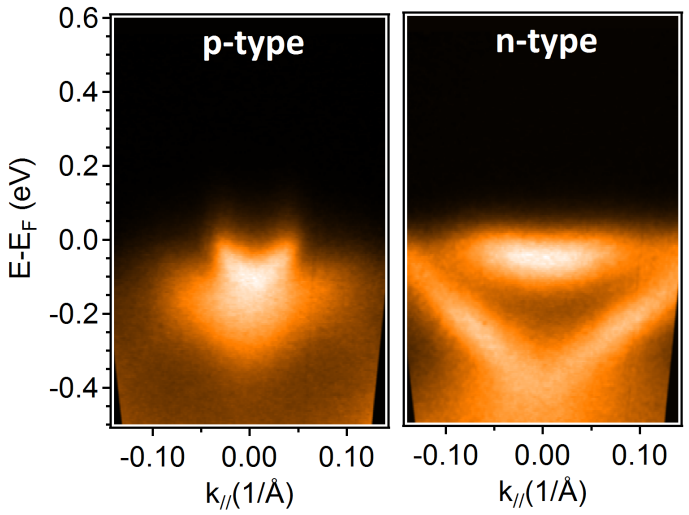

FIGURE 5.8: *ARPES images acquired along the ΓK direction in s-polarization with the $h\nu_2$ = 6.3 eV laser source for a) n-type Bi_2Te_3 and b) p-type $Bi_{2.2}Te_3$.*

ΓK direction, taken at 130 K for both compounds. In Bi_2Te_3 the E_F lies almost 85 meV below the bottom of conduction band E_c. And in $Bi_{2.2}Te_3$ the E_F position is about 30 meV with respect to the top valence band position E_c.

In order to estimate the E_F position in the bulk respect the E_c position for the n-type Bi_2Te_3 and to the E_v position for the p-type $Bi_{2.2}Te_3$, one can use standard semiconductor formulas:

$$E - E_c = K_B T \ln(\frac{N_c}{N_d}) : \text{(n-type)}$$

$$E - E_v = - K_B T \ln(\frac{N_v}{N_a}) : \text{(p-type)}$$

$$N_{c,v} = 2(\frac{2.\pi.m^*_{e,h}.K_B T}{h^2})^{3/2}$$

where N_d or N_a is the doping concentration of the donors or acceptors for the n and p sample, respectively, which is approximately equal to the carrier concentration given by transport measurements, and $m^*_{e,h}$ is the effective mass of electrons (e) or holes (h) in Bi_2Te_3.

These equations give: $E - E_c$ = 90 meV for Bi_2Te_3, consistent with the ARPES measurment and indicating that the bands are flat at the surface. While in $Bi_{2.2}Te_3$ $E - E_v$ = - 40 meV, so that the comparaison with the ARPES measurements gives

a pinning of the Fermi level of about 70 meV in this system. Using the formula 5.5, one can estimate in $Bi_{2.2}Te_3$ a depletion region z_{dep} of about 10 nm.

5.3.3 TR-ARPES on $Bi_{2.2}Te_3$ and Bi_2Te_3

5.3.3.1 Sequence of Tr-ARPES

In figure 5.9 I present the results of the TR-ARPES experiments performed on the two samples (p-type, figure 5.9 -a, and n-type figure 5.9 -b) for selected time delays Δt after the pump laser pulse.
The data presented here are taken along the ΓK direction at 130 K and 40 K for $Bi_{2.2}Te_3$ and at 130 K for Bi_2Te_3. Measurements were also performed at room temperaure for both systems, but no substantial differences were found with respect to those performed at 130 K. In figure 5.9-c I present the time evolution of the populations in the k-energy windows CB^*_n, CB^*_p (bulk conduction bands) and S^*_n, S^*_p (excited Dirac cones) as defined the image of figure 5.9-a-b at $\Delta t = 100$ fs. As we have seen in 5.2 for slightly n-doped Bi_2Te_3, also for the two systems presented here an excess carrier population builds up in the Dirac cone and the conduction band during the first picoseconds, as a result of different interband scattering processes with higher energy bulk states.

At longer delays, n-type Bi_2Te_3 is almost completely relaxed after 6 ps. This is faster than for the slightly n-doped specimen, probably due to a contribution of conduction band electrons to the overall scattering and recombination processes. Conversely, in the p-type sample a significant population of excess hot carriers survives in the surface Dirac cone for a much longer time: 30 ps at 130 K, and even more (about 50 ps) at low temperature (40 K).
For $\Delta t > 10$ ps, the surface Dirac cone for p-type $Bi_{2.2}Te_3$ is filled with hot electrons within the gap, with the remarkable consequence that there are no carriers at the bottom of the bulk conduction band CB^*_p. This interesting situation is not trivial to be found. For example, it is in stark contrast with the p-type Bi_2Se_3 [89], where the bulk conduction band was found to act as a charge reservoir, which keeps filling the Dirac cone states in the gap persisting until complet relaxation for about 10 ps,

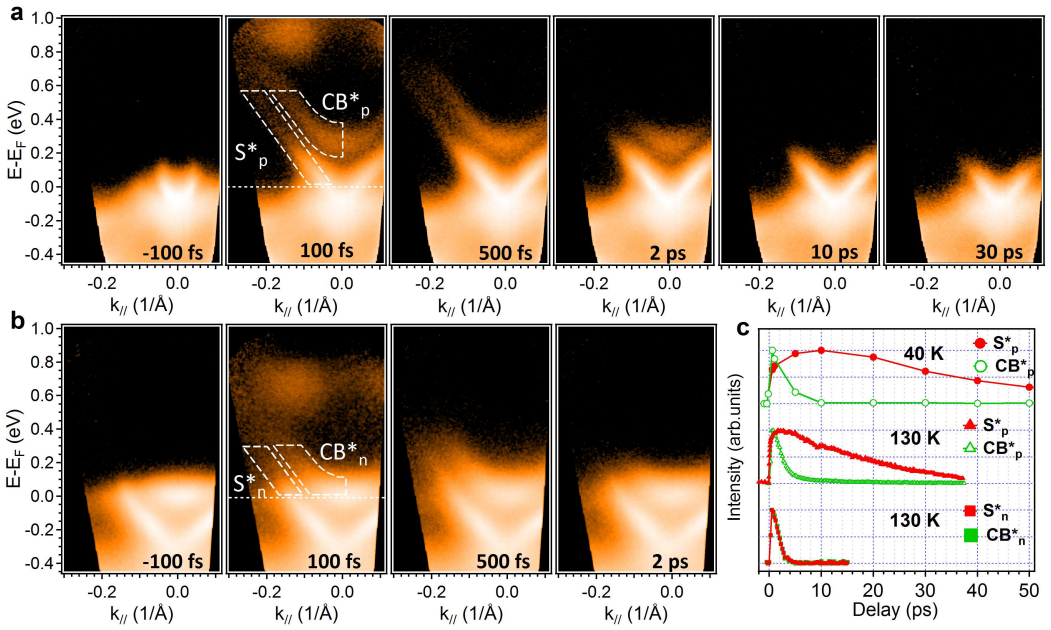

FIGURE 5.9: *Time-resolved ARPES measurements on (a) p-type $Bi_{2.2}Te_3$ and (b) n-type Bi_2Te_3. The signal intensity is presented in a logarithmic color scale. The integration regions called S^*_p, S^*_n, and CB^*_p, CB^*_n are indicated as dashed contour windows. (c) time evolution of S^*_p, S^*_n, CB^*_p, CB^*_n*

so that a non-equilibrium population of bulk photoinduced carriers CB^*_p always coexists with the hot electrons in the Dirac cone.

In order to compare the dynamics of the photoexcited Dirac cone with respect to the conduction band, in figure 5.10, I plot the transient photoemission intensity obtained by integrating within the k-energy windows shown in the inset: S_i for the excited surface states and B_i for the excited bulk states (i is the index of the k-energy window). Above the bottom of the conduction band (BCB) and starting from window number 2, the surface states and the conduction band have the same time decays, proving that an effective carrier exchange takes place between the two bands. The same behavior is also observed in n-type Bi_2Te_3, since the excited surface state is also close to the excited conduction band. In this time window the bulk states act as relaxation channel for the surface states, giving a fast dynamics. However, below the BCB (windows S_g and 1 are in the gap) a slower dynamics is observed, reflecting the absence of the fast bulk recombination, and indicating that recombination processes involving only surface states give large decay times, due for example to the weak electron-phonon coupling of these states [96]. Moreover,

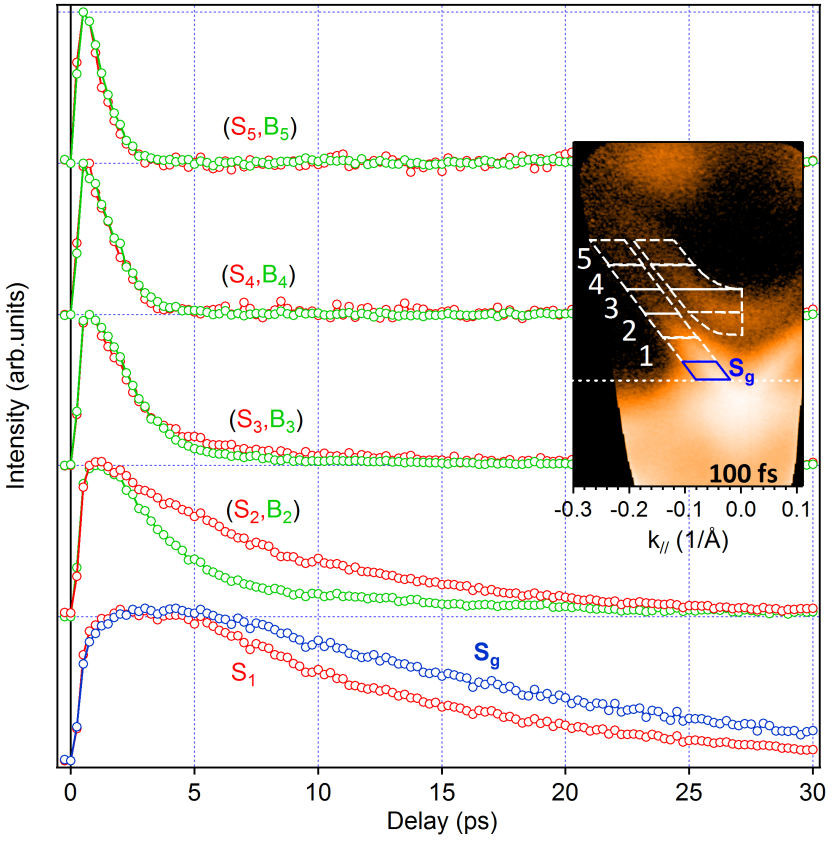

FIGURE 5.10: *Transient photoemission intensities within the integration windows indicated in the inset.*

above the BCB, the maximum of the transient population of the different excited states is at less than 2 ps, while within the gap it is about 4 ps, which also confirms the overall slower dynamics of the surface states within the gap.

5.3.3.2 Asymmetry of photoexcited Dirac fermions

The reasons for the longer dynamics of our p-type $Bi_{2.2}Te_3$ can be identified by analysing the interplay of electron and hole carrier dynamics, related to the band bending present in this system. In figure 5.11-a and 5.11-c, I present the differences of various ARPES images with respect to the negative time delays at 40K and 130K in the p and n sample, respectively. In figure 5.11-b and 5.11-d, I present the time evolution of the detected electron and hole populations for the two systems. During the first 2 ps, for the n-type sample a substantial symmetry is present at all delays between excess electrons and holes. Conversely, for the p-type specimen after 500

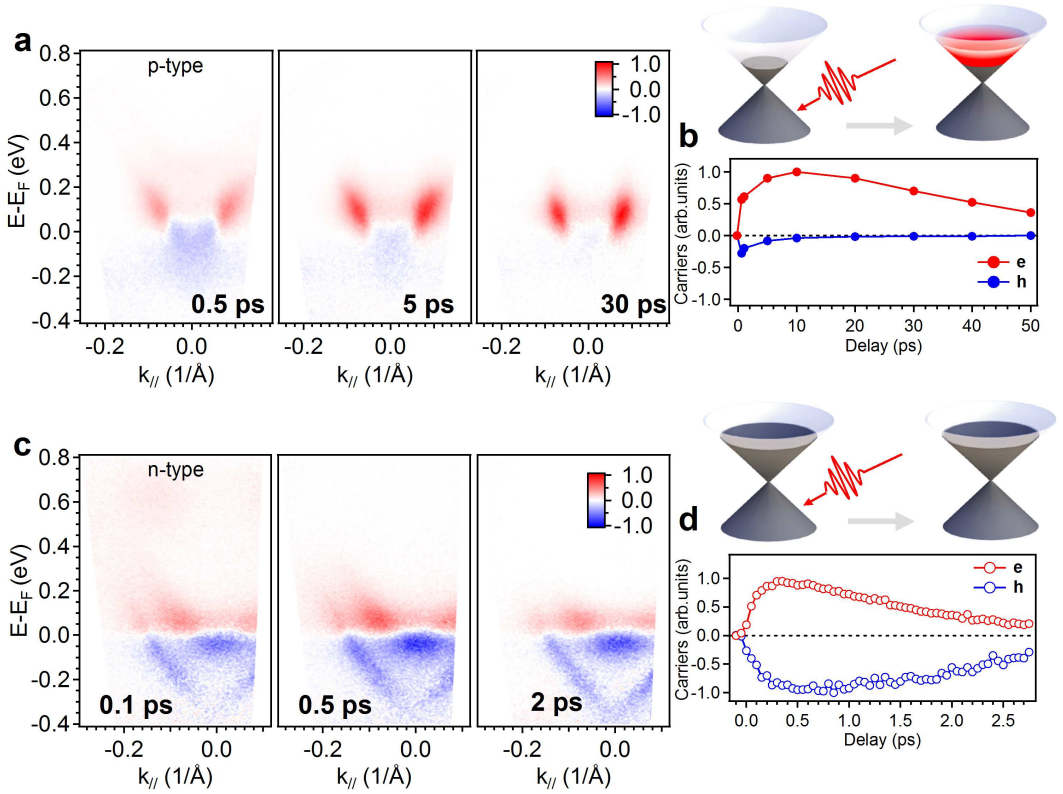

FIGURE 5.11: *Transient excess electrons (red) and holes (blue) as detected from the difference of time-resolved ARPES images between positive and negative time delays for (a) p-type $Bi_{2.2}Te_3$ and (c) n-type Bi_2Te_3. In (b) and (d) we present the time evolution of the detected excess carriers (electrons, e and holes, h) for the two samples (p-type and n-type).*

fs the hole population starts decreasing in the surface layers (the probing depth is about 2-3 nm) while excess electrons maintain a strong presence and are actually trapped into the surface states. This is due to the preexisting band bending for the p-type sample, which causes a flow of the excess majority carriers (holes) towards the bulk, while the excess minority carriers (electrons) remain confined at the surface. The temperature dependence of the relaxation dynamics, which is longer at 40 K than 130 K can be explained by the temperature dependence of the bulk mobility of the carriers, since the carriers drift slower towards the bulk at low temperature. For the laser fluences used in this study the corresponding transient SPV was found to be negligeably small (10 meV), so that it does not change significantly the initial band bending. As a consequence in the following I will not consider these small effects.

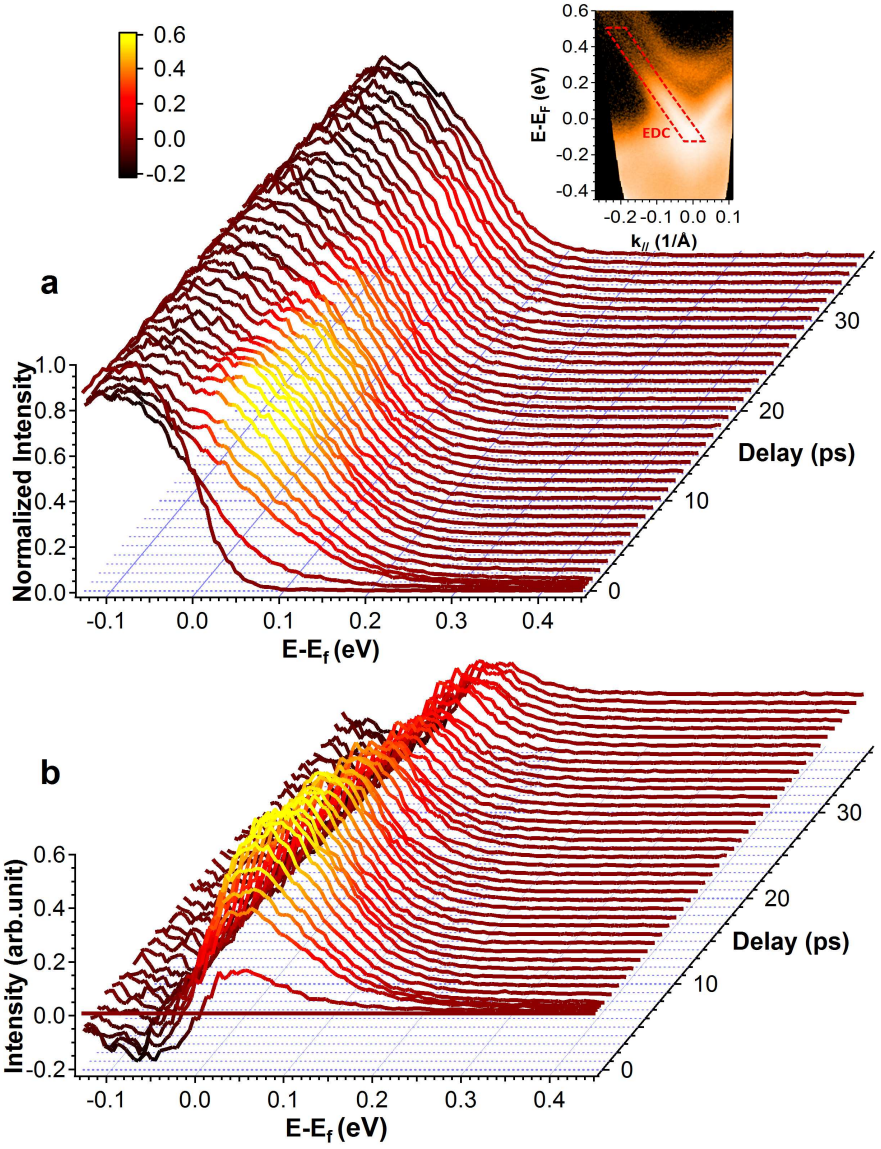

FIGURE 5.12: *a) EDC's taken along the surface Dirac cone of p-type $Bi_{2.2}Te_3$ at 130 K for different pump-probe delays Δt. In the inset, the corresponding momentum integration area is shown. The vertical axis is the normalized intensity of the EDC's, while the color scale intensity indicates the difference of the photoelectron yield with respect to the non-excited system (b).*

5.3.3.3 Energy Distribution Curves (EDC's)

A detailed analysis of the Energy Distribution Curves (EDC's) gives a more complete description of the evolution of this strongly non equilibrium Dirac cone. Figure 5.12-a presents the EDC's taken along the surface bands of p-type $Bi_{2.2}Te_3$ at T = 130 K for different time delays Δt. In order to better visualize the hot fermions, the color scale intensity indicates the difference of the photoelectron

yield with respect to the non-excited system shown in figure 5.12-b: for each time delay Δt, I present the difference of the relative EDC with respect to the EDC at negative time delay (Δt = -0.25 ps).

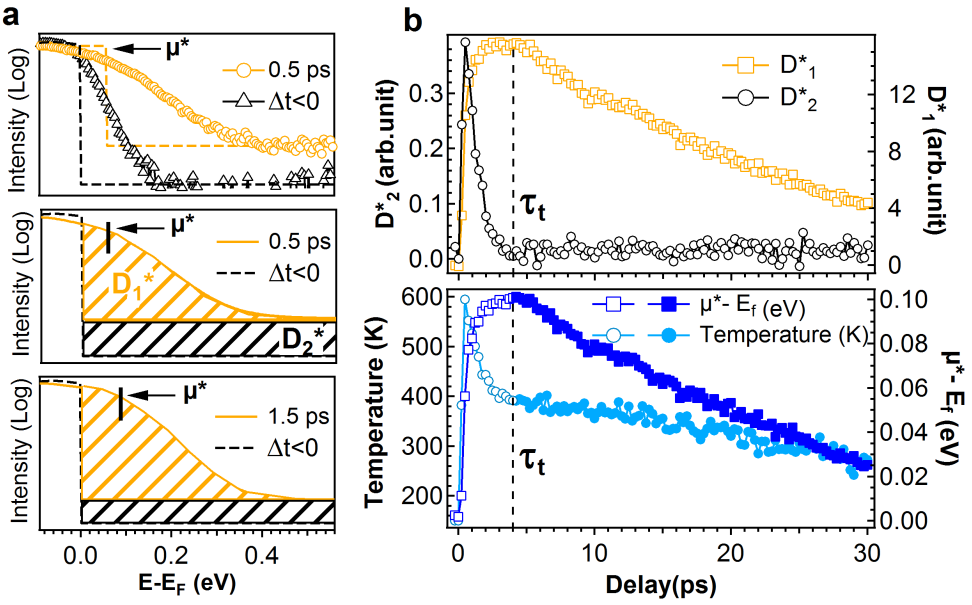

FIGURE 5.13: *a) Top panel: difference between the EDC at Δt = 0.5 ps and Δt < 0; medium and bottom panels: visualisation for two time delays of D^*_1 and D^*_2, parameters used to fit the transient electronic states with a Fermi Dirac distribution as explained in the text. (c) Time evolution of the fitting parameters.*

Figure 5.13-a presents the EDC's in logarithmic scale for two limiting cases, Δt < 0 (non excited state) and Δt = 0.5 ps (strongly out of equilibrium). The EDC for Δt < 0 can be well fitted with a Fermi-Dirac distribution with T_e = 130 K, convoluted with our experimental resolution 80 meV (figure 5.14). The spectrum for Δt = 0.5 ps presents a non zero signal level at high kinetic energies, a background due to incoming scattered electrons with the bulk states. To model the EDC, we describe this background with a constant energy distribution D^*_2 for E > μ^*, where μ^* is the chemical potential describing the rest of the excess population D^*_1, plus a Fermi-Dirac distribution with temperature T_e and the chemical potential μ^*. This model makes the somehow artificial assumption that an electronic temperature T_e can be defined only at time delays where $D^*_2 = 0$. Nevertheless, it provides a good fit for the spectra at all delays shown in figure 5.14. The parameters extracted from the fit are plotted in 5.13-b, and indicate that a real electronic thermalization

develops only when $D^*_2 = 0$ and when μ^* reaches its maximum value (about 0.1 eV, figure 5.14) at $\Delta t = \tau_t$ (τ_t = 4 ps at 130 ps and 10 ps at T = 40 K). When $D^*_2 \neq 0$, parameters like μ^* and T_e are physically ill-defined, and I report them in 5.12-c with different symbols for sake of clarity: this distinction is particularly clear here because the band filling ($\Delta t < \tau_t$) and its quasi-adiabatic relaxation ($\Delta t > \tau_t$) take place on well distinct time scales.

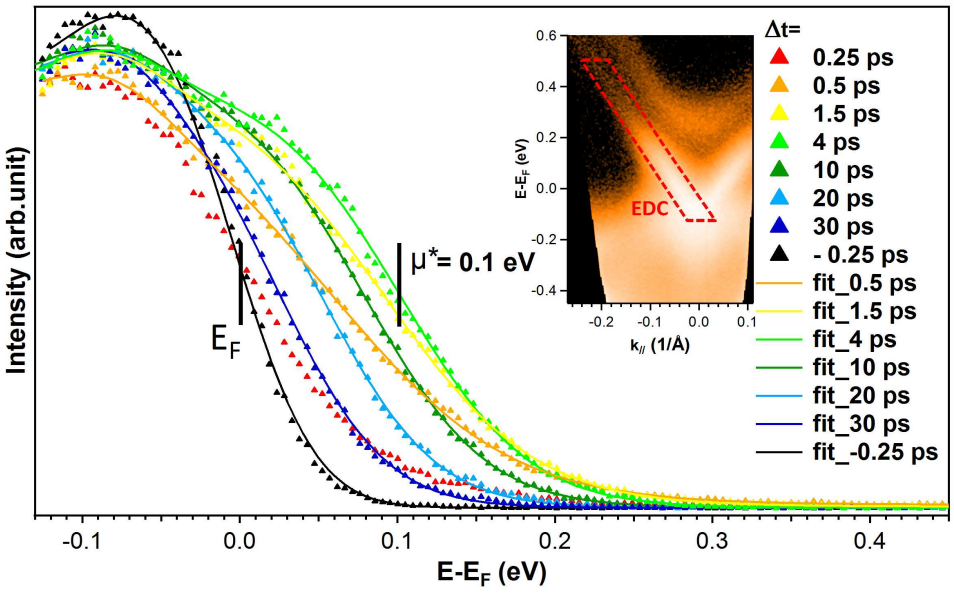

FIGURE 5.14: *Energy Distribution Curves taken along the Dirac cone for p-type $Bi_{2.2}Te_3$ (the integration region is indicated in the inset). The fitting curves are shown as solid lines.*

5.3.3.4 Genuine transient 3D TI's

Figure 5.15 presents the consequences of the spatial separation of photoexcited negative and positive carriers in $Bi_{2.2}Te_3$. After excitation (b), the excess electrons fill the surface Dirac cone over few ps. And after 10 ps (c) there are no visible electrons in the conduction band, nor are there any excess holes in the subsurface valence band, because a strong excess population of electrons concentrated in the conducting surface states while no excess carriers are present in the bulk bands. The chemical potential μ^* intersects only the surface states, indicating fully gapped bulk states as is expected for a 3D topological insulators.

As we discussed in 5.3.3.1, this is the first time that this is shown for the transient

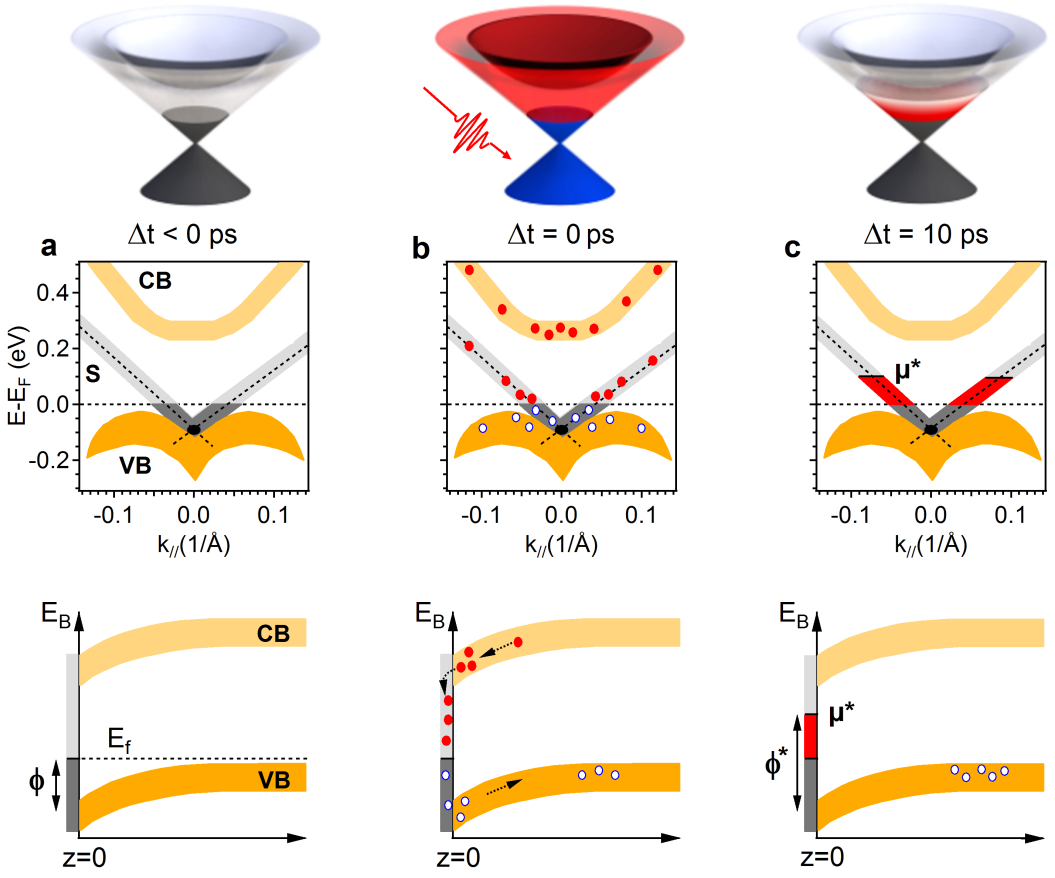

FIGURE 5.15: *A comparaison of $Bi_{2.2}Te_3$ (a) in its ground state, (b) after photoexcitation and (c) in its photo-excited state for a delay Δt = 10 ps after optical pumping. For each case, the top panel represents a pictorial view of the Dirac cone with excess electrons (red) and holes (blue); the mid panel shows the schematic structure of the bands in reciprocal space and their filling at the surface (z=0); and the bottom panel the corresponding band lineup in real space along the normal to the surface z.*

regime: if one gates the system on a time window starting 10 ps after the pump pulse, this system can consequently be regarded as a genuine transient topological insulator, with an extension in space (z_{dep} = 10 nm) and in time (Δt = 50 ps) which is interesting for potential ultrafast device applications.

5.3.4 Conclusion

In conclusion, I showed that the dynamics of the Dirac cone can be widely enhanced by the presence of subsurface band bending. Due to the carrier exchange between the Dirac cone and the bulk states, this situation leads to an extremely

long recombination time for more than 50 ps and a strongly out of equilibrium state of about 0.1 eV. A genuine transient 3D TI can be created, with no excess carriers in the conduction band after 10 ps, which can find interesting technological applications.

All these properties cannot be found in a conventional metal and open new perspectives for the transmission of current and information.

Chapter 6

Metal-insulator coexistence at the Mott transition in $(V_xCr_{1-x})_2O_3$

6.1 Introduction: microscopic domains in $(V_xCr_{1-x})_2O_3$

Over the last years, a lot of experimental and theoretical effort has been devoted to exploring microscopic inhomogeneities in many phenomena taking place in transition metal oxides (TMOs), such as metal-insulator transitions [97], colossal magnetoresistance [98] and high temperature superconductivity [99]. TMOs are often characterized by complicated phase diagrams [100]; phase coexistence occurs when different physical interactions, such as spin, charge and lattice, are active between two competing phases, and its understanding can lead to significant advances in our knowledge of the underlying physics.

Vanadium sesquioxide (V_2O_3) is one of the most widely studied TMOs. In particular, Cr-doped $(V_xCr_{1-x})_2O_3$ undergoes a metal-insulator transition as a function of temperature or pressure which is a prototype Mott transition (see chapter 3). Since this metal-insulator transition is of the first order, it should present the coexistence of metallic and insulating domains and hence exhibit large related electronic inhomogeneities.

In a recent previous study, the inhomogeneities in this phase transition were explored with scanning photoelectron microscopy (SPEM) at low photon energy (27

eV) and with a spatial resolution of about 1 μm [46]. It was found that the PM-PI transition in $(V_{0.989}Cr_{0.011})_2O_3$ is not homogeneous, presenting a coexistence of metallic and insulating regions, as it can be seen in figure 6.1. By comparing these photoemission microscopy results with data obtained on the same compound using other techniques with different characteristic probing lengths (such as X-ray diffraction and optical spectroscopy), and thanks also to precise LDA+DMFT calculations, it was possible to correctly interpret the bad metallic behaviour of the spatially averaging optical response of the x = 0.011 compound.

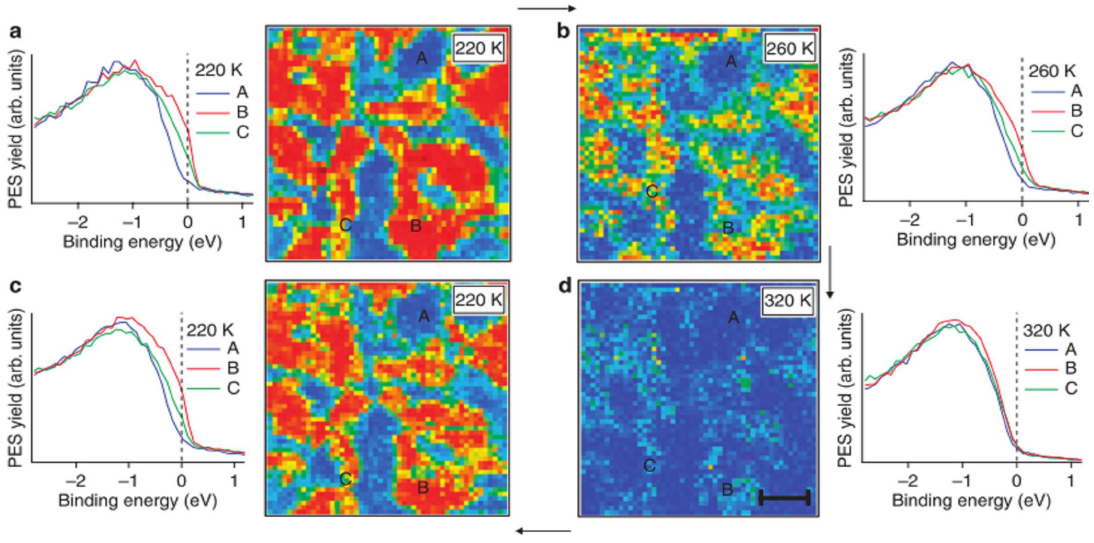

FIGURE 6.1: *Microscopic domains at the Mott transition in* $(V_{0.989}Cr_{0.011})_2O_3$ *as detected with SPEM at a photon energy of 27 eV in Ref. [46]*

This work clearly showed the importance of exploring the phase diagram of the this compound both on a macroscopic and on a microscopic scale. However, it also shows the difficulty of comparing the results obtained with different experimental methods: photoelectron spectroscopy with hν = 27 eV is very surface sensitive, due the low electron mean free path at this energy, while optical spectroscopy remains a bulk sensitive technique. In fact, in ref. [46] all the photoemission spectra taken from metallic domains do not detect any coherent QP peak, because the intensity of the QP peak in V_2O_3 systems is well affected by surface effects, as already explained in chapter 3 (3.2.2). Overall, these considerations call for a step further in this kind of studies, in particular for photoemission microscopy

performed in a more bulk sensitivity fashion .

As already explained in chapter 4, for this thesis work I used a soft X-ray Scanning PhotoElectron Microscope (SPEM) operating at a photon energy of 400 eV, giving a higher value of the photoelectron mean free path and hence increased bulk sensitivity. Furthermore, the spatial resolution with this microscope is also considerably better (150 nm), which makes it possible to better detect and analyse the metallic domains. In this way, one can address many other questions, like for exemple: can one detect a QP peak in the metallic domains thanks to the improved experimental conditions? is the QP intensity the same than in the undoped compound? and for what temperatures? These questions will be the main topics of this chapter. First, I will explain the analysis of the scanning images which allows us to identify the contrast between the metallic and the insulating regions. Then I will present and discuss the photoemission microscopy results on the $(V_{0.989}Cr_{0.011})_2O_3$ compound. And finally I will present the photoemission results on undoped V_2O_3 and the comparison between the PM phases in the two compounds.

6.2 Analysis of the scanning photoemission images

In this section I will explain how we can determine the contrast between metallic and insulating domains in scanning photoemission images [101]. As I explained in chapter 4 (4.4.3.3), the spectroscopic signal in the SPEM setup is contained in 48 channels on the detector; the energy window and the separation between channels depend on the pass energy of the analyzer. During my experiment I used an analyzer pass energy of 10 eV, which corresponds to a 2 eV energy window on the detector. However, two contributions to the photoemission intensity are measured by the analyzer: the first one is due to surface topography, particularly to the slope and the height of various surface features with respect to a perfectly flat surface; and the second one is the intrinsic photoemission intensity from the PM or PI phase. In order to determine the real contrast between the PM-PI

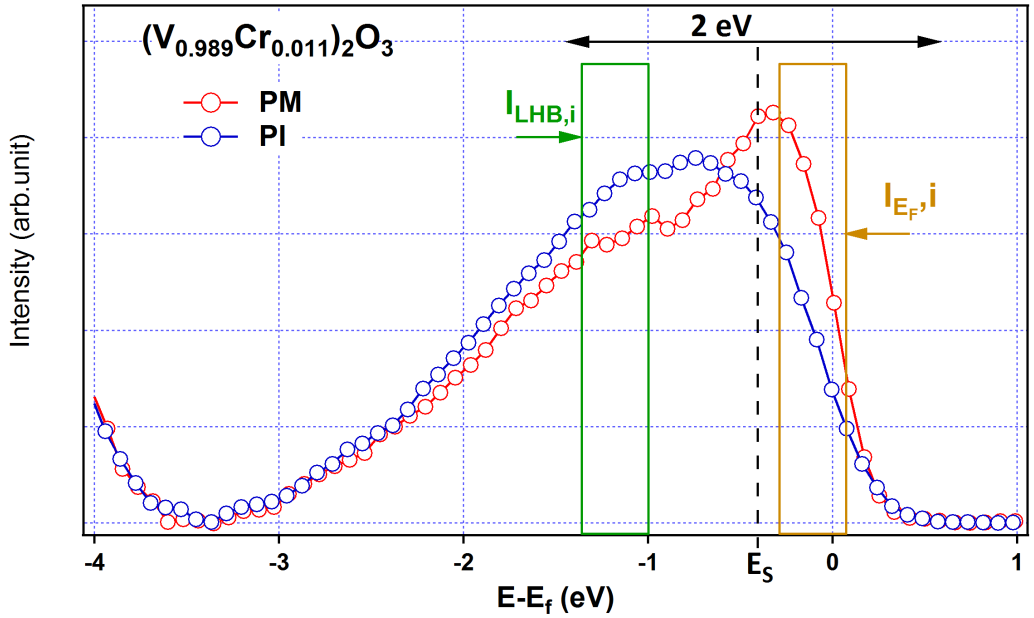

FIGURE 6.2: *Two photoemission spectra explain the difference between the PM and PI phases.*

phases one must first determine and remove topography effects. For each image we set the analyser to an energy E_S near the Fermi level E_F (see figure 6.2: after background suppression by shirley method); since the detected energy window is 2 eV wide, this allows the detection of a photoemission signal going from the gap to the lower Hubbard band (LHB), covering more than 1.2 eV of the V3d band. Near E_F, the photoemission intensity contains the intrinsic contrast between the PM and PI phases, but also topographic effects. The same is also in the LHB at 1.2 eV from E_F. We can write the intensity near E_F for each i phase, (i = PM,PI) as [102]:

$$I_{E_F,i} = I_i * I_{tpg}$$

where I_i and I_{tpg} are respectively the intrinsic intensity and the topography contribution in a specific energy range near E_F, selected by a specific number of channels (yellow window in figure 6.2). While the intensity of LHB at 1.2 eV for each phase i is:

$$I_{LHB,i} = I_{1.2eV,i} * I_{tpg}$$

where $I_{1.2eV,i}$ is the intrinsic intensity corresponds to LHB at 1.2 eV for the same number of detector channels used for the window near E_F (green part in figure 6.2)

The ratio $I_{E_F,i}/I_{LHB,i}$ will then remove the topography and enhance at the same time the genuine metal-insulator contrast in 2D "ratio" images. In particular, since the intensity within the yellow window is maximum for the PM phase and nearly absent or absent in the PI phase, in 2D ratio images the PM phase will correspond to high ratio values, and the PI phase to small ratio values.

6.3 SPEM on $(V_{0.989}Cr_{0.011})_2O_3$

6.3.1 Evidence and origin of phase coexistence

As extensively discussed, microscopic lateral inhomogeneities can play a crucial role in the macroscopic physical properties of TMOs. It is nevertheless important to distinguish two different scenarios: the first one is when phase separation is caused by extrinsic effects, like chemical or structural inhomogeneities, or other kinds of material imperfections; the second one is when it is really due to the competition between different thermodynamic phases. In materials presenting metal-insulator transitions, the coexistence of both phases under the form of microscopic domains at the transition is intrinsic in origin; nevertheless, both intrinsic and extrinsic effects were found for instance in vanadium dioxide, where grain boundaries present in (VO_2) thin films were found to be nucleation centers for the transition [97]. For $(V_{0.989}Cr_{0.011})_2O_3$, a direct comparison between its two metal-insulator transitions (the PM-PI Mott transition, and the structural transition between the PM and the antiferromagnetic insulating phase) showed that structural defects in single crystals can guide the morphology of domains that are intrinsic in nature [103].

Indeed, real materials have many defects such as impurities, oxygen vacancies, twinning. ect, which can act as nucleation centers, or seeding centers, for the phase transition [104, 105]. The typical size of these defects can be at the nanoscale

or less: this can be orders of magnitude smaller than the lateral resolution of the SPEM used in our experiments (150 nm). Consequently, the smaller inhomogeities will not be detected by our experiment, and we will be able to visualize only the larger features seeding the development of the new phase. For instance, when cleaving a new sample, with our technique we are able to ascertain a homogeneous surface only within the limits of our spatial resolution: the presence of cleavage steps or other defects smaller than 100 nm will escape our detection but it may still play a role in affecting the microscopic evolution of the specimen during the phase transition [98].

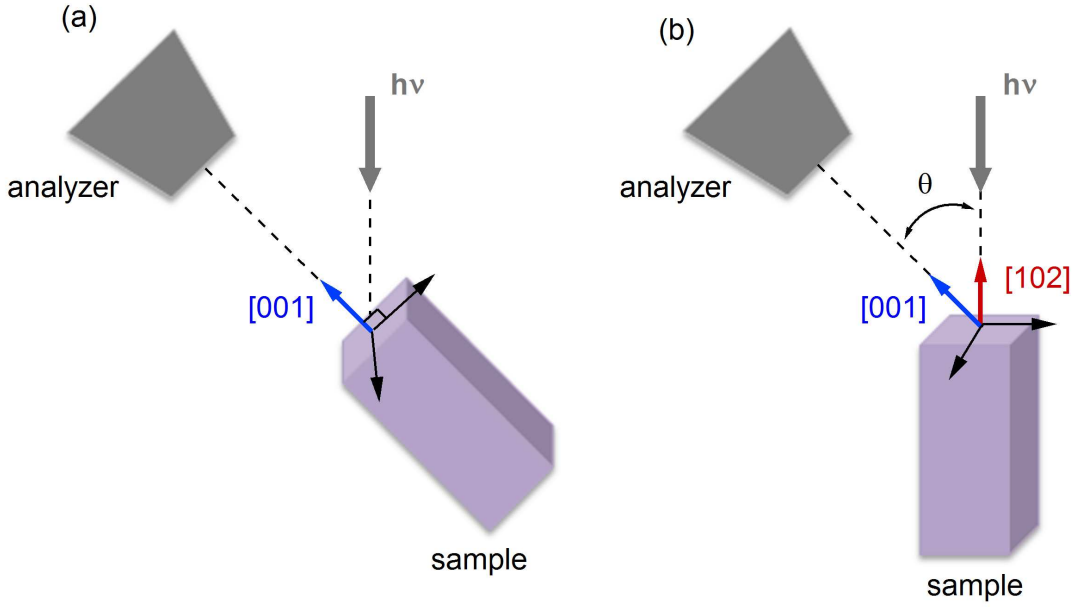

FIGURE 6.3: *a) Experimental geometry chosen to detect the photoelectrons at normal emission and along the [001] direction b) Experimental geometry chosen to detect the photoelectrons along the [001] direction but with emission angle* $\theta =$ *60 degrees*

A first crystal of $(V_{0.989}Cr_{0.011})_2O_3$ was carefully oriented and cleaved under ultrahigh vacuum condition ($< 10^{-10}$ mbar) along the [001] direction, where a more pronounced QP can be detected with respect to other orientations [58]. In order to enhance the bulk sensitivity of the measurement, the experimental geometry was chosen to detect the photoelectrons at normal emission, as shown in figure 6.3-a.

Figure 6.4-a (left) presents the surface morphology after the cleave, at a temperature T = 255 K, obtained by detecting photoelectrons at energy near E_F, where as the correspondent ratio image (right) presents a map of the coexistence of the metallic and insulating regions, showing a clear contrast between the two phases for example around the two points A (metallic) and B (insulating). This coexistence is confirmed by photoemission spectra taken from these two points, and shown in figure 6.4-c. By analyzing the correspondence between the surface morphology and the metallic regions, we can get a better understanding of the origin of the domains.

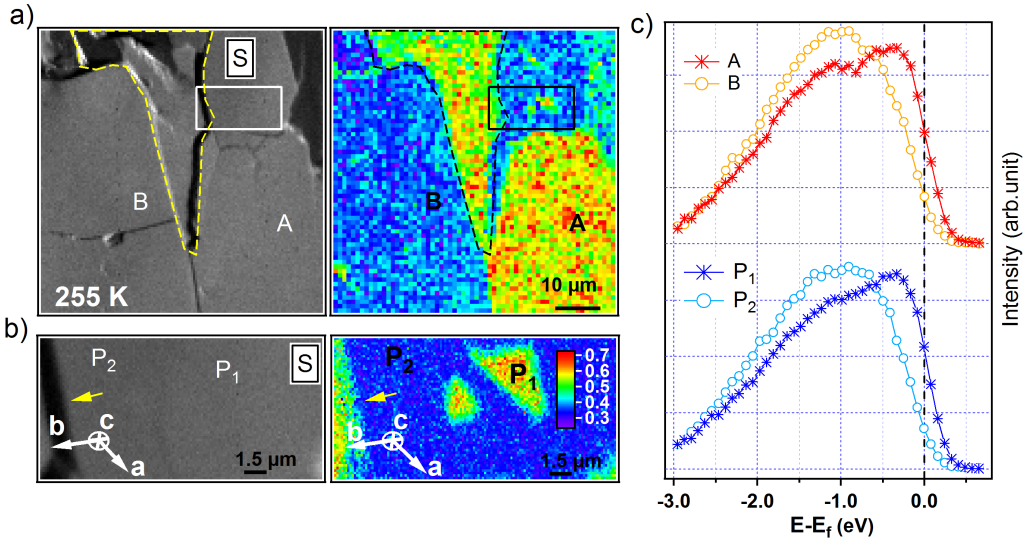

FIGURE 6.4: *a) (left) A surface morphology image taken at energy E_s corresponding to the V3p, and at temperature T = 255 K. The correspondent image showing the contrast between the PM and PI phases is on the right. b) The same for the S region. c) Photoemission spectra taken from the points A_1, A_2, P_1 and P_2*

Different kinds of regions can be easily identified from the morphology image (figure 6.4-a). For instance, the dashed contour line indicates a highly defected region, with clearly visible cleavage steps (left), and corresponds to a big metallic domain (right). But there are also flat regions, with no visible morphological defects, like for instance the one delimited by a solid rectangular contour line (S). As shown in more detail in figure 6.4-b (left), this region includes at its left a small part of the big cleavage step, indicated by yellow arrow, which was used as reference during the experiments to avoid and compensate lateral drifts

due for instance to sample temperature variations. Far away from this step, no defects are detected, at least with our spatial resolution, showing a flat surface region. As a consequence, S can be used as a good region to investigate intrinsic inhomogeneities in the metal-insulator transition. The correspondent contrast between the two PM-PI phases is shown on the right. A coexistence of insulating and metallic regions is well evident from the two points P_1 (metallic) and P_2 (insulating), and is confirmed also by the photoemission spectra shown in figure 6.4-c. The direction of the crystallographic axes for the sample is also shown in the images (a) and (b): it is important to notice that the shape of the metallic domains around P_1 seems to follow the crystallographic directions. This is easily understandable, since the system has to accomodate the difference in volume of the unit cell between the PI and PM phases. The results suggest the existence of possible nucleation centers with size smaller than our resolution, and the fact that the phase transition edge-line corresponds to the cristallographic axes may be related to atomic steps that we cannot detect. In the absence of larger defects, this seems to guide the intrinsic tendency to phase separation to create domains that reproduce the crystal symmetry. To summarize, the reason for the existence of domains at the Mott transition is intrinsic, and due to electronic effects; the points where the domains start growing are related to imperfections which act as nucleation centers; and the shape of the domains can be guided by the crystal structure. Within the limits of our spatial resolution, this region can be regarded as a convenient example of the evolution of this prototype Mott transition in the absence of sizable defects.

In order to further appreciate the important role played by crystal structure, let us consider another single crystal which was cleaved along the natural cleaving direction [102]. In this time the photoelectrons were collected at an emission angle of $\theta = 60°$ from the surface normal, as shown the figure 6.3-b, and the photoemission signal is consequently more surface sensitive.

The cleaved surface showed a nearly flat region without defects, see figure 6.5-a. By decreasing the temperature across the Mott transition, no domains were detected and the system was insulating down to 233 K: this is in contrast with the previous sample, where the metallic domains were observed already at 255 K in a

flat region without visible defects.

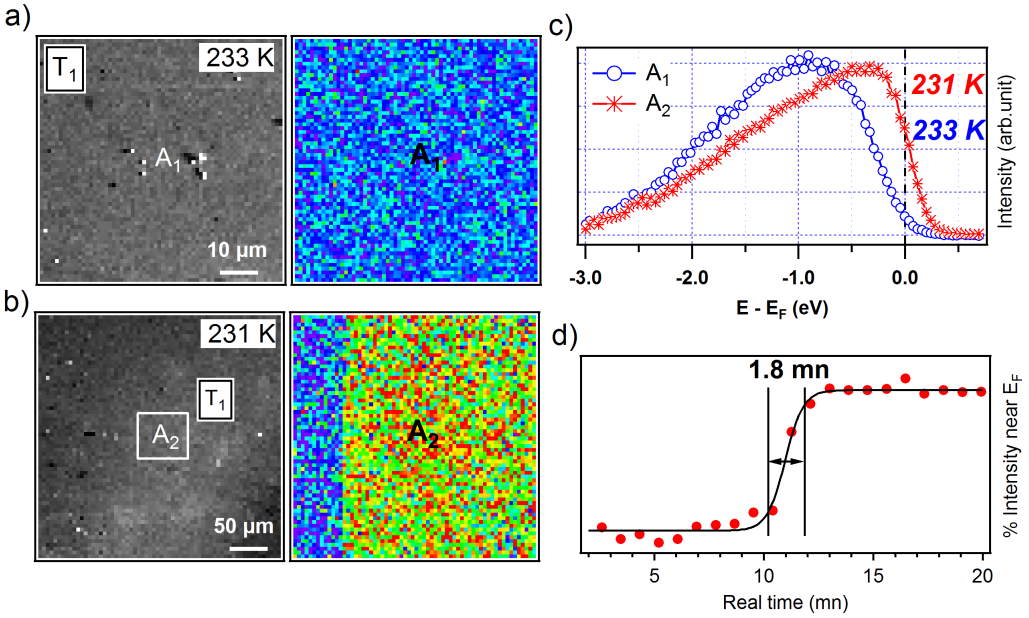

FIGURE 6.5: *a) left : T_1 a flat region after cleavage correponds to the surface (102). Right: the ratio image giving the contrast between the PM-PI phase. b) The same for more big region including the T_1 region c) Photoemission spectra taken from A_1 and A_2 points. d) The evolution of the PM-PI transition as a function of real time.*

After the temperature stabilized two degrees below (at around 231 K), the system became homogenously metallic, as evident from the comparison of the representative EDC's shown in the figure 6.5-c. The transition was in this case sudden, and we were not able to capture a coexistence of domains: actually the PM-PI ratio image shown in figure 6.5-b shows the evolution of the system in time, rather than in space: while scanning the image and as a function of the real time, the left part (blue) is insulating while the right part (red) became metallic. To characterize the velocity of this sudden transition we integrate all the pixels and we plot the contrast intensity between the PM and PI phases as a function of the real time required for scanning the image (figure 6.5-d). This transition takes place in less than 1.5 minutes and over a temperature range of less than two degrees. These results seem to indicate that for both surface orientations, [001] and [102], the nucleation centers for the transition are too small to be detected. But also that the (102) surface must be much more homogeneous, which leads to a transition

which is much more sudden and with domains probably too small for our spatial resolution.

6.3.2 A clear effect of cleavage steps

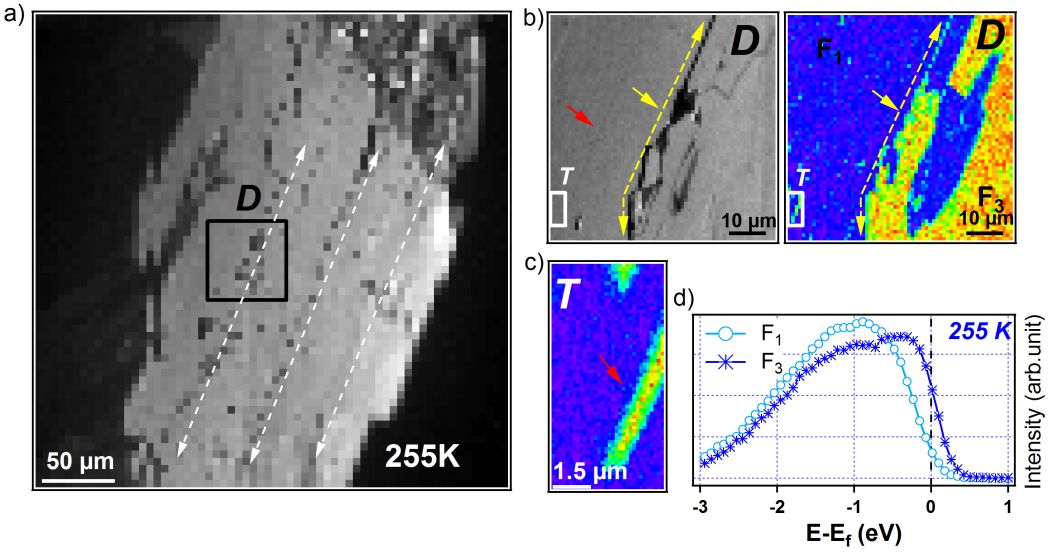

FIGURE 6.6: *a) The surface morphology shows clear cleavage steps along one direction (indicated by the white arrows). b) region D presents an image zooming on one step; on the right, a big metallic domain is present along and around the cleavage steps. c) region T shows the same behavior but with smaller domains. d) Two EDC spectra prove the evident coexistence of the PM and PI phases, corresponding to the* F_3 *(PM) and* F_1 *(PI) points in the region D.*

In order to appreciate the role of structural defects in the microscopic evolution of the phase transition, let us now consider another cleaved surface on the [001] oriented crystal. A large scale survey of the cleaved surface is presented with the topography image in figure 6.6-a. We focused our attention to the region indicated as D, and in figure 6.6-b one can see a zoomed image from this region (left) and the corresponding ratio image to appreciate the contrast between the PM and PI phases (right). Like for first cleave along the [001] direction presented in 6.3.1, the coexistence between the two phases is evident. But in this case the role of pre-existing structral defects in determining the shape of the domains is particularly evident. The shape of the domains presents a strong anisotropy in the surface, in particular it follows the position and direction of preexisting defects indicated by the yellow arrow, which correspond to the cleavage steps indicated

by different white dashed lines in figure 6.6-a. On an even smaller scale, a detailed view of a portion of the D region is presented in the zoomed image T (figure 6.6-c): in this case it is evident that the metallic domains have a markedly one-dimensional shape, and that they develop preferentially along the cleavage steps, as indicated by the red arrow. Overall, the morphology of the metallic domains during the transition mimics the morphology of preexisting structural defects. In the following I will take region D as an example of region with structural defects of known morphology.

6.3.3 Temperature evolution of the domains in regions without detected structural defects

Let us now examine how the morphology and the overall evolution of the domains during the PI-PM phase coexistence is affected by the crystal structure and by preexisting structural defects. As mentioned above, the flat region S obtained on the (001) surface shown in figure 6.4-b will be taken as an example of region without defects, at least not detectable with our experimental resolution (150 nm). In this paragraph I will present the evolution of the metallic domains when we decreased the temperature across the PM-PI transition.

Figure 6.7-a presents the evolution of the S region at three temperatures 255 K, 245 K and 235 K, while the evolution of the corresponding photoemission spectra taken from the two points P_1 and P_2, is shown in figure 6.7-b.

As temperature decreases to 245 K, a nearly homogenous metallic phase is found, where some contrast can still be seen around the first domains detected at 255 K which acted as seeding centers for the transition. By decreasing the temperature even more to 235 K we detect an evolution towards a more homogenous metallic phase. This behavior is confirmed by the photoemission spectra, that show how the point P_2 looks more and more like the point P_1 (figure 6.7-b).

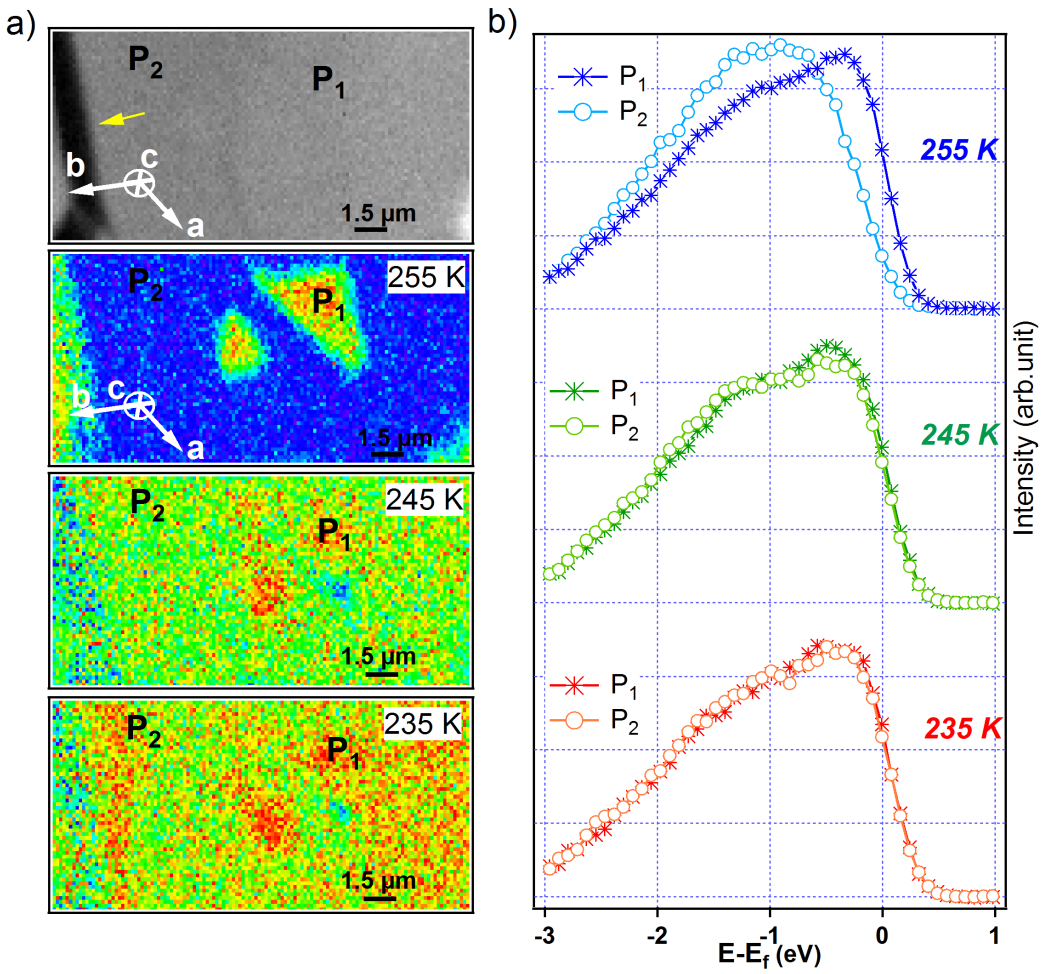

FIGURE 6.7: *a) Presents the evolution of the S region at three temperatures: 250 K, 245 K and 235 K. b) The evolution of the correspondent photoemission spectra taken from the two points* P_1 *and* P_2*.*

6.3.4 Temperature evolution of domains in regions with marked structural defects

Let us now turn our attention to a region with strong structural defects: figure 6.8-a presents the evolution of the D region at three temperatures, 255 K, 245 K and 200 K.

When we decreased the temperature across the PI-PM transition to 245 K, the insulating domains around the F_1 point at 255 K become strongly metallic, while the insulating domains around the F_2 point are less metallic.

In addition, even near the F_2 point the evolution of domains is not well homogeneous: the insulating domains near the cleavage step indicated by the yellow arrow

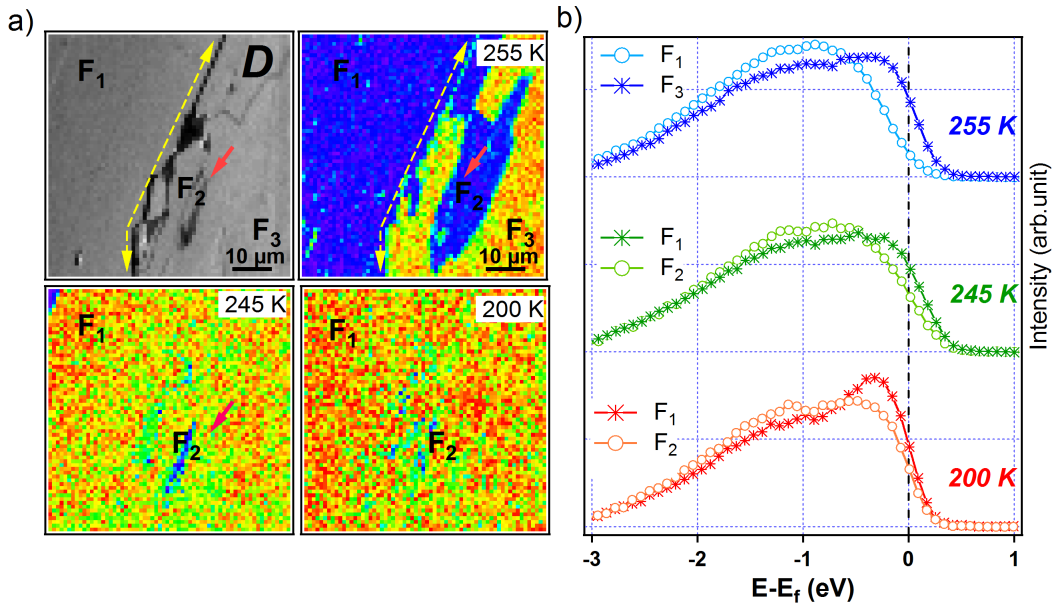

FIGURE 6.8: *a) Presents the evolution of the D region at three temperatures 255 K 245 K and 200 K. b) Photoemission spectra in the points* F_1*,* F_2 *and* F_3

turn easily into metallic with temperature; another type of defects, indicated by the red arrow, remain instead insulating at 245 K, and they seem to favor the insulating phase. This behavior is confirmed by the photoemission spectra in figure 6.8-a, where one can clearly compare the difference of the spectral weight near the Fermi level between the F_1 point and the F_2 point. This difference becomes clearer at low temperature 200 K, where a pronounced QP peak is detected in F_1 while in F_2 it is not. This type of defect presents a drawback to detect the good metallic behavior by using spatially averaging experiments: if for example we perform a standard soft X-ray photoemission spectroscopy experiment in the same conditions and on the same specimen, it will average on regions like F_1 and like F_2, giving a less pronounced QP peak in the EDC. This clearly shows the importance of the microscopic spatial resolution for the study of the PM-PI transition.

6.4 SPEM on undoped V_2O_3 and comparison of different PM phases

Soft-X-ray SPEM was also used to study the undoped compound V_2O_3. From low temperature at 180 K, corresponding to the PM phase, up to high temperature

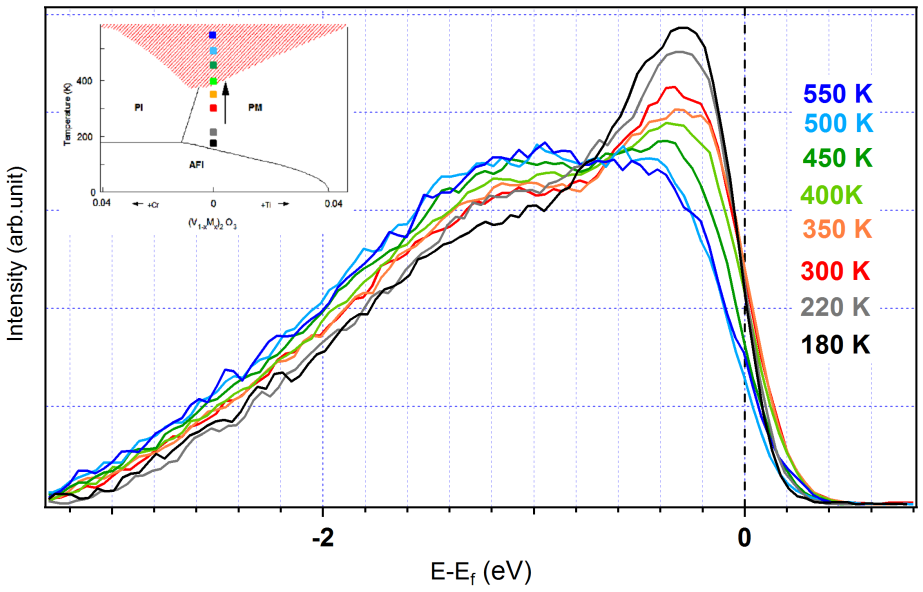

FIGURE 6.9: *Evolution of photoemission spectra in undoped* V_2O_3 *from the PM phase at low temperature (180K) to the cross over region at 550 K as indicated also in the inset with respect to the phase diagram*

at 550 K, corresponding to the cross over region, the cleaved surface was found to be laterally homogeneous: the PM phase was homogeneously metallic and the smooth transition towards the cross-over region showed no evidence of domains indicating phase separation. In parallel, to better understand the evolution of the electronic properties, in figure 6.9 I present the evolution of photoemission spectra in this temperature range, showing a clear evolution of the QP peak, which corresponds to transfer of spectral weight into the LHB. This behavior proves that V_2O_3 becomes more correlated when temperature is increased, and becomes a poor metal in the cross over region. The same behavior was observed also by optical measurements on the same compound, where the Drude peak characteristic of the metallic phase vanishes at high temperature [106].

Since we found also a pronounced QP peak in $(V_{0.989}Cr_{0.011})_2O_3$, it is possible to compare its spectral shape with undoped V_2O_3, i.e. to compare different points in the PM part of the thermodynamic phase diagram. Figure 6.10 presents the comparison of the two compounds at low temperature (200 K) and room temperature (300 K), respectively. It shows that the QP peak of $(V_{0.989}Cr_{0.011})_2O_3$ at low temperature is the same than V_2O_3 at room temperature, i.e. these two points in the phase diagram present the same degree of metallicity. At the same time, V_2O_3

at 200 K (see figure 6.9) presents a more pronounced QP than $(V_{0.989}Cr_{0.011})_2O_3$, proving that the undoped system remains less correlated at low temperature, and that the distance from the PM-PI phase transition line in the (x,T) phase diagram is more related to the degree of metallicity that the simple value of T.

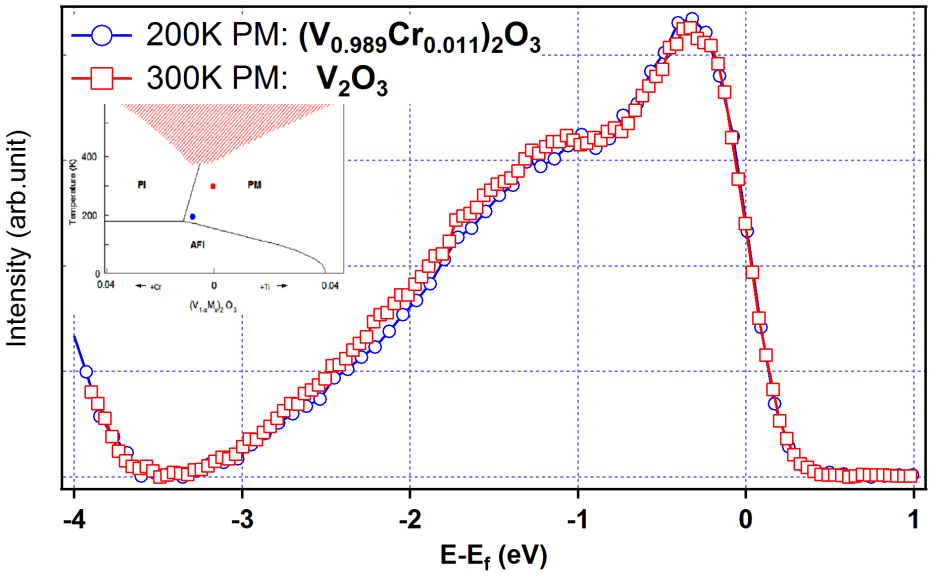

FIGURE 6.10: *Comparison of the photoemission spectra in* V_2O_3 *at 300 K and* $(V_{0.989}Cr_{0.011})_2O_3$ *at 200 K: these two points in the PM phase are indicated in the phase diagram in the inset by a blue circle (for the Cr-doped) and a red square (for the undoped).*

6.5 Conclusion

In conclusion, I showed the importance of enhancing the bulk sensitivity of SPEM to study a prototype strongly correlated compound like vanadium sesquioxide, in particular to look for the pronounced QP peak in the metallic domains. Using a Soft X-ray SPEM at 400 eV, I showed the evidence of coexisting domains in $(V_{0.989}Cr_{0.011})_2O_3$ across the PI-PM transition. The shape of the domains seems to be affected by the crystal structure: for surfaces with no detectable defects their shape can reproduce the main features of the crystalline structure; for surfaces with strong structural imperfections, like cleaving steps or other types of defects, these can act a nucleation centers or seeding centers for the transition

phase, and the shape and size of the domain tends to be affected by the morphology of the defects. Far away from these defects a pronounced QP was detected at low temperature in $(V_{0.989}Cr_{0.011})_2O_3$ showing the good metallic behavior of the PM phase in this system.

In parallel the PM phase of V_2O_3 was investigated as a function of the temperature. From low temperature up to the cross over region no domains or signs of phase separation were detected. The QP in this system vanishes when we increase the temperature, and the system becomes a bad metal in the cross over region, a behavior consistent with the most recent optical spectroscopy studies on this compound. Finally, a comparison of the QP peak for the PM phases at room temperature in the undoped compound and at low temperature in the Cr-doped compound, proves that these two points in the phase diagram present the same degree of correlation for the metallic phase.

Chapter 7

Conclusion

There were two goals is this thesis: the study of the ultrafast electron dynamics of surface (metal) and bulk (insulator) in the 3D topological insulators; and the study of the metal-insulator phase coexistence at the Mott transition. Two compounds were studied for this purpose, the 3D topological insulator Bi_2Te_3 and the prototype Mott material V_2O_3.

As we have seen, TR-ARPES is an ideal technique to study the ultrafast response of 3D topological insulators, since it gives a direct separation of the signal of the surface from that of the bulk. By applying this technique on n-type Bi_2Te_3 we have seen that the dynamics of the photoexcited Dirac cone is strongly affected by the scattering with the conduction band. In fact, both surface and bulk states contribute to the relaxation processes. Unlike normal semiconductors, topological insulators present metallic surface states. Furthermore these states show a long decay time after excitation. This situation can be strongly enhanced by a preexisting band bending in the subsurface region. A study performed on a p-type $Bi_{2.2}Te_3$ sample, with a downward bend bending of about 70 meV, showed that after the pump excitation excess hole carriers moved towards the bulk, while excited electrons in the conduction band moved towards the surface and remained confined in the surface states. After 10 ps there were no visible electrons in the bulk conduction band, while the chemical potential showed a maximum transient shift of 0.1 eV, a situation which can be extremely useful for optoelectronic applications. The absence of excited holes in the surface region resulted in a longer lifetime for the

photoexcited Dirac cone, more than 50 ps at low temperature (40K). These results indicate a general approach to effectively act on such a strong and persistent photoinduced transient Dirac fermion population, indicating many possible directions for its application, like for instance the possibility of exploiting the helical spin texture of the Dirac fermions. The electric field related to the band bending, along with the relative position of the Fermi level and of the Dirac point, are the main factors acting on the charge asymmetry and lifetime of the excited state: since and all these factors can be tailored at will using adjustable parameters, they can become powerful tools for the ultrafast control of Dirac fermions and for their technological application in devices.

The second technique based on photoelectron spectroscopy that was used in this thesis is scanning photoelectron microscopy (SPEM), employed to look for the microscopic domains at the Mott transition in Cr-doped V_2O_3. Thanks to the 150 nm spatial resolution attainable by this technique, an evidence of PM-PI phase coexistence was observed at the transition. Metallic domains have seen observed in regions without detected structural defects as well as in regions with marked defects. The domain morphology was found to be affected by the crystal structure, and in particular by cleavage steps. Different domain sizes were observed and they were crucially dependent on to the nature of the cleaved surface, strongly suggesting that they may also depend on small nucleation centers that cannot be detected with our spatial resolution. At low temperature, thanks to the use of soft X-ray photons (400 eV), SPEM was able to probe a pronounced QP peak in the metallic domains. In the undoped metallic compound no domains were observed, and its degree of metallicity at room temperature was the same than for the Cr doped specimen at low temperature. In order to further progress in this kind of studies, it appears critical to be able to detect smaller domains and to better study the quasiparticle peak in the metallic phase: for this purpose, one should try to improve the spatial resolution of the technique and increase the photon energy of the excitation source.

Bibliography

[1] K. v. Klitzing, G. Dorda, and M. Pepper. New method for high-accuracy determination of the fine-structure constant based on quantized Hall resistance. *Phys. Rev. Lett.*, (**45**):494–497, 1980. doi: 10.1103/PhysRevLett.45.494. URL http://link.aps.org/doi/10.1103/PhysRevLett.45.494.

[2] M. Z. Hasan and C. L. Kane. *Colloquium* : Topological insulators. *Rev. Mod. Phys.*, (**82**):3045–3067, 2010. doi: 10.1103/RevModPhys.82.3045. URL http://link.aps.org/doi/10.1103/RevModPhys.82.3045.

[3] Xiao-Liang Qi and Shou-Cheng Zhang. Topological insulators and superconductors. *Rev. Mod. Phys.*, (**83**):1057–1110, 2011. doi: 10.1103/RevModPhys.83.1057. URL http://link.aps.org/doi/10.1103/RevModPhys.83.1057.

[4] B. Andrei Bernevig, Taylor L. Hughes, and Shou-Cheng Zhang. Quantum spin hall effect and topological phase transition in HgTe quantum wells. *Science*, (**314**):1757–1761, 2006. doi: 10.1126/science.1133734. URL http://www.sciencemag.org/content/314/5806/1757.abstract.

[5] Markus Knig, Steffen Wiedmann, Christoph Brne, Andreas Roth, Hartmut Buhmann, Laurens W. Molenkamp, Xiao-Liang Qi, and Shou-Cheng Zhang. Quantum spin hall insulator state in HgTe quantum wells. *Science*, (**318**):766–770, 2007. doi: 10.1126/science.1148047. URL http://www.sciencemag.org/content/318/5851/766.abstract.

[6] Liang Fu and C. L. Kane. Topological insulators with inversion symmetry. *Phys. Rev. B*, (**76**):045302, 2007. doi: 10.1103/PhysRevB.76.045302. URL http://link.aps.org/doi/10.1103/PhysRevB.76.045302.

[7] Haijun Zhang, Chao-Xing Liu, Xiao-Liang Qi, Xi Dai, Zhong Fang, and Shou-Cheng Zhang. Topological insulators in Bi_2Se_3, Bi_2Te_3 and Sb_2Te_3 with a single Dirac cone on the surface. *Nature Physics*, (**5**):438–442, 2009. doi: 10.1038/nphys1270. URL http://www.nature.com/doifinder/10.1038/nphys1270.

[8] D Hsieh, Y Xia, D Qian, L Wray, J H Dil, F Meier, J Osterwalder, L Patthey, J G Checkelsky, N P Ong, a V Fedorov, H Lin, a Bansil, D Grauer, Y S Hor, R J Cava, and M Z Hasan. A tunable topological insulator in the spin helical Dirac transport regime. *Nature*, (**460**):1101–1105, 2009. doi: 10.1038/nature08234. URL http://www.nature.com/nature/journal/v460/n7259/abs/nature08234.html.

[9] Y. L. Chen, J. G. Analytis, J.-H. Chu, Z. K. Liu, S.-K. Mo, X. L. Qi, H. J. Zhang, D. H. Lu, X. Dai, Z. Fang, S. C. Zhang, I. R. Fisher, Z. Hussain, and Z.-X. Shen. Experimental realization of a three-dimensional topological insulator, Bi_2Te_3. *Science*, (**325**):178–181, 2009. doi: 10.1126/science.1173034. URL http://www.sciencemag.org/content/325/5937/178.abstract.

[10] Y. Xia, D. Qian, D. Hsieh, L. Wray, a. Pal, H. Lin, a. Bansil, D. Grauer, Y. S. Hor, R. J. Cava, and M. Z. Hasan. Observation of a large-gap topological-insulator class with a single Dirac cone on the surface. *Nature Physics*, (**5**):398–402, 2009. doi: 10.1038/nphys1274. URL http://www.nature.com/doifinder/10.1038/nphys1274.

[11] Joel E Moore. The birth of topological insulators. *Nature*, (**464**):194–8, 2010. doi: 10.1038/nature08916. URL http://www.nature.com/nature/journal/v464/n7286/abs/nature08916.html.

[12] Shuichi Murakami. Phase transition between the quantum spin Hall and insulator phases in 3D: emergence of a topological gapless phase. *New Journal of Physics*, (**9**):356, 2007. URL http://stacks.iop.org/1367-2630/9/i=9/a=356.

[13] Xiao-Liang Qi and Shou-Cheng Zhang. The quantum spin Hall effect and topological insulators. *Physics Today*, (**63**):33–38, 2010. doi: 10.1063/1.3293411. URL http://www.physicstoday.org/resource/1/phtoad/v63/i1/p33_s1.

[14] C. L. Kane and E. J. Mele. Z_2 topological order and the quantum spin Hall effect. *Phys. Rev. Lett.*, (**95**):146802, 2005. doi: 10.1103/PhysRevLett.95.146802. URL http://link.aps.org/doi/10.1103/PhysRevLett.95.146802.

[15] Rahul Roy. Z_2 classification of quantum spin hall systems: An approach using time-reversal invariance. *Phys. Rev. B*, (**79**):195321, 2009. doi: 10.1103/PhysRevB.79.195321. URL http://link.aps.org/doi/10.1103/PhysRevB.79.195321.

[16] Anders Strom. Interactions on the edge of a quantum spin Hall insulator. *Thesis*, page 12, 2011. URL http://physics.gu.se/~tfkhj/Lic_Thesis_AS.pdf.

[17] J. E. Moore and L. Balents. Topological invariants of time-reversal-invariant band structures. *Phys. Rev. B*, (**75**):121306, 2007. doi: 10.1103/PhysRevB.75.121306. URL http://link.aps.org/doi/10.1103/PhysRevB.75.121306.

[18] A. H. Castro Neto, F. Guinea, N. M. R. Peres, K. S. Novoselov, and A. K. Geim. The electronic properties of graphene. *Rev. Mod. Phys.*, (**81**):109–162, 2009. doi: 10.1103/RevModPhys.81.109. URL http://link.aps.org/doi/10.1103/RevModPhys.81.109.

[19] Tong Zhang, Peng Cheng, Xi Chen, Jin-Feng Jia, Xucun Ma, Ke He, Lili Wang, Haijun Zhang, Xi Dai, Zhong Fang, Xincheng Xie, and Qi-Kun Xue. Experimental demonstration of topological surface states protected by time-reversal symmetry. *Phys. Rev. Lett.*, (**103**):266803, 2009. doi: 10.1103/PhysRevLett.103.266803. URL http://link.aps.org/doi/10.1103/PhysRevLett.103.266803.

[20] Zhanybek Alpichshev, J. G. Analytis, J.-H. Chu, I. R. Fisher, Y. L. Chen, Z. X. Shen, A. Fang, and A. Kapitulnik. STM imaging of electronic waves on the surface of Bi_2Te_3: Topologically protected surface states and hexagonal warping effects. *Phys. Rev. Lett.*, (**104**):016401, 2010. doi: 10.1103/PhysRevLett.104.016401. URL http://link.aps.org/doi/10.1103/PhysRevLett.104.016401.

[21] C. Julian Chen. Introduction to scanning tunneling microscopy. *Oxford University Press*, 1993. URL http://www.columbia.edu/~jcc2161/documents/STM_2ed.pdf.

[22] Seo et al. Transmission of topological surface states through surface barriers. *Nature*, (**466**):343346, 2010. URL http://dx.doi.org/10.1038/nature09189.

[23] Masatoshi Imada, Atsushi Fujimori, and Yoshinori Tokura. Metal-insulator transitions. *Rev. Mod. Phys.*, (**70**):1039–1263, 1998. doi: 10.1103/RevModPhys.70.1039. URL http://link.aps.org/doi/10.1103/RevModPhys.70.1039.

[24] J H de Boer and E J W Verwey. Semi-conductors with partially and with completely filled 3D-lattice bands. *Proceedings of the Physical Society*, (**49**): 59, 1937. URL http://stacks.iop.org/0959-5309/49/i=4S/a=307.

[25] N F Mott. The basis of the electron theory of metals, with special reference to the transition metals. *Proceedings of the Physical Society. Section A*, (**62**): 416, 1949. URL http://stacks.iop.org/0370-1298/62/i=7/a=303.

[26] N. F. Mott. Metal-insulator transition. *Rev. Mod. Phys.*, (**40**):677–683, 1968. doi: 10.1103/RevModPhys.40.677. URL http://link.aps.org/doi/10.1103/RevModPhys.40.677.

[27] J. Hubbard. Electron correlations in narrow energy bands. *Proc. R. Soc. Lond. A*, (**276**):238–257, 1963. doi: 10.1098/rspa.1963.0204. URL http://rspa.royalsocietypublishing.org/content/276/1365/238.abstract.

[28] J. Hubbard. Electron correlations in narrow energy bands. II. the degenerate band case. *Proc. R. Soc. Lond. A*, (**277**):237–259, 1964. doi: 10.1098/rspa.1964.0019. URL http://rspa.royalsocietypublishing.org/content/277/1369/237.abstract.

[29] J. Hubbard. Electron correlations in narrow energy bands. III. an improved solution. *Proc. R. Soc. Lond. A*, (**281**):401–419, 1964. doi: 10.1098/rspa.1964.0190. URL http://rspa.royalsocietypublishing.org/content/281/1386/401.abstract.

[30] Elliott H. Lieb and F. Y. Wu. Absence of mott transition in an exact solution of the short-range, one-band model in one dimension. *Phys. Rev. Lett.*, (**20**):1445–1448, 1968. doi: 10.1103/PhysRevLett.20.1445. URL http://link.aps.org/doi/10.1103/PhysRevLett.20.1445.

[31] Martin C. Gutzwiller. Correlation of electrons in a narrow s band. *Phys. Rev.*, (**137**):A1726–A1735, 1965. doi: 10.1103/PhysRev.137.A1726. URL http://link.aps.org/doi/10.1103/PhysRev.137.A1726.

[32] Martin C. Gutzwiller. Effect of correlation on the ferromagnetism of transition metals. *Phys. Rev.*, (**134**):A923–A941, 1964. doi: 10.1103/PhysRev.134.A923. URL http://link.aps.org/doi/10.1103/PhysRev.134.A923.

[33] Antoine Georges, Gabriel Kotliar, Werner Krauth, and Marcelo J. Rozenberg. Dynamical mean-field theory of strongly correlated fermion systems and the limit of infinite dimensions. *Rev. Mod. Phys.*, (**68**):13–125, 1996. doi: 10.1103/RevModPhys.68.13. URL http://link.aps.org/doi/10.1103/RevModPhys.68.13.

[34] Walter Metzner and Dieter Vollhardt. Correlated lattice fermions in d= ∞ dimensions. *Phys. Rev. Lett.*, (**62**):324–327, 1989. doi: 10.1103/PhysRevLett.62.324. URL http://link.aps.org/doi/10.1103/PhysRevLett.62.324.

[35] Gabriel Kotliar and Dieter Vollhardt. Strongly correlated materials: Insights from dynamical mean-field theory. *Physics Today*, (**57**):53–59, 2004.

doi: 10.1063/1.1712502. URL http://www.physicstoday.org/resource/1/phtoad/v57/i3/p53_s1.

[36] Th. Pruschke, M. Jarrell, and J.K. Freericks. Anomalous normal-state properties of high-T_c superconductors: intrinsic properties of strongly correlated electron systems. *Advances in Physics*, (**44**):187–210, 1995. doi: 10.1080/00018739500101526. URL http://www.tandfonline.com/doi/abs/10.1080/00018739500101526.

[37] M. J. Rozenberg, G. Kotliar, H. Kajueter, G. A. Thomas, D. H. Rapkine, J. M. Honig, and P. Metcalf. Optical conductivity in Mott-Hubbard systems. *Phys. Rev. Lett.*, (**75**):105–108, 1995. doi: 10.1103/PhysRevLett.75.105. URL http://link.aps.org/doi/10.1103/PhysRevLett.75.105.

[38] W. Kohn and L. J. Sham. Self-consistent equations including exchange and correlation effects. *Phys. Rev.*, (**140**):A1133–A1138, 1965. doi: 10.1103/PhysRev.140.A1133. URL http://link.aps.org/doi/10.1103/PhysRev.140.A1133.

[39] A. I. Poteryaev V. I. Anisimov. First-principles calculations of the electronic structure and spectra of strongly correlated systems: Dynamical mean-field theory. *Cond Matter. arXiv:cond-mat/9704231v1*, 1997. doi: 10.1088/0953-8984/9/35/010. URL http://arxiv.org/abs/cond-mat/9704231.

[40] A. I. Lichtenstein and M. I. Katsnelson. Ab initio calculations of quasi-particle band structure in correlated systems: LDA++ approach. *Phys. Rev. B*, (**57**):6884–6895, 1998. doi: 10.1103/PhysRevB.57.6884. URL http://link.aps.org/doi/10.1103/PhysRevB.57.6884.

[41] D. B. McWhan and J. P. Remeika. Metal-insulator transition in $(V_{1-x}Cr_x)_2O_3$. *Phys. Rev. B*, (**2**):3734–3750, 1970. doi: 10.1103/PhysRevB.2.3734. URL http://link.aps.org/doi/10.1103/PhysRevB.2.3734.

[42] D. B. McWhan, A. Menth, J. P. Remeika, W. F. Brinkman, and T. M. Rice. Metal-insulator transitions in pure and doped V_2O_3. *Phys. Rev.*

B, (**7**):1920–1931, Mar 1973. doi: 10.1103/PhysRevB.7.1920. URL http://link.aps.org/doi/10.1103/PhysRevB.7.1920.

[43] P. Limelette, A. Georges, D. Jrome, P. Wzietek, P. Metcalf, and J. M. Honig. Universality and critical behavior at the mott transition. *Science*, (**302**):89–92, 2003. doi: 10.1126/science.1088386. URL http://www.sciencemag.org/content/302/5642/89.abstract.

[44] P.D. Dernier. The crystal structure of V_2O_3 and $(V_{0.962}Cr_{0.0382})_2O_3$ near the metal-insulator transition. *Journal of Physics and Chemistry of Solids*, (**31**):2569 – 2575, 1970. doi: 10.1016/0022-3697(70)90076-4. URL http://www.sciencedirect.com/science/article/pii/0022369770900764.

[45] G. Keller, K. Held, V. Eyert, D. Vollhardt, and V. I. Anisimov. Electronic structure of paramagnetic V_2O_3: Strongly correlated metallic and Mott insulating phase. *Phys. Rev. B*, (**70**):205116, 2004. doi: 10.1103/PhysRevB.70.205116. URL http://link.aps.org/doi/10.1103/PhysRevB.70.205116.

[46] S Lupi, L Baldassarre, B Mansart, a Perucchi, a Barinov, P Dudin, E Papalazarou, F Rodolakis, J-P Rueff, J-P Itié, S Ravy, D Nicoletti, P Postorino, P Hansmann, N Parragh, a Toschi, T Saha-Dasgupta, O K Andersen, G Sangiovanni, K Held, and M Marsi. A microscopic view on the Mott transition in chromium-doped V_2O_3. *Nature communications*, (**1**):105, 2010. doi: 10.1038/ncomms1109. URL http://www.ncbi.nlm.nih.gov/pubmed/21045823.

[47] C. Castellani, C. R. Natoli, and J. Ranninger. Magnetic structure of V_2O_3 in the insulating phase. *Phys. Rev. B*, (**18**):4945–4966, 1978. doi: 10.1103/PhysRevB.18.4945. URL http://link.aps.org/doi/10.1103/PhysRevB.18.4945.

[48] C. Castellani, C. R. Natoli, and J. Ranninger. Insulating phase of V_2O_3: An attempt at a realistic calculation. *Phys. Rev. B*, (**18**):4967–5000, 1978. doi: 10.1103/PhysRevB.18.4967. URL http://link.aps.org/doi/10.1103/PhysRevB.18.4967.

[49] C. Castellani, C. R. Natoli, and J. Ranninger. Metal-insulator transition in pure and Cr-doped V_2O_3. *Phys. Rev. B*, (**18**):5001–5013, 1978. doi: 10.1103/PhysRevB.18.5001. URL http://link.aps.org/doi/10.1103/PhysRevB.18.5001.

[50] J.-H. Park, L. H. Tjeng, A. Tanaka, J. W. Allen, C. T. Chen, P. Metcalf, J. M. Honig, F. M. F. de Groot, and G. A. Sawatzky. Spin and orbital occupation and phase transitions in V_2O_3. *Phys. Rev. B*, (**61**):11506–11509, 2000. doi: 10.1103/PhysRevB.61.11506. URL http://link.aps.org/doi/10.1103/PhysRevB.61.11506.

[51] S. Yu. Ezhov, V. I. Anisimov, D. I. Khomskii, and G. A. Sawatzky. Orbital occupation, local spin, and exchange interactions in V_2O_3. *Phys. Rev. Lett.*, (**83**):4136–4139, 1999. doi: 10.1103/PhysRevLett.83.4136. URL http://link.aps.org/doi/10.1103/PhysRevLett.83.4136.

[52] K. Maiti, Priya Mahadevan, and D. D. Sarma. Evolution of spectral function in a doped Mott insulator: Surface vs bulk contributions. *Phys. Rev. Lett.*, (**80**):2885–2888, 1998. doi: 10.1103/PhysRevLett.80.2885. URL http://link.aps.org/doi/10.1103/PhysRevLett.80.2885.

[53] S.-K. Mo, J. D. Denlinger, H.-D. Kim, J.-H. Park, J. W. Allen, A. Sekiyama, A. Yamasaki, K. Kadono, S. Suga, Y. Saitoh, T. Muro, P. Metcalf, G. Keller, K. Held, V. Eyert, V. I. Anisimov, and D. Vollhardt. Prominent quasiparticle peak in the photoemission spectrum of the metallic phase of V_2O_3. *Phys. Rev. Lett.*, (**90**):186403, 2003. doi: 10.1103/PhysRevLett.90.186403. URL http://link.aps.org/doi/10.1103/PhysRevLett.90.186403.

[54] S.-K. Mo, H.-D. Kim, J. D. Denlinger, J. W. Allen, J.-H. Park, A. Sekiyama, A. Yamasaki, S. Suga, Y. Saitoh, T. Muro, and P. Metcalf. *Phys. Rev. B*, (**74**):165101, Oct 2006. doi: 10.1103/PhysRevB.74.165101. URL http://link.aps.org/doi/10.1103/PhysRevB.74.165101.

[55] K. Held, G. Keller, V. Eyert, D. Vollhardt, and V. I. Anisimov. Mott-hubbard metal-insulator transition in paramagnetic V_2O_3: An

LDA+DMFT(QMC) study. *Phys. Rev. Lett.*, (**86**):5345–5348, 2001. doi: 10.1103/PhysRevLett.86.5345. URL http://link.aps.org/doi/10.1103/PhysRevLett.86.5345.

[56] Alexander I. Poteryaev, Jan M. Tomczak, Silke Biermann, Antoine Georges, Alexander I. Lichtenstein, Alexey N. Rubtsov, Tanusri Saha-Dasgupta, and Ole K. Andersen. Enhanced crystal-field splitting and orbital-selective coherence induced by strong correlations in V_2O_3. *Phys. Rev. B*, (**76**):085127, 2007. doi: 10.1103/PhysRevB.76.085127. URL http://link.aps.org/doi/10.1103/PhysRevB.76.085127.

[57] H. Fujiwara, A. Sekiyama, S.-K. Mo, J. W. Allen, J. Yamaguchi, G. Funabashi, S. Imada, P. Metcalf, A. Higashiya, M. Yabashi, K. Tamasaku, T. Ishikawa, and S. Suga. Evidence for the constancy of U in the mott transition of V_2O_3. *Phys. Rev. B*, (**84**):075117, 2011. doi: 10.1103/PhysRevB.84.075117. URL http://link.aps.org/doi/10.1103/PhysRevB.84.075117.

[58] F. Rodolakis, B. Mansart, E. Papalazarou, S. Gorovikov, P. Vilmercati, L. Petaccia, A. Goldoni, J. P. Rueff, S. Lupi, P. Metcalf, and M. Marsi. Quasiparticles at the mott transition in V_2O_3: Wave vector dependence and surface attenuation. *Phys. Rev. Lett.*, (**102**):066805, 2009. doi: 10.1103/PhysRevLett.102.066805. URL http://link.aps.org/doi/10.1103/PhysRevLett.102.066805.

[59] *J. Physics Synopsis*, Feb . URL http://physics.aps.org/synopsis-for/10.1103/PhysRevLett.102.066805.

[60] Giovanni Borghi, Michele Fabrizio, and Erio Tosatti. Surface dead layer for quasiparticles near a mott transition. *Phys. Rev. Lett.*, (**102**):066806, 2009. doi: 10.1103/PhysRevLett.102.066806. URL http://link.aps.org/doi/10.1103/PhysRevLett.102.066806.

[61] Hertz.H. Ueber einen einfluss des ultravioletten lichtes auf die electrische entladung. *Ann.Phys.*, (**267**):983, 1887. doi: 10.1002/andp.

18872670827. URL http://onlinelibrary.wiley.com/doi/10.1002/andp.18872670827/abstract.

[62] Einstein.A. ber einen die erzeugung und verwandlung des lichtes betreffenden heuristischen gesichtspunkt. *Ann.Phys.*, (**322**):132, 1905. doi: 10.1002/andp.19053220607. URL http://onlinelibrary.wiley.com/doi/10.1002/andp.19053220607/abstract.

[63] J. E. Bowen Katari, V. L. Colvin, and A. P. Alivisatos. X-ray photoelectron spectroscopy of cdse nanocrystals with applications to studies of the nanocrystal surface. *The Journal of Physical Chemistry*, (**98**):4109–4117, 1994. doi: 10.1021/j100066a034. URL http://pubs.acs.org/doi/abs/10.1021/j100066a034.

[64] Andrea Damascelli. Probing the electronic structure of complex systems by arpes. *Physica Scripta*, (**T109**):61–74, 2004. URL http://stacks.iop.org/1402-4896/2004/i=T109/a=005.

[65] W S Lee, I M Vishik, D H Lu, and Z-X Shen. A brief update of angle-resolved photoemission spectroscopy on a correlated electron system. *Journal of Physics: Condensed Matter*, (**21**)(16):164217, 2009. URL http://stacks.iop.org/0953-8984/21/i=16/a=164217.

[66] Christopher L. Smallwood, Christopher Jozwiak, and Wentao Zhang.and Alessandra Lanzara. An ultrafast angle-resolved photoemission apparatus for measuring complex materials. *Review of Scientific Instruments*, (**83**):123904, 2012. doi: 10.1063/1.4772070. URL http://link.aip.org/link/?RSI/83/123904/1.

[67] S. Mathias, L. Miaja-Avila, M. M. Murnane, H. Kapteyn, M. Aeschlimann, and M. Bauer. Angle-resolved photoemission spectroscopy with a femtosecond high harmonic light source using a two-dimensional imaging electron analyzer. *Review of Scientific Instruments*, (**78**):083105, 2007. doi: 10.1063/1.2773783. URL http://link.aip.org/link/?RSI/78/083105/1.

[68] G. L. Dakovski, Y. Li, T. Durakiewicz, and G. Rodriguez. Tunable ultrafast extreme ultraviolet source for time- and angle-resolved photoemission spectroscopy. *Review of Scientific Instruments*, (**81**):073108, 2010. doi: 10.1063/1.3460267. URL http://link.aip.org/link/?RSI/81/073108/1.

[69] F. Schmitt, P. S. Kirchmann, U. Bovensiepen, R. G. Moore, L. Rettig, M. Krenz, J.-H. Chu, N. Ru, L. Perfetti, D. H. Lu, M. Wolf, I. R. Fisher, and Z.-X. Shen. Transient electronic structure and melting of a charge density wave in $TbTe_3$. *Science*, (**321**):1649–1652, 2008. doi: 10.1126/science.1160778. URL http://www.sciencemag.org/content/321/5896/1649.abstract.

[70] Majid Kazemian Abyaneh, Luca Gregoratti, Matteo Amati, Matteo Dalmiglio, and Maya Kiskinova. Scanning photoelectron microscopy: a powerful technique for probing micro and nano-structures. *e-Journal of Surface Science and Nanotechnology*, (**9**):158–162, 2011. URL https://www.jstage.jst.go.jp/article/ejssnt/9/0/9_0_158/_article.

[71] L. Casalis, W. Jark, M. Kiskinova, D. Lonza, P. Melpignano, D. Morris, R. Rosei, A. Savoia, A. Abrami, C. Fava, P. Furlan, R. Pugliese, D. Vivoda, G. Sandrin, F.-Q. Wei, S. Contarini, L. DeAngelis, C. Gariazzo, P. Nataletti, and G. R. Morrison. Esca microscopy beamline at elettra. *Review of Scientific Instruments*, (**66**):4870–4875, 1995. doi: 10.1063/1.1146167. URL http://link.aip.org/link/?RSI/66/4870/1.

[72] C. N. Berglund and W. E. Spicer. Photoemission studies of copper and silver: Theory. *Phys. Rev.*, (**136**):A1030–A1044, 1964. doi: 10.1103/PhysRev.136.A1030. URL http://link.aps.org/doi/10.1103/PhysRev.136.A1030.

[73] M. P. Seah and W. A. Dench. Quantitative electron spectroscopy of surfaces: A standard data base for electron inelastic mean free paths in solids. *Surf. Interface Anal.*, (**1**):2–11, 1979. doi: 10.1002/sia.740010103. URL http://onlinelibrary.wiley.com/doi/10.1002/sia.740010103/abstract.

[74] M. Lisowski, P.A. Loukakos, U. Bovensiepen, J. Sthler, C. Gahl, and M. Wolf. Ultra-fast dynamics of electron thermalization, cooling and transport effects in Ru(001). *Applied Physics A*, (**78**):165–176, 2004. doi: 10.1007/s00339-003-2301-7. URL http://dx.doi.org/10.1007/s00339-003-2301-7.

[75] J. Faure, J. Mauchain, E. Papalazarou, W. Yan, J. Pinon, M. Marsi, and L. Perfetti. Full characterization and optimization of a femtosecond ultraviolet laser source for time and angle-resolved photoemission on solid surfaces. *Review of Scientific Instruments*, (**83**):043109, 2012. doi: 10.1063/1.3700190. URL http://link.aip.org/link/?RSI/83/043109/1.

[76] E. Papalazarou, J. Faure, J. Mauchain, M. Marsi, A. Taleb-Ibrahimi, I. Reshetnyak, A. van Roekeghem, I. Timrov, N. Vast, B. Arnaud, and L. Perfetti. Coherent phonon coupling to individual bloch states in photoexcited Bismuth. *Phys. Rev. Lett.*, (**108**):256–808, 2012. doi: 10.1103/PhysRevLett.108.256808. URL http://link.aps.org/doi/10.1103/PhysRevLett.108.256808.

[77] A. Borsutzky, R. Brnger, Ch. Huang, and R. Wallenstein. Harmonic and sum-frequency generation of pulsed laser radiation in BBO, LBO, and KD*P. *Applied Physics B*, (**52**):55–62, 1991. doi: 10.1007/BF00405687. URL http://dx.doi.org/10.1007/BF00405687.

[78] Peter Siffalovic. *Femtosecond time-resolved photoelectron spectroscopy in the extreme ultraviolet region*. PhD thesis, Bielefeld University, 2002. URL http://pub.uni-bielefeld.de/publication/2304161?source_opus=367.

[79] I. Lovas, W. Santy, E. Spiller, R. Tibbetts, and J. Wilczynski. Design and assembly of a high resolution schwarzschild microscope for soft x rays. pages 90–99, 1982. doi: 10.1117/12.933138. URL http://dx.doi.org/10.1117/12.933138.

[80] Ren Hudec. Kirkpatrick-baez x-ray optics: a review. pages 807607–807607–14, 2011. doi: 10.1117/12.888268. URL http://dx.doi.org/10.1117/12.888268.

[81] Pavan Hosur. Circular photogalvanic effect on topological insulator surfaces: Berry-curvature-dependent response. *Phys. Rev. B*, (**83**):035309, Jan 2011. doi: 10.1103/PhysRevB.83.035309. URL http://link.aps.org/doi/10.1103/PhysRevB.83.035309.

[82] R. Valdés Aguilar, A. V. Stier, W. Liu, L. S. Bilbro, D. K. George, N. Bansal, L. Wu, J. Cerne, A. G. Markelz, S. Oh, and N. P. Armitage. Terahertz response and colossal kerr rotation from the surface states of the topological insulator Bi_2Se_3. *Phys. Rev. Lett.*, (**108**):087403, 2012. doi: 10.1103/PhysRevLett.108.087403. URL http://link.aps.org/doi/10.1103/PhysRevLett.108.087403.

[83] Alexander Q. Wu, Xianfan Xu, and Rama Venkatasubramanian. Ultrafast dynamics of photoexcited coherent phonon in Bi_2Te_3 thin films. *Applied Physics Letters*, (**92**):011108, 2008. doi: 10.1063/1.2829604. URL http://link.aip.org/link/APPLAB/v92/i1/p011108/s1&Agg=doi.

[84] D. Hsieh, F. Mahmood, J. W. McIver, D. R. Gardner, Y. S. Lee, and N. Gedik. Selective probing of photoinduced charge and spin dynamics in the bulk and surface of a topological insulator. *Phys. Rev. Lett.*, (**107**):077401, 2011. doi: 10.1103/PhysRevLett.107.077401. URL http://link.aps.org/doi/10.1103/PhysRevLett.107.077401.

[85] Jason N. Hancock, J. L. M. van Mechelen, Alexey B. Kuzmenko, Dirk van der Marel, Christoph Brüne, Elena G. Novik, Georgy V. Astakhov, Hartmut Buhmann, and Laurens W. Molenkamp. Surface state charge dynamics of a high-mobility three-dimensional topological insulator. *Phys. Rev. Lett.*, (**107**):136803, 2011. doi: 10.1103/PhysRevLett.107.136803. URL http://link.aps.org/doi/10.1103/PhysRevLett.107.136803.

[86] M. Hajlaoui et al. Time resolved ultrafast arpes for the study of topological insulators: The case of Bi_2Te_3. *Eur. Phys. J. Special Topics*, (**222**):1271–1275, 2013. doi: 10.1140/epjst/e2013-01921-1. URL http://epjst.epj.org/articles/epjst/abs/2013/11/epjst2225022/epjst2225022.html.

[87] M. Hajlaoui, E. Papalazarou, J. Mauchain, G. Lantz, N. Moisan, D. Boschetto, Z. Jiang, I. Miotkowski, Y. P. Chen, A. Taleb-Ibrahimi, L. Perfetti, and M. Marsi. Ultrafast surface carrier dynamics in the topological insulator Bi_2Te_3. *Nano Letters*, (**12**):3532–3536, 2012. doi: 10.1021/nl301035x. URL http://pubs.acs.org/doi/abs/10.1021/nl301035x.

[88] M. Hajlaoui, E. Papalazarou, J. Mauchain, L. Perfetti, A. Taleb-Ibrahimi, F. Navarin, M. Monteverde, P. Auban-Senzier, C. R. Pasquier, N. Moisan, D. Boschetto, M. Neupane, M. Z. Hasan, T. Durakiewicz, Z. Jiang, Y. Xu, I. Miotkowski, Y. P. Chen, S. Jia, H. W. Ji, R. J. Cava, and M. Marsi. Tuning a schottky barrier in a photoexcited topological insulator with transient dirac cone electron-hole asymmetry. *cond-mat, accepted on nature communication*, nov 2013. URL http://arxiv.org/abs/1311.6171.

[89] J. Sobota, S. Yang, J. Analytis, Y. Chen, I. Fisher, P. Kirchmann, and Z.-X. Shen. Ultrafast Optical Excitation of a Persistent Surface-State Population in the Topological Insulator Bi_2Se_3. *Physical Review Letters*, (**108**):1–5, 2012. doi: 10.1103/PhysRevLett.108.117403. URL http://link.aps.org/doi/10.1103/PhysRevLett.108.117403.

[90] Y. Wang, D. Hsieh, E. Sie, H. Steinberg, D. Gardner, Y. Lee, P. Jarillo-Herrero, and N. Gedik. Measurement of Intrinsic Dirac Fermion Cooling on the Surface of the Topological Insulator Bi_2Se_3 Using Time-Resolved and Angle-Resolved Photoemission Spectroscopy. *Physical Review Letters*, (**109**):1–5, 2012. doi: 10.1103/PhysRevLett.109.127401. URL http://link.aps.org/doi/10.1103/PhysRevLett.109.127401.

[91] A. Crepaldi, B. Ressel, F. Cilento, M. Zacchigna, C. Grazioli, H. Berger, Ph. Bugnon, K. Kern, M. Grioni, and F. Parmigiani. Ultrafast photodoping and effective fermi-dirac distribution of the dirac particles in Bi_2Se_3. *Phys.*

Rev. B, (**86**):205133, 2012. doi: 10.1103/PhysRevB.86.205133. URL http://link.aps.org/doi/10.1103/PhysRevB.86.205133.

[92] M. Marsi, L. Nahon, M.E. Couprie, D. Garzella, T. Hara, R. Bakker, M. Billardon, A. Delboulb, G. Indlekofer, and A. Taleb-Ibrahimi. Surface photovoltage in semiconductors under pulsed optical excitation, and its relevance to synchrotron radiation spectroscopy. *Journal of Electron Spectroscopy and Related Phenomena*, (**94**):149 – 157, 1998. doi: 10.1016/S0368-2048(98)00142-X. URL http://www.sciencedirect.com/science/article/pii/S036820489800142X.

[93] N. J. Halas and J. Bokor. Surface recombination on the Si(111) 2 x 1 surface. *Phys. Rev. Lett.*, (**62**):1679–1682, 1989. doi: 10.1103/PhysRevLett.62.1679. URL http://link.aps.org/doi/10.1103/PhysRevLett.62.1679.

[94] Zhen Zhang and John T. Yates. Band bending in semiconductors: Chemical and physical consequences at surfaces and interfaces. *Chemical Reviews*, (**112**):5520–5551, 2012. doi: 10.1021/cr3000626. URL http://pubs.acs.org/doi/abs/10.1021/cr3000626.

[95] S. Chevtchenko, X. Ni, Q. Fan, A. A. Baski, and H. Morkoç. Surface band bending of a-plane gan studied by scanning kelvin probe microscopy. *Applied Physics Letters*, (**88**):122104, 2006. doi: 10.1063/1.2188589. URL http://link.aip.org/link/?APL/88/122104/1.

[96] Z.-H. Pan, a. Fedorov, D. Gardner, Y. Lee, S. Chu, and T. Valla. Measurement of an Exceptionally Weak Electron-Phonon Coupling on the Surface of the Topological Insulator Bi_2Se_3 Using Angle-Resolved Photoemission Spectroscopy. *Physical Review Letters*, (**108**)(18):1–5, 2012. doi: 10.1103/PhysRevLett.108.187001. URL http://link.aps.org/doi/10.1103/PhysRevLett.108.187001.

[97] A. Frenzel, M. M. Qazilbash, M. Brehm, Byung-Gyu Chae, Bong-Jun Kim, Hyun-Tak Kim, A. V. Balatsky, F. Keilmann, and D. N. Basov. Inhomogeneous electronic state near the insulator-to-metal transition in the correlated

oxide VO_2. *Phys. Rev. B*, (**80**):115115, 2009. doi: 10.1103/PhysRevB.80.115115. URL http://link.aps.org/doi/10.1103/PhysRevB.80.115115.

[98] M. Fth, S. Freisem, A. A. Menovsky, Y. Tomioka, J. Aarts, and J. A. Mydosh. Spatially inhomogeneous metal-insulator transition in doped manganites. *Science*, (**285**):1540–1542, 1999. doi: 10.1126/science.285.5433.1540. URL http://www.sciencemag.org/content/285/5433/1540.abstract.

[99] S. H. Pan et al. Microscopic electronic inhomogeneity in the high-tc superconductor $Bi_2Sr_2CaCuO_{8+x}$. *Nature*, (**413**):282–285, 2001. doi: 10.1038/35095012. URL http://www.nature.com/nature/journal/v413/n6853/pdf/413282a0.pdf.

[100] Elbio Dagotto. Complexity in strongly correlated electronic systems. *Science (New York, N.Y.)*, (**309**):257–62, 2005. doi: 10.1126/science.1107559. URL http://www.sciencemag.org/content/309/5732/257.short.

[101] D. D. Sarma, Dinesh Topwal, U. Manju, S. R. Krishnakumar, M. Bertolo, S. La Rosa, G. Cautero, T. Y. Koo, P. A. Sharma, S.-W. Cheong, and A. Fujimori. Direct observation of large electronic domains with memory effect in doped manganites. *Phys. Rev. Lett.*, (**93**):097202, 2004. doi: 10.1103/PhysRevLett.93.097202. URL http://link.aps.org/doi/10.1103/PhysRevLett.93.097202.

[102] M Marsi, L Casalis, L Gregoratti, S Gnther, A Kolmakov, J Kovac, D Lonza, and M Kiskinova. ESCA microscopy at elettra: what it is like to perform spectromicroscopy experiments on a third generation synchrotron radiation source. *Journal of Electron Spectroscopy and Related Phenomena*, (**84**):73 – 83, 1997. URL http://www.sciencedirect.com/science/article/pii/S0368204897000108.

[103] B. Mansart, A. Barinov, P. Dudin, L. Baldassarre, A. Perucchi, E. Papalazarou, P. Metcalf, S. Lupi, and M. Marsi. Photoemission microscopy

study of the two metal-insulator transitions in Cr-doped V_2O_3. *Applied Physics Letters*, (**100**):014108, 2012. doi: 10.1063/1.3675445. URL http://link.aip.org/link/?APL/100/014108/1.

[104] A. V. Balatsky, I. Vekhter, and Jian-Xin Zhu. Impurity-induced states in conventional and unconventional superconductors. *Rev. Mod. Phys.*, (**78**): 373–433, 2006. doi: 10.1103/RevModPhys.78.373. URL http://link.aps.org/doi/10.1103/RevModPhys.78.373.

[105] R. Lopez, T. E. Haynes, L. A. Boatner, L. C. Feldman, and R. F. Haglund. Size effects in the structural phase transition of VO_2 nanoparticles. *Phys. Rev. B*, (**65**):224113, 2002. doi: 10.1103/PhysRevB.65.224113. URL http://link.aps.org/doi/10.1103/PhysRevB.65.224113.

[106] L. Baldassarre, A. Perucchi, D. Nicoletti, A. Toschi, G. Sangiovanni, K. Held, M. Capone, M. Ortolani, L. Malavasi, M. Marsi, P. Metcalf, P. Postorino, and S. Lupi. Quasiparticle evolution and pseudogap formation in V_2O_3: An infrared spectroscopy study. *Phys. Rev. B*, (**77**):113107, 2008. doi: 10.1103/PhysRevB.77.113107. URL http://link.aps.org/doi/10.1103/PhysRevB.77.113107.

Entre métal et isolant: dynamique ultra-rapide dans l'isolant topologique Bi_2Te_3 et domaines microscopiques à la transition de Mott dans V_2O_3

Résumé: Cette thèse présente l'étude de la coexistence métal isolant dans deux systèmes très différents pour la communauté scientifique de la matière condensée : l'isolant topologique 3D Bi_2Te_3 et le composé prototype de la transition de Mott V_2O_3. Ces deux systèmes ont été étudiés par des techniques basées sur la spectroscopie de photoélectrons. La première technique utilisée est le TR-ARPES (time and angle resolved photoemission spectroscopy), avec une résolution temporelle de 80 fs, appliquée à l'isolant topologique 3D Bi_2Te_3 pour distinguer la dynamique ultra-rapide des états métalliques de la surface de celle des états isolants du volume. Cette mesure a permet de comprendre les différents mécanismes de diffusion entre la surface et le volume, ainsi que l'amélioration de la relaxation du cône de Dirac par la préexistence à la sous-surface d'une bande de flexion. La seconde technique utilisée dans cette thèse est le SPEM (scanning photoelectron microscopy), avec une résolution spatiale de 150 nm, permettant d'étudier la coexistence des domaines métalliques et isolants à la transition de Mott dans V_2O_3 ; cette coexistence a pour origine le caractère 1^{er} ordre de la transition. La mesure montre une coexistence métal-isolant dans le Cr-dopé : les domaines métalliques sont dus à des centres de nucléations < 150 nm et la forme des domaines est clairement liée à la forme des marches de clivage.

Mots-clefs: matière condensée, métal, isolant, isolant topologique, transition de Mott, spectroscopy de photoémission, dynamique ultra-rapide, spectromicroscopie

---

Between metal and insulator: ultrafast dynamics in the topological insulator Bi_2Te_3 and microscopic domains at the Mott transition in V_2O_3

Abstract: This thesis presents the study of metal-insulator coexistence in two very different systems for the scientific community of condensed matter: the 3D topological insulator Bi_2Te_3 and the prototype compound of the Mott transition V_2O_3. Both systems were studied by techniques based on the photoelectron spectroscopy. The first technique is the TR- ARPES (time and angle resolved photoemission spectroscopy), with a temporal resolution of 80 fs, applied to the 3D topological insulator Bi_2Te_3, to distinguish the ultrafast dynamics of metallic surface states from that of the insulating bulk states. This allows us to understand the different mechanisms of scattering between the surface and the bulk, as well as the amelioration on the Dirac cone relaxation due to the preexistence of subsurface band bending. The second technique used in this thesis is the SPEM (scanning photoelectron microscopy), with a spatial resolution of 150 nm, which was used to study the coexistence of metallic and insulating domains at the Mott

transition on V_2O_3. This coexistence takes its origin from the first order character of the transition. The measurement shows the metal-insulator coexistence on the Cr-doped: metal domains are due to nucleation centers < 150 nm and the shape of the domains is clearly linked to the shape of the cleavage steps.
Keywords: condensed matter, metal, insulator, topological insulator, Mott transition, photoemission spectroscopy, ultrafast dynamics, spectromicroscopy